西南交通大学学报

第 54 卷 第 5 期
2019 年 10 月

JOURNAL OF SOUTHWEST JIAOTONG UNIVERSITY

Vol. 54 No. 5
Oct. 2019

ISSN: 0258-2724

DOI：10.35741/issn.0258-2724.54.5.15

Materials Science

ENHANCEMENT OF THE SURFACE PLASMON POLARITONS EXCITATION EFFICIENCY

增强表面等离子激元激发效率

Riyadh D. Mansoor [1]*, Alistair Duffy [2]

[1] Engineering College, Al-Muthanna University,
Samawa, Iraq, riyadhdmu@mu.edu.iq
[2] School of Engineering and Sustainable Development, De Montfort University,
Leicester, UK, apd@dmu.ac.uk

Abstract

Surface Plasmon Polaritons (SPPs) are propagating excitations that arise from the coupling of light with collective oscillations of electrons on the metal surface. This paper describes a new approach for increasing the SPP excitation efficiency. Using a computational electromagnetics approach, potential techniques for reducing incident power reflectivity were investigated using the Kretschmann configuration. The effects of different parameters such as incident angle, metal thickness, and dielectric permittivity were tested and optimized to improve the efficiency of SPPs by minimizing reflectivity. An 30% increase in efficiency was obtained. In addition, the optical response of a thin metal film on a glass substrate was numerically examined in terms of SPP excitation. The dependency of the response on the incident angle, materials, and dimensions were demonstrated. This paper describes how an improvement in efficiency can improve the effectiveness of bio-sensing applications through the proper choice of layer dimensions and material permittivity of different layers. The relationship between incident angle and reflectivity for different permittivities can be used for bio-sensing applications such as blood glucose biosensors, etc.

Keywords: Biosensors, Kretschmann Configuration, Reflectivity, Plasmon, Surface Plasmon Polaritons.

摘要 表面等离激元极化子（最高人民党）是传播的激发，它是由光与金属表面上电子的集体振荡耦合而产生的。本文介绍了一种提高 SPP 激励效率的新方法。使用计算电磁方法，使用克雷施曼配置研究了降低入射功率反射率的潜在技术。测试并优化了不同参数（例如入射角，金属厚度和介电常数）的影响，以通过最小化反射率来提高 SPP 的效率。效率提高了 30%。另外，根据 SPP 激发，在数值上检查了玻璃基板上的金属薄膜的光学响应。证明了响应对入射角，材料和尺寸的依赖性。本文描述了效率的提高如何通过适当选择层尺寸和不同层的材料介电常数来提高生物传感应用的有效性。不同介电常数的入射角和反射率之间的关系可以用于生物传感应用，例如血糖生物传感器等。

关键词: 生物传感器，克雷施曼配置，反射率，等离激元，表面等离激元极化子。

I. INTRODUCTION

Surface Plasmons (SP) are of topical interest due to the recent advances in the science that allows for characterizing and structuring metals in nanometer scales [1]. Controlling SP properties has enabled scientists and engineers to reveal a new field of applications ranging from solar cells to biological sensors [2]. SPs are electron charge density waves that exist at the interface of a conductor (usually metal) and adielectric. The interaction between these waves and the free electrons of the conductor excites strongly confined propagating modes. There are number of application areas ranging from optical computing to improved biomedical sensors. For example, in the field of optics, SPs provide opportunities for the confinement and guiding of light in sub-wavelength structures [3]. This confinement in sub-wavelength structures has the potential to increase the integration density in photonic circuits using small size optical components. In addition, SP-based sensors are used for investigating bio-molecular interactions by measuring the changes in the refractive index of the environment that the SPPs propagate in, whether that is due to chemical reactions or analyte concentrations [4].

A. Research Background

Surface Plasmon Polaritons (SPPs) are bound electromagnetic excitations existing at the dielectric-metal interface; resonance coupling between SPPs and light results in enhanced near-field waves. The plasmon was first introduced, theoretically, by Pines [5]. He attributed the loss of electron energy travelling in a metal to the collective oscillations of electrons. These oscillations were known as ‘Plasmons'. The coupling of these bound electrons with the light inside a transparent material was studied by Fano [5], where the term ‘Polariton’ was introduced. A study of electron energy loss ata metal interface was performed by Ritchie [6] to describe surface plasmons. He found that the plasmon modes that exist near the surface of the metal are responsible for the unexplained features of optical reflections on a metallic grating observed by Wood [7]. The term “surface plasmon polaritons” was first introduced by Cunningham in 2007 [8]. The interaction between light and surface charges at the metal-dielectric interface leads to an increased mismatch between the SPP momentum and that of light. Bridging this mismatch allows light and SPP wave vectors to coincide and provide a possibility for SPP excitation.

Different coupling configurations have been proposed to excite SPPs, such as grating couplers, waveguide couplers, and prisms [9]. The excitation of SPPs on metal films was first proposed by Otto and Kretschmann [10] by illuminating a metal film using a dielectric prism with an appropriate angle, which gives rise to the light tunneling at the metal surface and allows for good coupling of light to the SPPs.

B. Research Objective

Increasing of light coupling by improving the SPP efficiency is of significant interest in plasmonic waveguides to reduce the dimensions of waveguides and thereby increase the integration density in optical integrated circuits, as well as to allow improvements in the process of biosensing, a key application area for this technology.

In this study, the effect of the incident light angle on the excitation of SPP is examined and simulated using Computer Simulation Technology CST simulation software. The analyte solution flowing in a material, which is in contact with a metal surface, is simulated by changing the permittivity and measuring the change in the SPP excitation efficiency and SPP generation angle. The proposed design resulting from the research presented in this paper provides a good platform for SPP-based life science applications.

II. Excitation of Surface Plasmon Polaritons: A Review

Illuminating the dielectric-metal interface that is shown in Figure 1 with a p-polarized wave at an incident angle of θ_1 results in a partial reflection of light at the interface. The photon momentum of the incident wave is defined by using the equation $m = \mathrm{hk_d}$, where $\mathrm{k_d} = \frac{2\pi \mathrm{n_d}}{\lambda}$, $\mathrm{n_d}$ is the dielectric refractive index, λ is the wavelength, and h is Planck’s constant. The reflected wave will propagate with an angle equal to θ_1 with similar photon momentum. However, the travelling wave in the metal will propagate with an angle θ_2 and different momentum based on the refractive index of metal $(\mathrm{n_m})$.

Based on Snell’s law [11], there is a limiting angle beyond which no wave can propagate in the metal, this angle θ_c, the critical angle, is defined as [11]:

$$\sin\theta_c = \frac{\mathrm{n_1}}{\mathrm{n_2}}$$

where n_1 and n_2 are the refractive indices of the two materials. Generally, n_1 is greater than n_2 for noble metals around visible wavelengths. Therefore, the incident angle is limited and needs to be greater than θ_c. The oscillating electric field associated with the p-polarized incident wave, hitting the interface with an angle beyond θ_c , will excite surface charges with collective oscillations at the metal-dielectric interface. These oscillations are decaying spatially (evanescent modes) away from the interface and are useful for coupling light to SPPs.

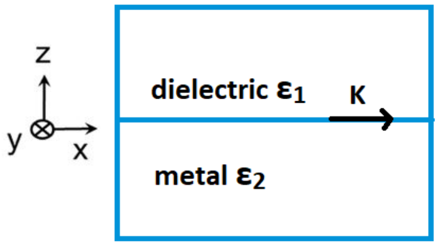

Figure 1. The interface between the dielectric and metal along x-y plane (K is the wavevector).

Applying the boundary conditions for the dielectric/metal interface shown in Figure 1, the normal component of the displacement D (D_z) is continuous. Therefore, the z component of the electric field E_z is discontinuous ($E_{zd} \neq E_{zm}$).

Using Maxwell's equations, equations (1) and (2) are calculated as in [1].

$$E_{zd} = i\frac{k_x}{k_d} E_{xd} \qquad (1)$$

$$E_{zm} = -i\frac{k_x}{k_d} E_{xm} \qquad (2)$$

where k_x is the x-direction component of the wavevectors while k_d is the wavevector at the dielectric material. Applying the curl function for the electric fields' components at z>0 (dielectric medium) yields:

$$-k_{zd} E_{xd} - ik_x E_{zd} = ikH_{yd} \qquad (3)$$

In eq. 3, k is the light wavevector in free space ($k = \omega/c$), and for $z < 0$ (metal) (3) yields:

$$k_{zm} E_{xm} - ik_x E_{zm} = ikH_{ym} \qquad (4)$$

From the equations above, the wave vectors can be expressed as in (5) and (6):

$$k_{zd}{}^2 = k_x{}^2 - \varepsilon_d k^2 \qquad (5)$$

and

$$k_{zm}{}^2 = k_x{}^2 - \varepsilon_m k^2 \qquad (6)$$

In addition, the relationship between normal components of wavevectors and dielectric constants in the metal and dielectric media is given by:

$$\frac{k_{zd}}{k_{zm}} = -\frac{\varepsilon_d}{\varepsilon_m} \qquad (7)$$

From equations 5, 6 and 7, the wavevector k_x can beexpressed as the SPP dispersion relation of k_{spp} [1].

$$k_{spp} = k\sqrt{\frac{\varepsilon_d \varepsilon_m}{\varepsilon_d + \varepsilon_m}} \qquad (8)$$

This nonlinear equation shows a mismatch between SPP momentum (hk_{spp}) and that of light for different frequencies. To overcome this mismatch (excitation of SPP), different techniques have been proposed to have these two dispersion lines intersect at a specific frequency called the SPP frequency, given by [1]:

$$\omega_{spp} = \frac{\omega_p}{\sqrt{1+\varepsilon_d}} \qquad (9)$$

where ω_p is the frequency of the bulk plasmon, given by:

$$\omega_p = \omega\sqrt{1 - \varepsilon_m} \qquad (10)$$

In this paper, the optical response of a thin metal film on a glass substrate is examined numerically in terms of the excitation of SPPs. The dependency of the response on the incident angle, materials, and the dimensions are simulated. The Kretschmann-Raether configuration [12] was simulated and the excitation of the SPPs through the attenuated total reflection was studied. The incident angle of the light relative to the normal of the model is changed to obtain the angle at which the reflection coefficient (S_{11}) reaches its minimum, which means a transmission of power incident on the glass to the metal-air interface due to the excitation of SPP, as will be presented in the next section.

In the Kretschmann modelshown in Figure 2, the photon wavevector in the interface of materials 3and gold $k_{spp\,2}$ (given in equation 8) coincides with the SPP wavevector at the glass(ε_g) and gold (ε_1) interfaces ($k_{spp\,1}$) at a certain angle θ[11].

$$k_{spp\,1} = k\sqrt{\varepsilon_g}\sin\theta$$

At this angle, the incident light is tunneling through the gold and coupled to the surface plasmon [12].

$$k_{spp\,1} = k_{spp\,2}$$
$$\sqrt{\varepsilon_g}\sin\theta = \sqrt{\frac{\varepsilon_1\varepsilon_3}{\varepsilon_1+\varepsilon_3}} \qquad (11)$$

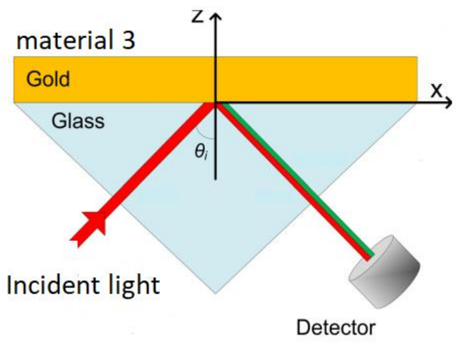

Figure 2. Schematic of the Kretschman coupling configuration.

III. Research Methods: CST Modeling of SPP

A commercial full-wave electromagnetic simulation software package was utilized to perform the numerical simulations of SPP excitation at the interface between Material 3 (the analyte channel) and gold, as shown in Figure 3. The S-parameters were used to calculate power transmission from Port 1 (on the glass plate) to Port 2 (on Material 3). When CST is adopted, S-parameter calculations require that the ports through which the energy enters and leaves the structure be precisely defined. In this work, energy was assumed to enter via Port 1, as light is incident on the glass plate and is reflected at different angles, while Port 2 (Material 3) was used to receive the energy. Moreover, S_{11}, denoting the reflection coefficient, was calculated to estimate the propagation. The study findings indicate that, in the absence of SPP, high S_{11} is obtained for all angles due to the reflection at the interface between metal and dielectric, in line with the fundamental electromagnetic principles. However, at a specific angle, if the SPP exists, a dip in the S_{11} curve emerges, indicating that the power is transformed from Port 1 to Port 2. To elucidate this phenomenon further, in this section, the parameters that affect the angle of SPP generation are examined to emulate the effect of the presence of the analyte in Material 3.

For this experiment, a glass plate of 250 nm thickness and refractive index of 1.62 served as Material 1 to form a metal-dielectric interface with a 50 nm thick gold layer, whereas air (with a refractive index of 1) represented Material 3. The dispersive properties of Material 2 (optical gold) were obtained from the data generated by CST and are presented in Figure 4. For simulations, the background material properties were set to "normal" and the frequency was allowed to take values in the 400−416 THz range. Material 1 *x, y* and *z* dimensions in the initial simulations were set to 100×10×250 nm. Next, a gold layer of 100×10×50 nm dimensions was modeled on top of the glass. The boundary conditions for *x*-direction were set as periodic to simulate continuity, whereas magnetic (Ht = 0) and open boundary conditions were chosen for the *y*- and *z*-direction, respectively. To simulate S-parameters, frequency domain solver was used and waveguide ports were modeled at Material 1 and 3, yielding results shown in Figure 5. S_{11} was measured for different incident angle values. Moreover, parameter sweeping was performed to examine different angles (θ) and permittivity (ε) required to measure the reflection coefficient S_{11}.

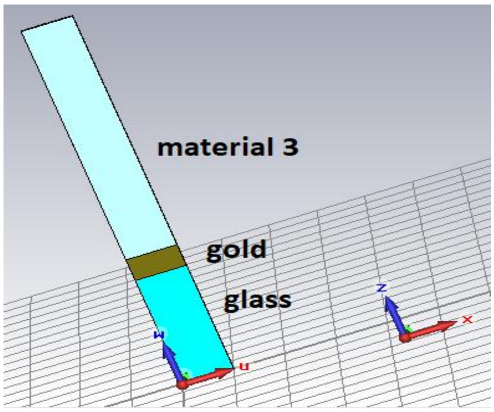

Figure 3. CST model of three materials configuration.

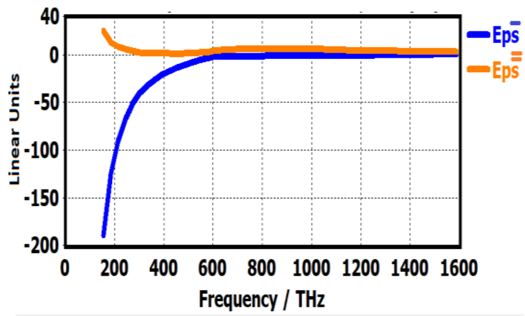

Figure 4. Numerical representation of the real (eps^{-}) and imaginery ($eps^{=}$) parts of the the permittivity of gold.

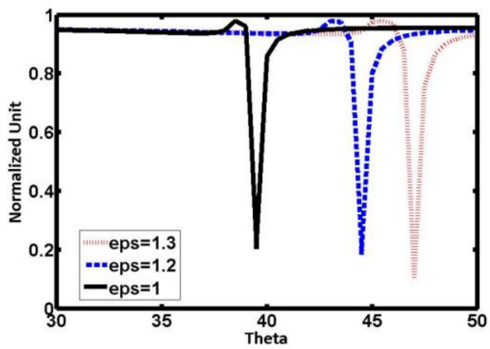

Figure 5. Representation of S11 (reflectivity) for eps3=1, 1.2 and 1.3.

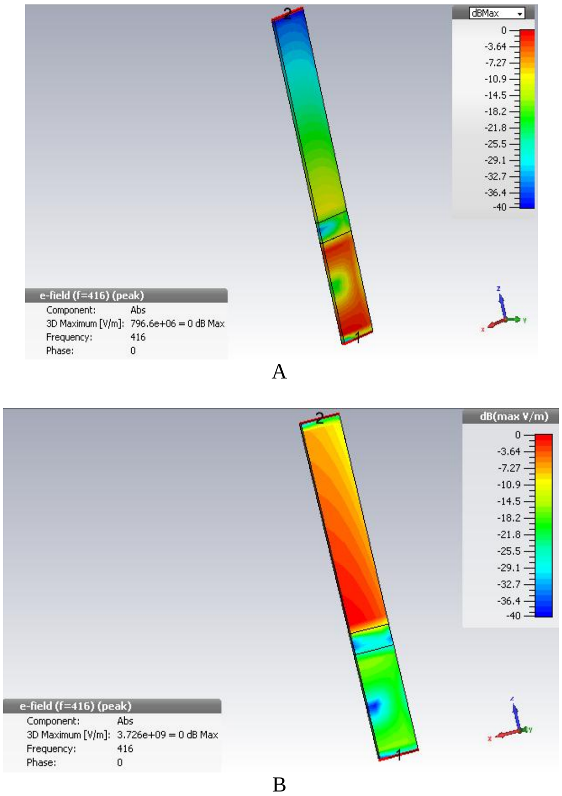

Figure 6. (A) No SPP generation at different angles; (B) Effect of SPP excitation on the energy profile at an angle of 39.5°.

IV. RESULTS AND DISCUSSION

Figure 6 shows the effect of SPP excitation, whereby the field distribution at different ports of the simulated configuration is presented. Specifically, total power reflection is depicted in Figure 6A, while the graph shwon in Figure 6B demonstrates that SPP excitation allows the electric field incident on the glass to be transferred to the other side of the gold material.

Changing the refractive index of the upper cladding was also simulated and tested as a part of the current investigation. For this purpose, two refractive index values (1.2 and 1.3) were simulated without the loss of generality, with the results depicted in Figure 5. In addition to the change in the excitation angle, Figure 5 also reveals a change in the SPP excitation efficiency (equivalent to the minimum value of S_{11}). Specifically, the S_{11} minimum is obtained for ε = 1.3, indicating that minimal power reflection is obtained.

Sweep parameters function in CST was performed for the permittivity of the cladding material (ε) and the incidence angle (θ), revealing that ε varies in the 0.9−1.4 range, whereas θ remains in the 38°–48° range, as shown in Figure 7.

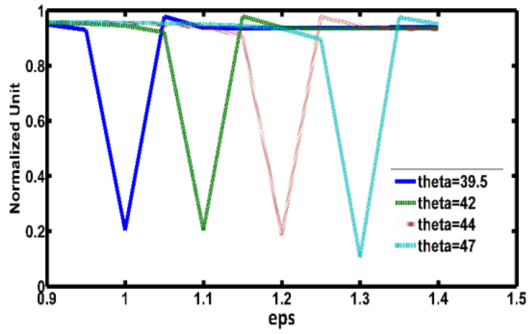

Figure 7. S_{11} for different incident angles (θ) and permittivity (ε) values.

For ε = 1.3, the effect of gold layer thickness (*h*) was also simulated. The findings reported in Figure 8 show that the efficiency of SPP excitation is reduced as the *h* increases due to the increase in tunneling distance [13]. Moreover, *h* = 49 nm corresponds to the maximum SPP excitation efficiency (30% increase compared to that in Figure 7). However, no changes in the SPP efficiency were observed due to changing Material 3 thickness (*h2*) because it is only used for light coupling in this configuration, as shown in Figure 9.

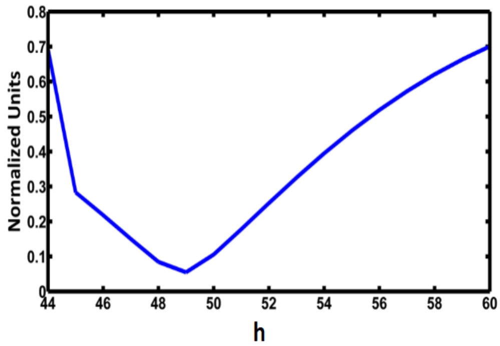

Figure 8. The effect of metal thickness on the SPP excitation efficiency.

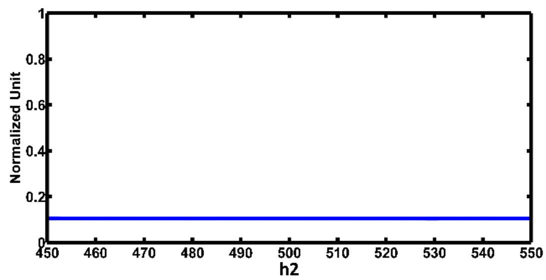

Figure 9. The effect of material 3 thickness (h2) on the SPP excitation efficiency.

A computational electromagnetics approach is clearly beneficial, for developing greater insight into the problem space for SPP excitation. In this work, CST simulation software was used to simulate the excitation of SPP at the interface between metal (gold) and dielectric. The results show how the analyte affects the excitation of SPP at different angles. Optimization of parameters was performed to select the parameters that increase the efficiency of SPP excitation.

V. CONCLUSION

SPP bio sensing is one of the most widely used plasmon based commercial platforms in the life sciences. The analyte solution flows through a channel which is in contact with a (functionalized) gold surface, and this will lead to a change in the reflection angle of the incident light, which in turn provides compact and reliable tools for bio-sensing applications. In this paper, Surface Plasmon Polaritons (SPPs) were simulated in a three-layer structure based on the Kretschmann configuration, in order to study the effect of different parameters on the SPP excitation efficiency. SPP is a charged particle wave that propagates at the metal-dielectric interface. The effect of the incident light is simulated numerically using full-wave simulation software. CST simulation software was used to simulate the excitation of SPP at the interface between metal (gold) and dielectric. Three different values for the permittivity of the dielectric material were used to simulate the effect of the solution analyte. The results show how the analyte affects the excitation of SPP at different angles. Optimization of parameters was performed to select the parameters that increase the efficiency of SPP excitation.

VI. APPLICATION POTENTIAL

This model and analysis can be used for bio-sensing design by changing the permittivity of the material at the top of the gold material to select the optimum design parameters. Grating-enhanced SPP excitation can also be proposed to study the enhancement of the excitation efficiency.

REFERENCES

[1] MANSOOR, R. and AL-KHURSAN, A.H. (2018) Numerical modelling of surface plasmonic polaritons. *Results in Physics*, 9, pp. 1297-1300.

[2] FERRY, V.E., SWEATLOCK, L.A., PACIFICI, D., and ATWATER, H.A. (2008) Plasmonic nanostructure design for efficient light coupling into solar cells. *Nano Letters*, 8(12), pp. 4391-4397.

[3] ZHANG, J., ZHANG, L., and XU, W. (2012) Surface plasmon polaritons: physics and applications. *Journal of Physics D: Applied Physics*, 45(11), 113001.

[4] KUMAR, S., WITTENBERG, N.J., and OH, S.-H. (2012) Nanopore-induced spontaneous concentration for optofluidic sensing and particle assembly. *Analytical Chemistry*, 85(2), pp. 971–977.

[5] BARNES, W.L., DEREUX, A., and EBBESEN, T.W. (2003) Surface plasmon subwavelength optics. *Nature*, 424(6950), pp. 824–830.

[6] RITCHIE, R.H. (1957) Plasma Losses by Fast Electrons in Thin Films. *Physical Review*, 106, pp. 874–881.

[7] WOOD, R.W. (1902) On a Remarkable Case of Uneven Distribution of Light in a Diffraction Spectrum. *Proceedings of the Physical Society of London*, 18(1), pp. 269–275.

[8] LEE, I.-M., JUNG, J., PARK, J., KIM, H., and LEE, B. (2007) Dispersion characteristics of channel plasmon polariton waveguides with step-trench-type grooves. *Optics Express*, 15(25), pp. 16596-16603.

[9] WILLETS, K.A. and VAN DUYNE, R.P. (2007) Localized surface plasmon resonance spectroscopy and sensing. *Annual Review of Physical Chemistry*, 58, pp. 267–297.

[10] ZAYATS, A.V., SMOLYANINOV, I.I., and MARADUDIN, A.A. (2005) Nano-optics of surface plasmon polaritons. *Physics Reports*, 408(3-4), pp. 131-314.

[11] SMITH, D.R., PENDRY, J.B., and WILTSHIRE, M. (2004) Metamaterials and negative refractive index. *Science*, 305(5685), pp. 788-792.

[12] WANG, L., and ZHU, S. (2005) Large negative lateral shifts from the Kretschmann–Raether configuration with left-handed materials. *Applied Physics Letters*, 87(22), 221102.

[13] SIDORENKO, S. and MARTIN, O.J.F. (2007) Resonant tunneling of surface plasmon-polaritons. *Optics Express*, 15(10), pp. 6380-6388.

参考文

[1] MANSOOR，R. 和 AL-KHURSAN，A.H.（2018）表面等离子体激元的数值模拟。物理学报，9，第 1297-1300 页。

[2] 费里（Verry）费里（Ferry），洛杉矶（LA）的SWEATLOCK，华盛顿州帕奇菲奇（PACIFICI）和 宾夕法尼亚州阿特瓦特（ATWATER）（2008）等离子纳米结构设计，可将有效的光耦合到太阳能电池中。纳米字母，8（12），第 4391-4397 页。

[3] ZHANG，J.，ZHANG，L.，和 XU，W.（2012）表面等离激元极化子：物理与应用。物理学杂志D：应用物理学，45（11），113001。

[4] KUMAR，S.，WITTENBERG，N.J。和 OH，S.-H。（2012）纳米孔诱导的自发浓度，用于光流传感和粒子组装。分析化学，85（2），第 971–977 页。

[5] W.L.的BARNES，A。的DEREUX 和 T.W.的EBBESEN。（2003）表面等离子体激元亚波长光学。自然，424（6950），第 824–830 页。

[6] RITCHIE，R.H.（1957）薄膜中快速电子引起的等离子体损失。《身体评论》，106，第 874–881 页。

[7] WOOD，R.W。（1902年）关于衍射光谱中光分布不均匀的显着情况。伦敦物理学会会议论文集，18（1），第 269-275 页。

[8] LEE，I.-M.，JUNG，J.，PARK，J.，KIM，H. 和 LEE，B.（2007）带有阶梯沟槽型沟槽的通道等离子体激元极化子波导的色散特性。光学快递，15（25），第 16596-16603 页。

[9] WILLETS，K.A. 和 VAN DUYNE，R.P.（2007）局部表面等离子体共振光谱和传感。物理化学年度评论，58，第 267-297 页。

[10] ZAYATS，A.V.，SMOLYANINOV，I.I。和 MARADUDIN，A.A。（2005）表面等离振子极化子的纳米光学。物理报告408（3-4），第 131-314 页。

[11] SMITH，D.R.，PENDRY，J.B. 和 WILTSHIRE，M.（2004）超材料和负折射率。科学，305（5685），第 788-792 页。

[12] Wang，L. 和 ZHU，S.（2005）左撇子在克雷茨曼·雷瑟构型中产生较大的负侧移。应用物理学快报，87（22），221102。

[13] S. SIDORENKO 和 O.J.F. MARTIN。（2007）表面等离振子-极化子的共振隧穿。光学快报，15（10），第 6380-6388 页。

Optical Crosstalk Improvement in Ring Resonator Based Add/Drop Multiplexers Using Controllable Reflectivity

Riyadh D. Mansoor [1] and Alistair P. Duffy [2]

[1] Engineering College
Al-Muthanna University, Samawa, Iraq
riyadhdmu@mu.edu.iq

[2] School of Engineering and Sustainable Development
De Montfort University, Leicester, UK
apd@dmu.ac.uk

Abstract **—** In this paper, the topic of optical signal integrity is approached by studying crosstalk suppression in ring resonator based optical Add/Drop Multiplexers (OADM). The resonance splitting induced by surface corrugation is exploited to enhance signal integrity by increasing the crosstalk suppression bandwidth compared to that of a smooth-walled resonator. Sidewall roughness in silicon-on-insulator waveguides is studied using Coupled Mode Theory (time and space domain CMT). An analytical model of a corrugated ring resonator is presented, which is then exploited to estimate the spectral response of the different ports. Verification against results generated from full-wave electromagnetic numerical modeling of a randomized corrugated ring is performed. The analysis then examines the performance of an OADM with controllable reflectivity resulting from a predefined corrugation of sidewall. Gratings have been successfully used in optical filters; this paper proposes the use of a grating in an OADM, giving more controlled roughness. A grating-assisted design of a single ring OADM with 28 GHz crosstalk suppression bandwidth is presented. This bandwidth supports the dropping of 10 Gbps signals with mitigated crosstalk levels and improved signal integrity.

Index Terms **—** Back reflection, crosstalk, grating reflectivity, ring resonators, sidewall roughness.

I. INTRODUCTION

Signal integrity issues in all optical networks are of increasing interest due to the closer proximity of waveguides and optical components as integration density increases. The distinction between RF and optical communications frequencies is diminishing, making true on the claim that Electromagnetic compatibility (EMC) is "a DC to light phenomenon". Silicon-On-Insulator (SOI) is a promising technology to increase the integration density of all optical networks [1], [2]. SOI waveguides provide high confinement of light in devices of small dimensions and allow for large-scale integration in planar light wave circuits [3]. In this technology the propagation loss is relatively low [4]. However, the back-reflection effect due to sidewall roughness is of great importance [5], [6]. In rough-walled ring resonators, back reflection is a well-known cause of resonance splitting due to the interference between forward and counter-directional modes [7]-[9]. This effect has been exploited to increase the extinction ratio by enhancing the depth of the through port response at resonance [7]. In this paper, the resonance splitting resulting from a periodic perturbation of the sidewall roughness is exploited to improve the crosstalk performance of optical add/drop multiplexers OADMs in wavelength division multiplexed (WDM) networks by increasing the crosstalk suppression bandwidth [10].

Back reflection is a frequency dependent phenomenon that manifests as a variation of the response at each resonant frequency. The existence of resonance splitting relies on the relation between coupling coefficients and reflectivity. To extract the coupling and loss coefficients from experimental or numerical results, the back-reflection effect should be considered to produce an accurate analysis of OADMs. A coherent backscattering measuring system [11] and a fully analytical model [4] have been proposed to characterize all parameters of the ring including back reflection.

The sidewall roughness was created using semi-periodic gratings as reported, experimentally, in [12]. A set of ridges having identical length and period was shown to act as a wall corrugation. Therefore, it was studied as a quasi-grating and the reflectivity was measured as a function of frequency. Controlling the backscattering by predefining the dimensions of a quasi-grating during the fabrication introduces a new field of applications using grating-assisted resonators [13], [14]. Using Bragg grating calculations [15], the back-reflection

Submitted On: January 18, 2019
Accepted On: May 6, 2019

effect can be controlled by changing the grating dimensions (number, period and lengths of gratings). The dual-mode filter model has been used recently in photonic integrated platforms [16] in a similar manner to that in microwave circuits. Using a partial reflector inside a single ring resonator will result in a second order response. This effect has been exploited to enhance filter performance [9] and maximize the bandwidth of crosstalk suppression [17].

In this paper, controllable levels of back-reflection induced by a periodic surface corrugation are exploited to improve the crosstalk suppression bandwidth. This bandwidth of crosstalk suppression is defined as the bandwidth over which the suppression of intra-band crosstalk is maintained above 20 dB [18]. To achieve this aim, the research presented in this paper is arranged as follows:

1. Time domain Coupled Mode Theory (CMT) [19], [20] is exploited to propose an analytical model. This model allows a complete characterization of all parameters of the ring including back reflection.

2. An equivalent model of the corrugated ring is presented. The back-reflection can be visualized as resulting from a virtual ring. The space domain calculation is used, where the sidewall roughness is treated as a single scattering point.

3. The validity of the proposed models is tested against an existing experimental result [4]. Time and space domain models allow for accurate characterization of the ring without the need for curve fitting calculations.

4. The spectral response of different ports is simulated numerically using a commercial full wave simulation tool, CST [21], and the controllable reflectivity induced by semi-periodic gratings is modelled and validated using the ASPIC design simulator [22].

This paper presents a general solution for rough-wall ring resonator modelling as well as a particular solution to maximize the crosstalk suppression bandwidth. It concludes with a design that provides a 28 GHz crosstalk bandwidth.

II. COUPLED MODE ANALYSIS

Mutual coupling between the back reflected mode (induced by surface corrugation) and the forward mode is modelled analytically using CMT (coupled mode theory), both in the time and space domains.

A. Time domain analysis

Starting with Fig. 1, $a(t)$ is the forward mode, while $b(t)$ refers to the back-reflection mode, which is related to $a(t)$ through the reflection coefficient *r*. No new channels at the add port were assumed.

Based on the analysis of the time domain CMT [7], [23], the stored energy in the ring (forward mode) behaves as described by eq. (1):

$$\frac{\mathrm{da(t)}}{\mathrm{dt}} = \left(\mathrm{j}\omega_0 - \frac{1}{\tau}\right) \cdot \mathrm{a(t)} - \mathrm{j}k_1 \cdot \mathrm{S_i} - \mathrm{ju} \cdot \mathrm{b(t)}. \tag{1}$$

Where $u = \sqrt{\mathrm{r}} \cdot \frac{\mathrm{V_g}}{\mathrm{l}}$, is the mutual coupling, l is the perimeter of resonator $(2\pi R)$, V_g is the group velocity and $\frac{1}{\tau}$ is the decay rate of energy inside the ring (which depends mainly on the losses and coupling coefficient inside the resonator). S_i and k_1 are the input field and the coupling coefficient, respectively.

Also, the energy of the back-reflection mode changes as in eq. (2):

$$\frac{\mathrm{db(t)}}{\mathrm{dt}} = \left(\mathrm{j}\omega_0 - \frac{1}{\tau}\right) \cdot \mathrm{b(t)} - \mathrm{ju} \cdot \mathrm{a(t)}. \tag{2}$$

Based on (1) and (2), *a(t)* and *b(t)* can be obtained as in (3), (4) and (5):

$$\mathrm{a(t)} = \frac{-\mathrm{j}k_1 \cdot \mathrm{S_i} - \mathrm{ju} \cdot \mathrm{b(t)}}{\mathrm{A}}, \tag{3}$$

$$\mathrm{A} = \mathrm{j}(\omega - \omega_o) + \frac{1}{\tau}, \tag{4}$$

$$\mathrm{b(t)} = \frac{-\mathrm{ju} \cdot \mathrm{a(t)}}{\mathrm{A}}. \tag{5}$$

And from (3) and (5), equation (6) is obtained:

$$\mathrm{a(t)} = \frac{-\mathrm{j} \cdot k_1 \cdot \mathrm{A}}{\mathrm{A}^2 + \mathrm{u}^2} \cdot \mathrm{S_i}. \tag{6}$$

Considering that β is the propagation constant in a waveguide of length *l*; the response of each port is as follows [17]:

i. Through-port spectral response (equations (7) and (8)):

$$\mathrm{S_t} = \mathrm{e}^{\mathrm{j}\beta\mathrm{l}}\left(\mathrm{S_i} - \mathrm{j} \cdot k_1 \cdot \mathrm{a(t)}\right), \tag{7}$$

$$\left|\frac{\mathrm{S_t}}{\mathrm{S_i}}\right|^2 = \left|1 - \frac{{k_1}^2 \cdot \mathrm{A}}{\mathrm{A}^2 + \mathrm{u}^2}\right|^2. \tag{8}$$

ii. Drop-port spectral response (equations (9) and (10)):

$$\mathrm{S_d} = -\mathrm{j} \cdot k_2 \cdot \mathrm{a(t)}, \tag{9}$$

$$\left|\frac{\mathrm{S_d}}{\mathrm{S_i}}\right|^2 = \left|\frac{k_1 k_2 \cdot \mathrm{A}}{\mathrm{A}^2 + \mathrm{u}^2}\right|^2. \tag{10}$$

iii. Add-port response (reflectivity) (equations (11 – (13)):

$$\mathrm{S_a} = -\mathrm{j} \cdot k_2 \cdot \mathrm{b(t)}, \tag{11}$$

$$\mathrm{S_a} = \frac{-k_1 k_2 \cdot \mathrm{u}}{\mathrm{A}} \cdot \mathrm{a(t)}, \tag{12}$$

$$\left|\frac{\mathrm{S_a}}{\mathrm{S_i}}\right|^2 = \left|\frac{k_1 k_2 \cdot \mathrm{u}}{\mathrm{A}^2 + \mathrm{u}^2}\right|^2. \tag{13}$$

The behavior at resonance is given in equations (14), (15) and (16):

$$\left|\frac{S_t}{S_i}\right|^2=\frac{\left[u^2+\frac{1}{\tau^2}-\frac{{k_1}^2}{\tau}\right]^2}{\left[u^2+\frac{1}{\tau^2}\right]^2}, \tag{14}$$

$$\left|\frac{S_d}{S_i}\right|^2=\frac{\frac{{k_1}^2{k_2}^2}{\tau^2}}{\left[u^2+\frac{1}{\tau^2}\right]^2}, \tag{15}$$

and

$$\left|\frac{S_a}{S_i}\right|^2=\frac{{k_1}^2{k_2}^2\cdot u^2}{\left[u^2+\frac{1}{\tau^2}\right]^2}. \tag{16}$$

To obtain the scattering parameters,

$$\mathrm{Th_o}=\left|\frac{S_t}{S_i}\right|^2,\ \mathrm{Dr_o}=\left|\frac{S_d}{S_i}\right|^2,\ \text{and}\ \mathrm{Re_o}=\left|\frac{S_a}{S_i}\right|^2,$$

where, Th_o, Dr_o and Re_o are the through, drop and back reflection values at resonance respectively.

From (15) and (16):

$$\frac{\mathrm{Dr_o}}{\mathrm{Re_o}}=\frac{1}{\tau^2\cdot u^2}. \tag{17}$$

Then,

$$u^2=\frac{1}{\tau^2}\cdot\frac{\mathrm{Re_o}}{\mathrm{Dr_o}}. \tag{18}$$

To obtain τ, the ratio of Eqs. (10) and (13) is taken at f_1 which is the frequency where $\mathrm{Re}=\frac{1}{2}\cdot\mathrm{Re_o}$. With some rearrangements, equation (19) results:

$$\tau=\frac{1}{\Delta\omega}\cdot\sqrt{\frac{2\mathrm{Dr}}{\mathrm{Dro}}-1}\ . \tag{19}$$

Dr is the value of the drop response at f_1 and $\Delta\omega$ is the frequency difference between f_1 and the resonant frequency.

Given the value of τ, the back-reflection coefficient is expressed as in Equ. (20):

$$R=\frac{(\Delta\omega)^2\cdot l^2}{vg^2}\cdot\frac{\mathrm{Dro}\cdot\mathrm{Re_o}}{\sqrt{2\mathrm{Dr}-\mathrm{Dro}}}. \tag{20}$$

Also, the coupling coefficients can be represented as in equations (21) and (22):

$${k_1}^2=\frac{l}{v_g}\cdot\frac{1}{\tau}\cdot\frac{(\mathrm{R_{eo}}+\mathrm{D_{eo}})}{\mathrm{D_{eo}}}\cdot\left[1-\sqrt{\mathrm{Th_o}}\right], \tag{21}$$

$${k_2}^2=\frac{l}{v_g}\cdot\frac{1}{\tau}\cdot\frac{(\mathrm{R_{eo}}+\mathrm{D_{eo}})}{\left[1-\sqrt{\mathrm{Th_o}}\right]}. \tag{22}$$

Finally, the losses can be measured based on [24] as in equation (23):

$${k_p}^2=\left[\frac{2\cdot l}{v_g}\cdot\frac{1}{\tau}\right]-{k_1}^2-{k_2}^2. \tag{23}$$

And the losses coefficient is given in equation (24):

$$\alpha=\frac{1}{l}\cdot\left[-10\cdot\log\left(1-{k_p}^2\right)\right]. \tag{24}$$

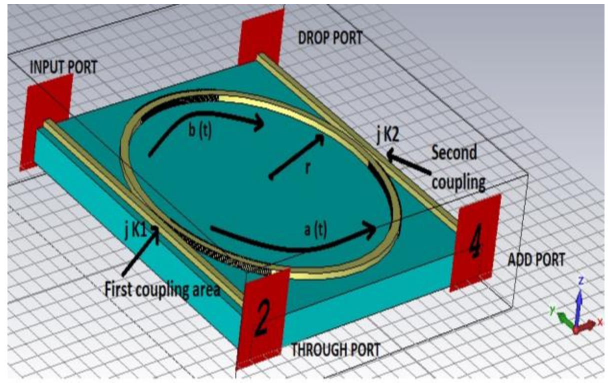

Fig. 1. Forward and back reflected modes in a rough-walled RR add/drop filter.

B. Space domain analysis

Although the scattering is distributed around the ring, it is helpful to think of it as an accumulated single scattering point [6] as shown in Fig. 2 (a). This point of scattering is characterized by $({K_r}^2)$ and $({t_r}^2)$, the back-reflection and transmission coefficient, respectively. The proposed equivalent structure is shown in Fig. 2 (b), where the reflection is assumed to be induced by a virtual ring.

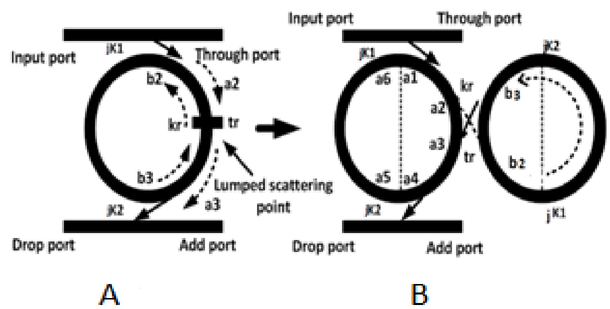

Fig. 2. The corrugated ring resonator (a), and (b) is the proposed virtual model.

The loop equations were written as in [17] to calculate the spectral responses of each port considering the existence of back reflection.

The drop port response is given in equation (25):

$$S_d=\frac{-k_1k_2\cdot\left[t_r-t_1t_2e^{-j\emptyset}\right]\cdot e^{-j\emptyset/2}}{1-2\cdot t_1t_2\cdot t_r\cdot e^{-j\emptyset}+{t_1}^2{t_2}^2\cdot e^{-2j\emptyset}}, \tag{25}$$

where, $\emptyset=\alpha l+j\beta l$, is the propagation loss and phase change. k_1 and k_2 are the bus/ring power coupling coefficients, $t_r=\sqrt{1-{k_r}^2}$ and l is the ring perimeter.

Also, the response of through port is given as in (26):

$$\mathrm{S_t} = \frac{t-(t_1^2-1)t_r t_2 e^{-j\phi} + t_2^2 t_1 e^{-j\phi}}{1-2t_1 t_2 t_r e^{-j\phi} + (t_1 t_2)^4 e^{-2j\phi}}. \quad (26)$$

Finally, the induced back-reflected signal at the add port due to the counter directional propagated mode is as given in equation (27):

$$\mathrm{S_{back}} = \frac{\mathrm{jk_r} \cdot k_1 k_2 \cdot \mathrm{t_1} \cdot \mathrm{e}^{-\mathrm{j}3\emptyset/2}}{1-2\cdot t_1 t_2 \cdot \mathrm{t_r} \cdot \mathrm{e}^{-\mathrm{j}\emptyset} + {t_1}^2 {t_2}^2 \cdot \mathrm{e}^{-2\mathrm{j}\emptyset}}. \quad (27)$$

Equations (25) to (27) represent the frequency response of a corrugated ring OADM. These equations and equations (21)-(23) allow for complete modelling of corrugated ring resonators and provide an alternative solution to reproduce the experimental results without the need for curve fitting.

C. Validation

These models (in both the time and space domains) are examined first against the experimental outcomes published in [4].

1. The analytical model (time domain) represented by equations (20) to (23) is used to extract the coupling coefficients from the experimentally determined response presented in [4], as shown in Fig. 3 (b). The fitted parameters are: ${\mathrm{k_1}}^2 = 4.8\%$, ${\mathrm{k_2}}^2 = 1.76\%$, $\mathrm{t_r} = 0.9991$ and the round-trip loss $\mathrm{e}^{-\alpha l} = 0.9639$.

2. The space domain model was used to plot the spectral response and reproduce the experimental results using coupling coefficients (${\mathrm{K_1}}^2, {\mathrm{K_2}}^2, \mathrm{t_r}$, and loss coefficient) calculated in step 1.

A comparison between Figs. 3 (a) and (b) shows the accuracy of the presented models and allows for the use of these equations for filter performance optimization in terms of crosstalk and signal integrity.

For further validation, a corrugated ring was modeled using CST MWS [21]. Figure 4 shows the CST model of a ring resonator based OADM.

In the electromagnetic model, the following parameters were used:

A substrate was silicon dioxide of 1 μm height with a 1.44 refractive index. Then the silicon waveguides were introduced above the substrate with 0.22 μm heights and 0.5 μm widths for single mode propagation [3]. A refractive index of 3.47 was used for the silicon waveguides [25]. The upper cladding was air. The corrugated ring was first modeled geometrically using Ruby code [26], and then moved into CST as a Wavefront.obj file. The ring radius was 8μm and the distances between the bus waveguides and the ring were 60 nm and 160 nm for the input and output bus waveguides, respectively. These values were taken to ensure the presence of resonance splitting. A hexahedral meshing in the transient CST solver was performed for simulation. The various spectral responses for the ports of a corrugated ring resonator are shown in Fig. 5. $\mathrm{S_{21}}$, $\mathrm{S_{31}}$, and $\mathrm{S_{41}}$ signify the output, drop and back reflection responses, respectively.

Equations (21) to (23) were used to calculate different parameters of the resonator from the simulation results. The modelled corrugated ring parameters (coupling, reflection, and loss coefficients) are calculated as: ${\mathrm{k_1}}^2 = 10.774\%$, ${\mathrm{k_2}}^2 = 1.422\%$, $\mathrm{t_r} = 0.998$ and $\mathrm{e}^{-\alpha l} = 0.986$.

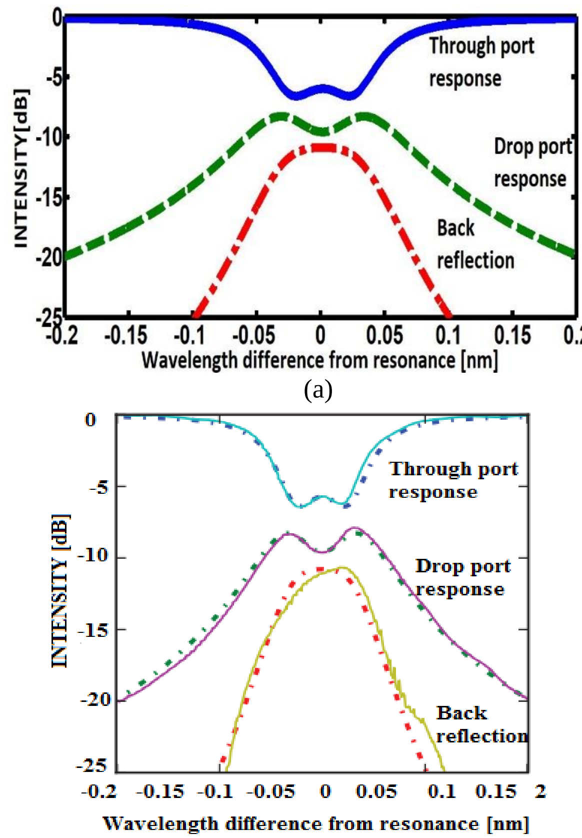

(a)

(b)

Fig. 3. (a) Spectral response of OADM based on time and space domain models. (b) Experimental results presented in [4].

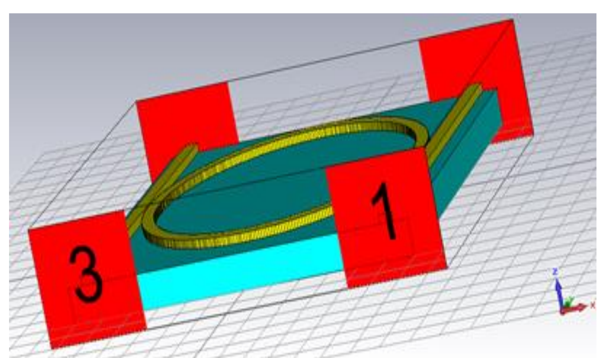

Fig. 4. CST model of a random sidewall roughness in a

corrugated single RR add /drop filter.

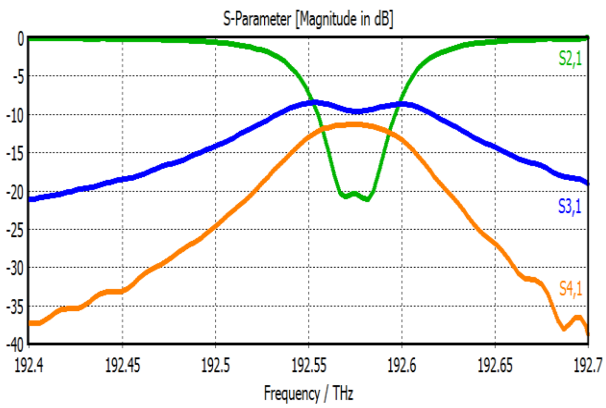

Fig. 5. CST spectral response of a corrugated ring.

These values were introduced into equations (25) - (27) to reproduce the spectral responses of different ports. Figure 6 shows a comparison between the analytically calculated port responses and that fitted using CST simulation. A good agreement between these results is clear. This provides additional validation for the derived equations and enables the application of them to study the effect of back-reflection on the crosstalk suppression bandwidth.

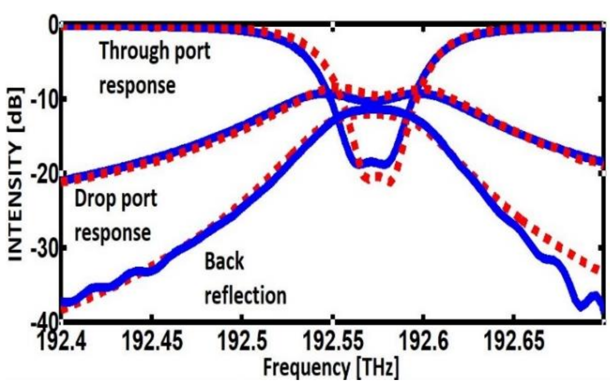

Fig. 6. Numerical (solid) and theoretical (dotted) modelled spectral response for a corrugated ring resonator.

Another advantage of the derived equations is in examining different values of the reflection coefficient (t_r) to show the effect of back-reflection on crosstalk suppression. Increasing the back-reflection coefficient, reducing t_r, leads to strong response splitting due to the mutual coupling between counter directional propagating modes, as shown in Fig. 7. Two minimums and a single maximum would exist in the output port response (S_{21}) of a single ring because of the back-reflection. Similarly, a double maximum and one minimum appears in the drop port response (S_{31}).

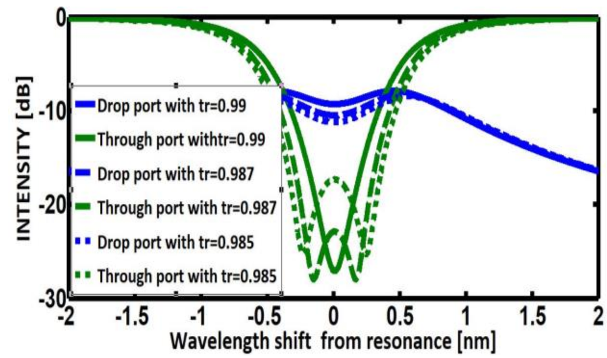

Fig. 7. The effect of reflection coefficient on the output and drop port response.

The difference between S31 (drop port response) and S21 (through port response) at each wavelength, represents the crosstalk suppression. It is required to be higher than |20| dB [27], for as wide a wavelength range as possible to increase the crosstalk suppression bandwidth to ensure high data rate channel dropping with improved signal integrity and mitigated crosstalk. This can be achieved by optimizing the reflectivity of the side-wall within the rough region, as discussed in the following sections.

III. CONTROLLABLE REFLECTIVITY

In this section, total reflectivity resulting from adding a number of reflectors is studied using the Bragg grating reflectivity model [15]. Single and double gratings are shown in Fig. 8.

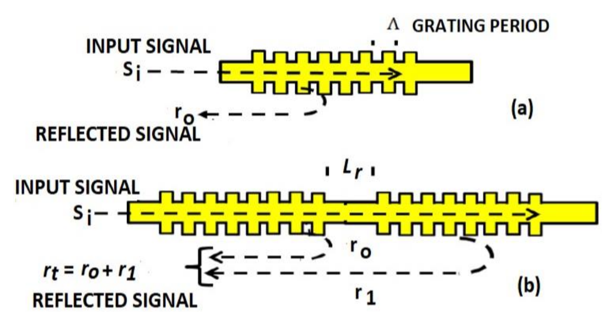

Fig. 8. (a) Single grating and (b) double gratings model.

The power back-reflection coefficient R is modelled as [28] and given in equation (28):

$$R = |r_0|^2 = \frac{k^2 \cdot \sinh^2(S \cdot L)}{\delta^2 \cdot \sinh^2(S \cdot L) + S^2 \cdot \cosh^2(S \cdot L)}, \quad (28)$$

where, r_0 is the reflection coefficient, $k = \frac{\pi \cdot \Delta n_{eff}}{\lambda}$ is the coupler coupling coefficient, and $\delta = \frac{2\pi n_{eff}}{\lambda} - \frac{\pi}{\Lambda}$, is the detuned propagation constant. n_{eff} is the effective refractive index, Λ is the period of the grating, L is the reflector length, and $S = \sqrt{k^2 - \delta^2}$. Equation (28) shows a high dependency of the reflectivity on the change of n_{eff}, and grating parameters (L, and $\wedge$). Increasing the reflectivity by modifying various parameters is the main aim of this section. The refractive indices were 3.47 for Si and 1.44 for SiO_2 at the wavelengths around 1550 nm [3]. $\mathrm{n_{eff}}$ was 2.55, with a constant change over the grating as $\Delta\mathrm{n_{eff}} = 0.5$. The effects of different parameters are examined as follows:

1. Reflector length (L): A 100 nm grating period and 50% duty cycle are considered first; these values were chosen to ensure high reflectivity around 1550 nm. Figure 9 shows that increasing L only influences a change of the reflectivity over the range of wavelengths around 1550 nm. Here, the range of wavelengths obtained was 1540-1560 nm and the best reflector length was 6500 nm (relatively high reflectivity) as shown in Fig. 9.

2. Grating period ($\wedge$): For $L = 6500$ nm and 50% duty cycle. Figure 10 shows an increase in the reflectivity with increasing grating period. Depending on the diffraction theory [12], the Bragg wavelength is ($\lambda_{Bragg} = 2 \cdot n \cdot \wedge$). Therefore, increasing $\wedge$ will increase the Bragg wavelength and shift it nearer to the required range.

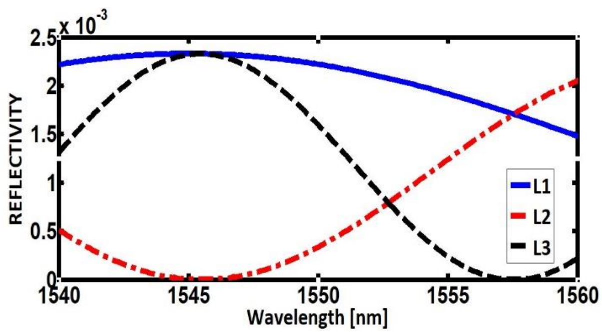

Fig. 9. The effect of $\boldsymbol{L}$. $\boldsymbol{L1}$=6500 nm, $\boldsymbol{L}_2$=13000 nm and $\boldsymbol{L}_3$=19500 nm.

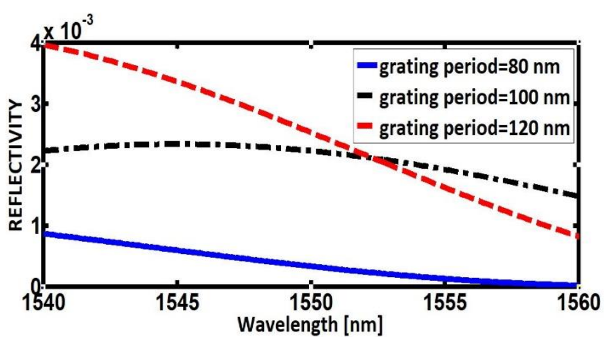

Fig. 10. The effect grating period.

3. Number of reflectors: Fig. 8 (b) shows the case of two groups of gratings, the total reflectivity of this model results from the contribution of each reflector. However, when adding $\mathrm{r_0}$ and $\mathrm{r_1}$, a locked loop needs to be considered between the reflectors. Based on Mason's rule [29], the total reflectivity of two reflectors is as given in equation (29):

$$\mathrm{r_0 + r_1 = \frac{r_0 + r_1 \cdot e^{-j2\beta L_r}}{1 + r_0 r_1 e^{-j\beta L_r}}}. \tag{29}$$

For three groups of gratings, the total reflectivity will be greater due to the number of reflectors. The total reflectivity can be calculated as in equation (30):

$$\mathrm{r_0 + r_1 + r_2 =}$$
$$\mathrm{\frac{r_0 + r_1 e^{-j2\beta L_{r1}} + r_2 e^{-l2\beta(L_{r1}+L_{r2})} + r_0 r_1 r_2 e^{-j2\beta L_{r2}}}{1 + r_0 r_1 e^{-j2\beta L_{r1}} + r_1 r_2 e^{-j2\beta L_{r2}} + r_0 r_2 e^{-l2\beta(L_{r1}+L_{r2})}}}, \tag{30}$$

where L_{r1} and L_{r2} are the separations between gratings. The reflectivity of one, two and three gratings is shown in Fig. 11.

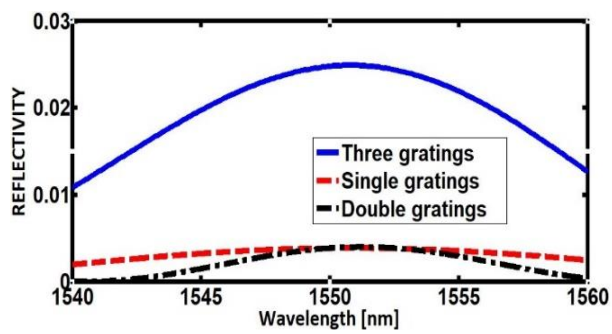

Fig. 11. Number of reflectors effect.

ASPIC design software [22] was used to validate equations (29) and (30), as shown in Fig. 12. ASPIC is a model-based simulation software and approaches simulation differently to the physically based CST MWS simulation software. The effect of using single, double and three gratings is simulated first. It is shown in Fig. 12 (b) that, increasing the number of gratings will result in an increase of back reflection as in [12]. Differences between analytical and ASPIC simulator results may be attributed to the change of the effective index with wavelength (material dispersion) [30].

4. Effect of $\boldsymbol{Lr}$: to obtain high reflectivity, the distance between reflectors should ensure a π radian phase shift. The overall reflectivity is strongly affected by Lr as shown in Fig. 13. Therefore, the perimeter of the grating assisted ring needs to be optimized to maximize the reflection by ensuring a proper Lr.

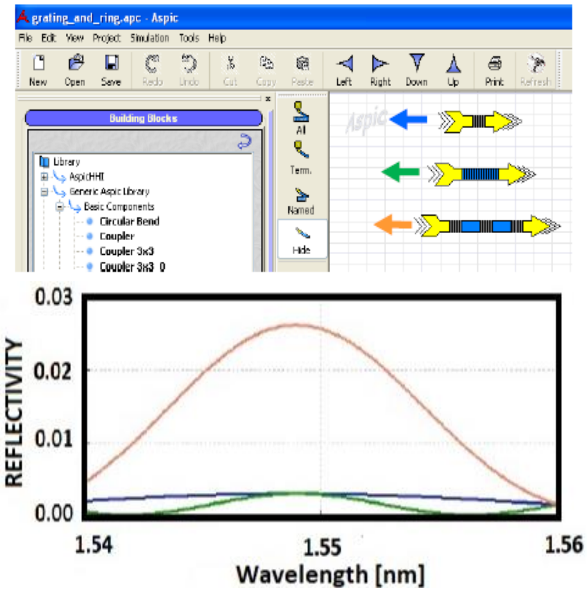

Fig. 12. Aspic model for three gratings (upper), and the reflectivity as a function of wavelength (lower) for single grating (blue), double grating (green) and three gratings (red).

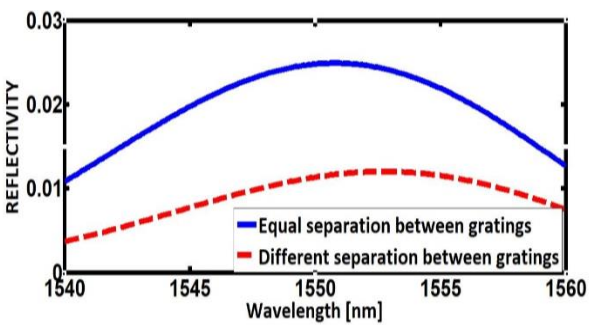

Fig. 13. The separation effect between three reflectors.

IV. GRATING ASSISTED SINGLE RING

This section aims to build on the above calculations to suggest a novel design of OADM that provides high crosstalk mitigation and ensure high integration density. The design steps are listed below:

Step 1: The goal-maximization algorithm is exploited to optimize the coupling and reflection coefficients that maximize the bandwidth of crosstalk suppression. Different parameters of an OADM with a corrugated ring are optimized based on Equations (25) and (26) to maximize the bandwidth of crosstalk suppression. Each time, a set of coupling coefficients (k_1, k_2 and tr) is used to calculate S_{31}-S_{21} and compare it with a |20| dB suppression threshold over the range of frequencies around one resonance.

Step 2: Not only k_1, k_2 and t_r need to be optimized, the ring radius needs to be chosen to match the resonance wavelength with the calculated value of tr.

Step 3: Three reflectors were used to ensure high reflectivity. The distance between the three reflectors was calculated as $(L_r = ((l - 3 \times L))/3)$, where l is the mean length of the ring. To maximize the reflectivity, the distance between reflectors was to be optimized.

Step 4: A model that combined all the parameters (coupling coefficients, ring radius, number of gratings, grating length, and grating period) was used. The optimization approach was performed for 100 and 120 mm grating period since these values provided increased reflectivity, as depicted in Fig. 10.

The optimized ring parameters for maximum crosstalk bandwidth in an asymmetric ring resonator were as follows: The power coupling coefficients $K_1{}^2 = 0.2258$, $K_2{}^2 = 0.0329$, and the back-reflection coefficient $t_r = 0.99$. The optimized value of back-reflection coefficient was used in equation (28) to calculate the length of reflectors inside the ring. A ring of $9.64\ \mu m$ radius loaded with three reflectors each of $6.5\mu m$ length, separated by $13.7\ \mu m$ is proposed. The period of ridges in each reflector is $0.1\mu m$. A 28 GHz crosstalk suppression BW was obtained using these optimized parameters, as shown in Fig. 14. By comparison, an OADM made of a smooth surface ring with high coupling coefficient > 0.65 [18] is needed to obtain a similar crosstalk BW. Such a high coupling coefficient would affect the selectivity of the multiplexer (Q-factor) and allow for the adjacent channels to increase the inter-band crosstalk. Also, a double ring resonator can have a similar BW [18]. However, the integration density will be reduced due to the increased filter size.

To this extent it is shown analytically that a single ring with three reflectors provides high data-rate channel dropping compared to the smooth surface ring OADMs. To ensure the accuracy of the results, a numerical validation using ASPIC simulator for the proposed model was performed.

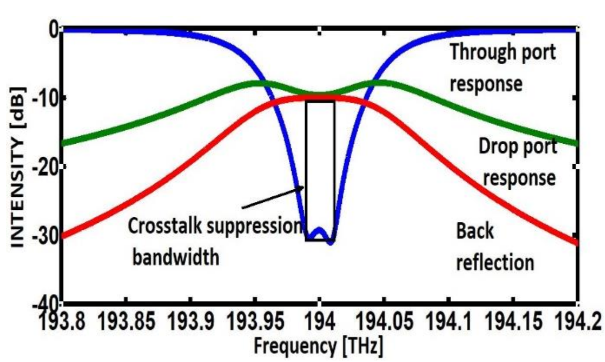

(a)

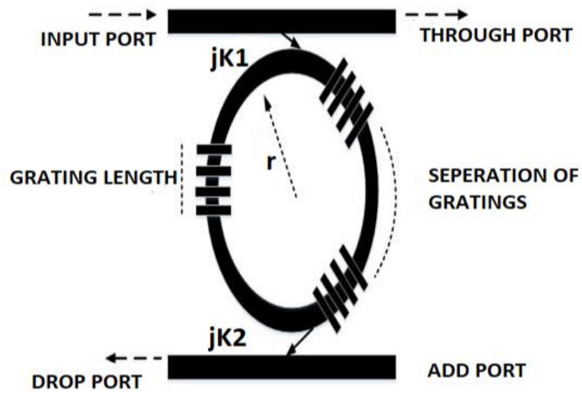

(b)

Fig. 14. (a) The single ring resonator spectral response, and (b) schematic of a grating-assisted OADM.

The ASPIC simulator results for a single ring resonator with three reflectors are shown in Fig. 15, which shows a good agreement with that of [17] (ASPIC simulation was performed for a 5 µm ring resonator model) where the resonance splitting is clear and |20| dB crosstalk suppression is maintained for a wide crosstalk suppression bandwidth.

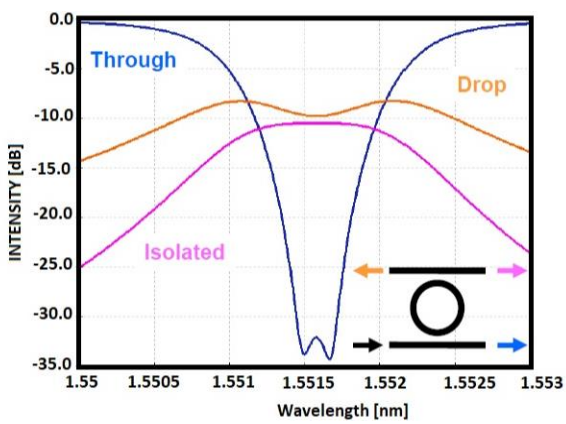

Fig. 15. The three-port response for a grating assisted ring resonator (Aspic simulated results).

V. CONCLUSION

Mitigating crosstalk effects and enhancing signal integrity in a small size ring resonator based OADM, by increasing the crosstalk suppression bandwidth, was the main aim of this paper. The objective of this work is to exploit the resonance splitting induced by silicon waveguide surface corrugation. To do that, a simple and direct approach to estimate all port responses without the need for curve fitting was presented. An equivalent model for the corrugated ring was proposed and examined against experimental published results. 3D simulation software was used for further validation. Analytical and numerical calculations were performed to ensure the accuracy of the proposed model. Finally, this model was used to obtain the optimized parameters of a ring resonator that maximize crosstalk suppression BW. A novel design, with more controllability during manufacture compared to a purely randomized corrugation, was proposed, and a 28 GHz crosstalk suppression BW was achieved. This bandwidth supports the dropping of 10 Gbps signals with mitigated crosstalk level and improved signal integrity.

REFERENCES

[1] A. Bianco, et al., "Crosstalk minimization in microring-based wavelength routing matrices," in *Global Telecommunications Conference (GLOBECOM), IEEE*, pp. 1-5, 2011.

[2] S. Koziel and S. Ogurtsov, "Simulation-driven optimization approach for fast design of integrated photonic components," in *30th Annual Review of Progress in Applied Computational Electro-magnetic*, Jacksonville, FL, pp. 679-684, 2014.

[3] W. Bogaerts, et al., "Silicon microring resonators," *Laser & Photonics Reviews*, vol. 6, no. 1, pp. 47-73, 2012.

[4] G. Ballesteros, et al., "Characterizing and modeling backscattering in silicon microring resonators," *Optics Express*, vol. 19, no. 25, pp. 24980-24985, 2011.

[5] C. Sui, et al., "Analysis of microdisk/microring's surface roughness effect by orthogonal decom-position," *Optics and Photonics Journal*, vol. 3, pp. 288, 2013.

[6] B. E. Little, J. Laine, and S. T. Chu, "Surface-roughness-induced contradirectional coupling in ring and disk resonators," *Opt. Lett.*, vol. 22, no. 1, pp. 4-6, 1997.

[7] Z. Zhang, et al., "Resonance-splitting and enhanced notch depth in SOI ring resonators with mutual mode coupling," *Optics Express*, vol. 16, no. 7, pp. 4621-4630, 2008.

[8] G. T. Paloczi, J. Scheuer, and A. Yariv, "Compact microring-based wavelength-selective inline optical reflector," *IEEE Photonics Technology Letters*, vol. 17, no. 2, pp. 390-392, 2005.

[9] C. Alonso-Ramos, et al., "Dual-mode coupled-resonator integrated optical filters," *IEEE Photonics Technology Letters*, vol. 26, pp. 929-932, 2014.

[10] R. D. Mansoor, et al., "Estimation of the bandwidth of acceptable crosstalk of parallel coupled ring resonator add/drop filters," *IEEE Trans. Electro-magn. Compat.*, vol. 57, no. 5, pp. 1005-1012, 2015.

[11] F. Morichetti, A. Canciamilla, and A. Melloni, "Statistics of backscattering in optical waveguides," *Opt. Lett.*, vol. 35, no. 11, pp. 1777-1779, 2010.

[12] T. Wang, et al., "Modeling of quasi-grating sidewall corrugation in SOI microring add-drop

filters," *Opt. Commun*., vol. 282, no. 17, pp. 3464-3467, 2009.
[13] Y. M. Kang, A. Arbabi, and L. L. Goddard, "Engineering the spectral reflectance of microring resonators with integrated reflective elements," *Optics Express*, vol. 18, no. 16, pp. 16813-16825, 2010.
[14] W. Shi, et al., "Grating-coupled silicon microring resonators," *Appl. Phys. Lett*., vol. 100, no. 12, pp. 121118-121118-4, 2012.
[15] K. O. Hill and G. Meltz, "Fiber Bragg grating technology fundamentals and overview," *J. Lightwave Technol*., vol. 15, no. 8, pp. 1263-1276, 1997.
[16] A. E. Atia and A. E. Williams, "Narrow-bandpass waveguide filters," *Microwave Theory and Techniques, IEEE Transactions On*, vol. 20, no. 4, pp. 258-265, 1972.
[17] R. Mansoor, et al., "Crosstalk bandwidth of grating-assisted ring resonator add/drop filter," *Opt. Quant. Electron*., vol. 47, pp. 1127-1137, 2015.
[18] R. D. Mansoor, et al., "Over coupled ring resonator based add/drop filters," *Quantum Electronics, IEEE Journal of*, vol. 50, no. 8, pp. 598-604, 2014.
[19] A. Yariv, "Coupled-mode theory for guided-wave optics," *Quantum Electronics, IEEE Journal of*, vol. 9, no. 9, pp. 919-933, 1973.
[20] O. Schwelb, "Microring resonator based photonic circuits: Analysis and design," in *Telecommunications in Modern Satellite, Cable and Broadcasting Services*, pp. 187-194, 2007.
[21] 3D Electromagnetic Simulation software, 2013. Available: www.cst.com.
[22] ASPIC design software, 2014. Available: www.aspicdesign.com.
[23] C. Manolatou, et al., "Coupling of modes analysis of resonant channel add-drop filters," *Quantum Electronics, IEEE Journal of*, vol. 35, no. 9, pp. 1322-1331, 1999.
[24] S. Xiao, et al., "Modeling and measurement of losses in silicon-on-insulator resonators and bends," *Optics Express*, vol. 15, no. 17, pp. 10553-10561, 2007.
[25] O. Schwelb, "Transmission, group delay, and dispersion in single-ring optical resonators and add/drop filters-a tutorial overview," *Lightwave Technology, Journal of*, vol. 22, no. 5, pp. 1380-1394, 2004.
[26] Ruby programming language. 2014. Available: https//:www.ruby-lang.org
[27] O. Schwelb, "Crosstalk and bandwidth of lossy microring add/drop multiplexers," *Opt. Commun*., vol. 265, no. 1, pp. 175-179, 2006.
[28] S. P. Ugale and V. Mishra, "Modeling and characterization of fiber Bragg grating for maximum reflectivity," *Optik-International Journal for Light and Electron Optics*, vol. 122, no. 22, pp. 1990-1993, 2011.
[29] S. J. Mason, *Feedback Theory: Further Properties of Signal Flow Graphs*. Research Laboratory of Electronics, Massachusetts Institute of Technology, 1956.
[30] H. Li, "Refractive index of silicon and germanium and its wavelength and temperature derivatives," *Journal of Physical and Chemical Reference Data*, vol. 9, no. 3, pp. 561-658, 1980.

Riyadh D. Mansoor received the B.Sc degree in Electrical and Electronic Engineering and the Master degree from the University of Basra, Iraq, in 1996 and 1998 respectively. He finished his Ph.D. in Optical Communication at De Montfort University, Leicester, UK, in 2015. He is currently working as a Senior Lecturer with the faculty of Engineering, Al-Muthanna University, Samawa, Iraq. His research interests include photonic circuits, optical communications, and Electromagnetic compatibility.

Alistair P. Duffy received the B.Eng. (Hons.) degree in Electrical and Electronic Engineering and the M.Eng. degree from University College, Cardiff, U.K., in 1988 and 1989, respectively. He received his Ph.D. degree from Nottingham University, Nottingham, U.K., in 1993 for his work on experimental validation of numerical modeling.

He is currently Professor of Electromagnetics and Director of the Institute of Engineering Sciences at De Montfort University, Leicester, U.K. He is also a Guest Professor at Harbin Institute of Technology, Harbin, China. He is the author of approximately 300 articles published in journals and presented at international symposia. His research interests include CEM validation, communications cabling, and technology management.

Duffy is a Fellow of the IEEE, the Institution of Engineering and Technology (IET) and the Royal Society for the Encouragement of Arts, Manufactures and Commerce (RSA). He is currently President Elect for the IEEE EMC Society. He is also Chair of the IEEE EMC Society Standards Development and Education Committee, along with a number of Standards working group officer roles. He is an Associate Editor of the IEEE Transactions on EMC Technology management.

Dispersion Characteristics of Asymmetric Multistep Titanium Nitride Channel Plasmon Waveguide

Riyadh Mansoor
College of Engineering
Al-Muthanna University
Al-Muthana, Iraq
r.m.2015@ieee.org

Firas Faeq K. Hussain
Department of physics
College of science
Al-Muthana University
Al-Muthana, Iraq
firas@mu.edu.iq;

Rasha Ali
College of Engineering
Al-Muthanna University
Al-Muthana, Iraq
rasha.laseren@mu.edu.iq

ABSTRACT

Plasmonic waveguides is a hot topic in the field of photonic devices due to the ability to provide signal propagation in nanoscales beyond the diffraction limit. Reducing the dimensions of optical components allows for increasing of integration density and reduce the cost of fabrication. In this paper, the dispersion characteristics of the Channel Plasmon Polaritons CPPs waveguide based on Titanium Nitride TiN material are presented. The proposed design is simulated numerically to obtain the optimum dimensions that provide longer propagation length with low loss. The asymmetric trench waveguide design shows superior performance compared to the symmetric waveguide due to the increase in the mode confinement through the groove. A 100 μm propagation length is achieved at $\lambda = 1.6\,\mu m$ by increasing the asymmetry of the trenches. TiN based waveguide provides a good alternative to the already existing CPPs waveguide designed based on gold and silver materials in terms of cost and the chemical stability. A low cost (compared to gold) and non-oxidize (compared to silver) CPPs waveguide model is proposed and simulated.

KEYWORDS

Plasmonic waveguides, Titanium Nitride TiN material.

1. INTRODUCTION

The increased bandwidth requirements of data communication have motivated the telecommunication companies to increasingly focusing on the integration solutions, allowing architectures to become more integrated [1]. However, miniaturization of optical waveguides, to meet the requirements of highly integrated optical circuits, is subjected to many factors such as the diffraction limit, and signal integrity [2]. Plasmon technology is existed to enable the high confinement of light in nanoscale dimensions allowing for light transmission and coupling in a highly integrated optical components compared to the silicon on insulator technology [3]. Plasmons are collective resonances of free bond electrons of Nobel metals [4] .

The resonance coupling between Surface Plasmons Polaritons SPPs and light results in enhanced near-field waves and leads to propagated excitations. SPs provide a very attractive aspect for researchers, which is the confinement and guiding of light in subwavelength structures [5].

Channel Plasmon Polaritons CPPs exploit the plasmon propagation to provide a waveguide-like behaviour to confine and propagate light in grooves[6]. The length of propagation obtained with this special waveguide exceeds the limitations of other waveguides. Basically, SPPs decays with distance, therefore, the propagation length is defined as the length at which the intensity of the SPPs decayed to (1/e). Hussain et. al [7] have proposed and examined the dispersion characteristics of both gold and silver based asymmetric CPP. It was shown in [7] that silver-based asymmetric CPPs provides a longer propagation length compared to the gold-based for the 200-550 THz frequency range. However, silver cannot be considered as an ideal choice for plasmonic devices due to the change of metal properties when it exposes to air (oxidization).

In this paper, the dispersion characteristics of asymmetric multistep channel plasmonic waveguide made of TiN is studied and presented. The propagation length (L_{prop}), real part of the effective index (n_{eff}), lateral mode radius and figure of merit (FOM) all are simulated and calculated numerically using the Full-Vectorial Finite Difference Frequency Domain (FV-FDFD method in Matlab[8]. The aim of this study is to suggest a new model of asymmetric multistep TiN CPPs waveguide which is sustainable in terms of the cost (compared to the gold CPPs) and of the chemical stability (compared the silver CPPs). TiN is a promising material for application in high integrated photonic devices[9].

2. WAVEGUIDE MODELLING

The cross section of the proposed waveguide is shown in **Figure 1**. In this figure, a TiN based waveguide with multiple trenches of different dimensions in an air cladding is presented. The

ICICT '19, April 15–16, 2019, baghdad, Iraq

ACM ISBN 978-1-4503-6643-4/19/04…$15.00
https://doi.org/10.1145/3321289.3321566

dimensions of trenches are notated as follows: W_1 and d_1 are the width and depth of the wide trench, respectively. While, W_2 and d_2 are the width and depth of the second trench and finally, the notations for the narrow trench, i.e. the width and depth are W3 and d3, respectively. For the special case when $d_3 = d_1$, the cross section turned to a symmetric two trenches waveguide where $d_2=d_1-d_3=0$. The total depth of the groove was fixed as (d= 1.2 µm) [10].

For calculations, values of W_1, d_1, W_2, and W_3 are considered constants as in [9] and listed in Table 1. While, d_2 was changed with a step of $0.1\mu m$ to simulate the asymmetry in the narrow trench. All the results were compared with the symmetrical cross section case, where $d_2=0$ ($d_3=d_1$ and $W_2=W_3$), to emphasize the improvement in the dispersion characteristics of the asymmetrical model over the symmetrical multistep waveguide. During the simulations, the extended-Drude model [11] was used to calculate the permittivity of the TiN material.

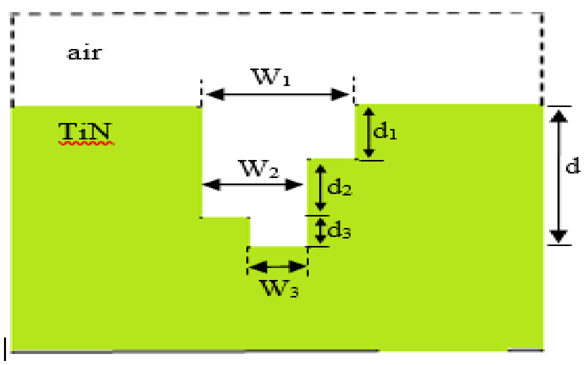

Figure 1. Asymmetric channel plasmon with multistep trench waveguide.

Table 1 design parameters for the CPP waveguide.

parameter	W_1	W_2	W_3	d_1
Dimension [µm]	0.523	0.32	0.12	0.6

The dispersion characteristics of the TiN based CPPs waveguide are calculated as below:

2.1. The Effective Index (n_{eff})

The simulation is started first by calculating the variation of the effective index of the proposed structure with the wavelength. The propagation constant of the SPP is defined as in equation below:

$$\beta = \frac{2\pi n_{eff}}{\lambda} \qquad 1$$

Therefore, it is important to find the effect of changing the dimensions of the waveguide cross section on the effective index.

Figure 2 shows the change of the real part of n_{eff} with the wavelength for different values of d_2. In this figure, the real part of the effective index decreases to a value comparable to the clad effective index as the wavelength getting longer (frequency decrease to 200 THz). By reducing d_2 from 0.4 to 0, the structure becomes symmetrical design. Therefore, the real part of the effective index is highly dependent on the dimension d_2 and decrease by increasing d_2. **Figure 2** also shows that by increasing d_2, the effective index of the quasi-TE mode will decrease, this is due to the change in dimension of the narrow trench W_3 which turned to become shallow, therefor, the field moves to the wider trench.

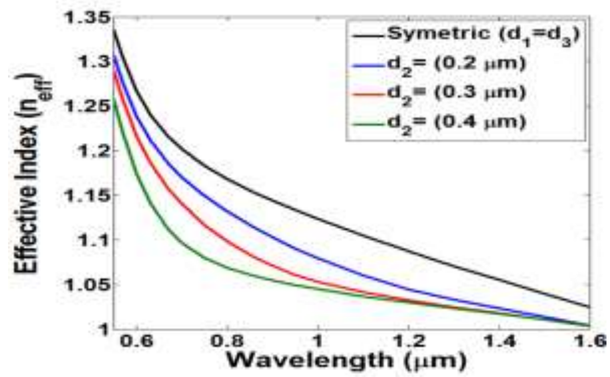

Figure 2. Real part of effective index (neff) variation with the wavelength for conventional symmetric and asymmetric CPP waveguide at d1 = 0.6 µm and different values of d2.

2.2. The propagation length (Lprop)

From equ. 1, the propagation length, which is defined as the length at which the intensity of the SPPs drops to 0.3678 of its original value, can be calculated by [7] :

$$L_{prop} = \frac{1}{Imag(\beta)} \qquad 2$$

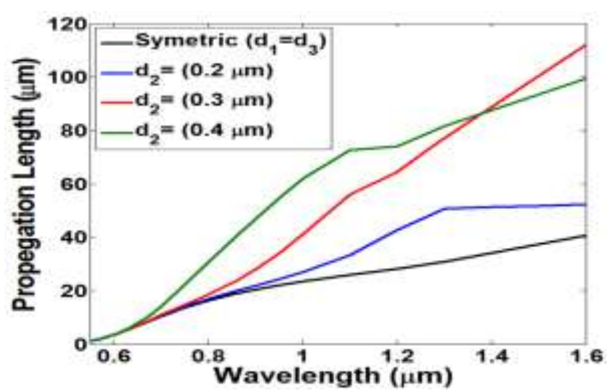

Figure 3. Variation of propagation length with the wavelength for symmetric and asymmetric CPP waveguides at d1 = 0.6 µm and different d2 values.

A comparison between the propagation length for symmetric and asymmetric designs is shown in **Figure 3**. Also, the effect of increasing the asymmetry in the cross section is examined by increasing d_2. In **Figure 3**, from the first glance, it can be seen that by increasing d_2, the propagation length will increase which proves that the asymmetric design provides superior performance over the symmetrical one. For example, in the range of wavelength from 0.6 to 1.4 μm the propagation length is increased to about 90 μm compared to 30 μm for the symmetrical design at the same wavelength (1.4 μm). However, there is a little change in the results for d_2=0.3 as the frequency decrease to 200 THz where the propagation length exceeds that of d_2=0.4 for the range (1.4 to 1.6 μm).

2.3. Lateral mode radius (r_{3dB})

The propagation of the SPPs mode inside the groove is prone to losses. Therefore, it is important to study the relation between the propagation loss and mode confinement to estimate the optimum design. To do so, the lateral mode radius (r_{3dB}) [10] along the width of the waveguide, is introduced and calculated. Practically, to ensure high confinement of the field (of a specific wavelength) in a particular trench of width W, the r_{3dB} need to be larger than W/2 at that wavelength. Thus, a good indication of the optical energy confinement can be achieved by calculating r_{3dB}. **Figure 4** presents the variation of the lateral mode radius over the wavelength range of interest. In this figure, a comparison between the symmetric and asymmetric designs in terms of r_{3dB} is shown. For symmetrical and semi-symmetrical design (d_2=0.2), almost a constant value for r_{3dB} over the whole wavelength range is observed. However, by increasing the asymmetry (d_2=0.3 and 0.4), a sharp change in the r_{3dB} curve is obtained. This is because of the movement of the optical energy towards the upper trench and increased losses in the narrow trench.

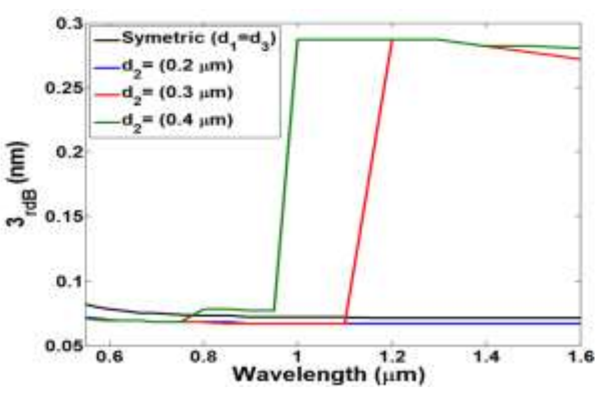

Figure 4. Variation of lateral mode radius r3dB with wavelength for symmetric and asymmetric CPP waveguide at d1 = 0.6 μm and different d2 values.

2.4. The Figure of Merit (FOM)

Finally, the important parameter, needed for completing the design, is the Figure of Merit (FOM). FOM is defined as the trade-off between mode confinement and losses. It is expressed mathematically as [10]:

$$FOM = \frac{L_{prop}}{r_{3dB}} \quad 3$$

This equation implies that, in order to obtain a good design, high FOM should be achieved, which means long propagation length with low propagation loss. **Figure 5** shows the variations of FOM with wavelength for the symmetrical and asymmetrical designs. For the symmetrical design, the highest value of FOM was achieved at low frequency (λ=1.6 μm). However, by slightly altering the symmetry (d_2=0.2), almost a linear increase of FOM with the reduction of frequency is noticed around (0.6-1.3 μm). From this figure, the effect of changing d_2 is clearly affecting FOM, therefore, the optimum dimension for d_2 can be selected from **Figure 5** based on the required wavelength. For example, for 1.3 μm wavelength, the optimum dimension (d_2) should be chosen as d_2=0.3. While for λ=0.8 μm, d_2 need to be 0.4 μm. The sudden changes in the FOM curves for d_2= 0.3 and 0.4 are attributed to the change in r_{3dB} at the same wavelengths as shown in **Figure 4**. A comparison of the obtained FOM for TiN material with that of gold and silver material in [7] (1200 for gold and 1500 for silver) shows a reduction in FOM for the proposed material (≈ 800). However, the propagation length ($100\ \mu m$ fot TiN) is comparable to that in [7] ($50\ \mu m$ for gold, and $120\ \mu m$ for silver) for $\lambda = 1.6\ \mu m$ and d_2= $0.4\ \mu m$. L_{prop}= $100\ \mu m$ obtained for TiN is in the acceptable required range for the dense integrated photonic devices.

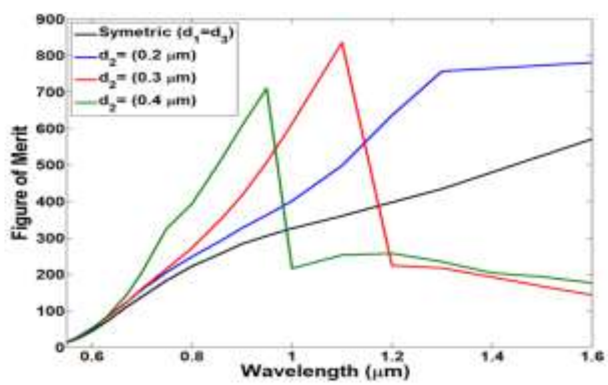

Figure 5. Variation of FOM with the wavelength for symmetric and asymmetric two trenched CPP waveguides at d1 = 0.6 μm and different values of d2.

3. CONCLUSION

Designing of green optical network is the highest priority of many research groups. Proposing a new model of CPPs waveguide that addresses the sustainability issue of the plasmonic groove waveguides was the main theme of this work. TiN based CPPs waveguide was proposed and simulated. The dispersion characteristics of the proposed material were examined over a range of frequencies from 200 to 550 THz. The propagation length, mode confinement loss and FOM were calculated and compared for symmetrical and asymmetrical designs. The result showed that introducing the asymmetry of the trenches is highly improving the performance of the CPPs waveguide. Comparison of the TiN based CPPs waveguide with the previously published results for gold and silver CPPs waveguide showed a little reduction in the FOM. However, the proposed material provides a low cost and stabilized chemical and physical properties compared to the gold and silver metals.

REFERENCES

[1] R. Mansoor and A. H. AL-Khursan, "Numerical modelling of surface plasmonic polaritons," Results in Physics, vol. 9, pp. 1297-1300, 2018.

[2] R. D. Mansoor et al, "Over coupled ring resonator based add/drop filters," Quantum Electronics, IEEE Journal Of, vol. 50, (8), pp. 598-604, 2014.

[3] H. A. Atwater, "The promise of plasmonics," Sci. Am., vol. 296, (4), pp. 56-62, 2007.

[4] N. Liu et al, "Plasmonic analogue of electromagnetically induced transparency at the Drude damping limit," Nature Materials, vol. 8, (9), pp. 758, 2009.

[5] H. A. Atwater and A. Polman, "Plasmonics for improved photovoltaic devices," Nature Materials, vol. 9, (3), pp. 205, 2010.

[6] A. M. Heikal, M. F. O. Hameed and S. S. Obayya, "Improved trenched channel plasmonic waveguide," J. Lightwave Technol., vol. 31, (13), pp. 2184-2191, 2013.

[7] F. F. K. Hussain et al, "Dispersion characteristics of asymmetric channel plasmon polariton waveguides," IEEE J. Quant. Electron., vol. 50, (6), pp. 474-482, 2014.

[8] A. B. Fallahkhair, K. S. Li and T. E. Murphy, "Vector finite difference modesolver for anisotropic dielectric waveguides," J. Lightwave Technol., vol. 26, (11), pp. 1423-1431, 2008.

[9] G. V. Naik et al, "Titanium nitride as a plasmonic material for visible and near-infrared wavelengths," Optical Materials Express, vol. 2, (4), pp. 478-489, 2012.

[10] I. Lee et al, "Dispersion characteristics of channel plasmon polariton waveguides with step-trench-type grooves," Optics Express, vol. 15, (25), pp. 16596-16603, 2007.

[11] A. Vial et al, "Improved analytical fit of gold dispersion: Application to the modeling of extinction spectra with a finite-difference time-domain method," Physical Review B, vol. 71, (8), pp. 085416, 2005.

environments
MDPI

Article

Comparison between Three Off-Grid Hybrid Systems (Solar Photovoltaic, Diesel Generator and Battery Storage System) for Electrification for Gwakwani Village, South Africa

Miriam Madziga [1], Abdulla Rahil [2,*] and Riyadh Mansoor [3]

[1] Faculty of Technology, De Montfort University, Leicester LE1 9BH, UK; mmadziga@yahoo.co.uk or P12238308@my365.dmu.ac.uk
[2] Institute of Energy and Sustainable Development (IESD), De Montfort University, Leicester LE1 9BH, UK
[3] Engineering College, Al-Muthanna University, Samawa, NA, Iraq; riyadhdmu@mu.edu.iq
* Correspondence: P13063959@my365.dmu.ac.uk; Tel.: +44-116-250-6848

Received: 12 March 2018; Accepted: 2 May 2018; Published: 8 May 2018

check for updates

Abstract: A single energy-based technology has been the traditional approach to supplying basic energy needs, but its limitations give rise to other viable options. Renewable off-grid electricity supply is one alternative that has gained attention, especially with areas lacking a grid system. The aim of this paper is to present an optimal hybrid energy system to meet the electrical demand in a reliable and sustainable manner for an off-grid remote village, Gwakwani, in South Africa. Three off-grid systems have been proposed: (i) Photovoltaic (PV) systems with a diesel generator; (ii) Photovoltaic systems and battery storage; and (iii) Photovoltaic systems with diesel generator and battery storage. For this analysis, different size of photovoltaic panels were tested and the optimal size in each scenario was chosen. These PV sizes were 1, 0.8, 0.6 and 0.4 kW. The optimization between these sizes was built based on three main objectives. These objectives are: (i) energy demand satisfaction; (ii) system cost; and (iii) pollution. For the first and second system scenarios, the optimal size was the 1 kW with battery and 1 kW with diesel generator; the third scenario results did not sufficiently match the three objectives. A general comparison has been carried out between the two optimal systems when the diesel generator is used and when the battery is applied. Both scenarios can sufficiently meet the demand without any considerable interruption, but disparities exist between them in relation to cost and technical optimization. There is a huge difference in the cost between these scenarios. The total cost in PV-Battery system (Scenario 1) represents only 26% of the entire PV system. Also, the PV and Battery system does not release any harmful emissions compared with nearly 6 tCO_2/year in the PV with Diesel system (Scenario 2). Also, Scenario (3) is a viable option in terms of energy production but costs more and is proposed to be more beneficial using an economies-of-scale analysis.

Keywords: renewable energy; off-grid; hybrid; photovoltaic with battery; photovoltaic with diesel; Gwakwani; South Africa

1. Introduction

Recently, Hybrid Renewable Energy Systems (HRES) have gained reputable popularity, and garnered momentum among research studies for modelling, simulation, and optimization. This is a system which combines two or more renewable and/or non-renewable energy sources. The main drivers of a HRES are costs associated with conventional/traditional energy systems, reduction of emissions, negative impact on health and environment and optimization of systems [1,2]. The current global deviation from fossilized remains of dead plants and animals (which are considered non-renewable resources) formed over extensive heat and pressure formation on the earth over millions of years [3] to renewable resources has further enhanced research in this area. The use of fossil fuel is widespread in South Africa, for electrification, cooking, daily living and practical uses and its emission of toxic gases into the atmosphere accounts for global warming issues and challenges. The key contributing factor of the HRES is deviation from overexertion of fossil fuel sources and its negative impact to the environment, in relation to the financial costs, commitments and access associated with it. The burden of costs of installation of large energy plants and equipment is reduced (which is often borne by the government on a macro level) and passed on to a lower-cost alternative solutions using renewable resources [4]. The overall system reliability and performance levels is higher for areas with an abundance of solar irradiation, HRES and resources [5].

The HRES also have the potential for energy balancing of systems, stability, and reliability for areas with little or no access to electricity, with the design and modelling of the HRES unique to each case study. Ongoing research and investigation persists in improving its efficiency, performance, and integration with renewable energy sources such as solar, wind and other renewable energy technologies. However, the design is usually aimed at solving an optimization problem. An exact one-size-fits-all solution is not realistic, due to the number of dynamic variables, complexities, and non-linearity in performance of systems. Therefore, the defining terms for optimal solution in a case study vary as a function of energy balance and management, support of existing infrastructure, optimal sizing of system and component parts, control strategies, and so on as stipulated by location and researcher [3,6,7]. The process of achieving optimal conditions, through operation and component part selection, can be determined through multiple techniques. There is a numerical algorithm-based technique for unit sizing and cost analysis, an algorithm-based energy technique to size the photovoltaic (PV) elements, a software modelling technique, a linear programming technique, a probability technique, an iterative technique, analytical model, dynamic technique, and multi-objective genetic algorithm technique, etc. [2,4,8–11].

In the development of the HRES using wind and solar PV, the state of design, operation, control requirement, performance analysis of demonstration systems and development of efficient power converters was examined, and it was observed that the total life costs were significantly reduced. The combination of energy sources proved to be a more reliable source of electricity supply and this reduced the battery bank and diesel requirements all together [10]. In another study of the HRES, the design process was leveraged using different component parts for minimizing lifecycle costs, and a criteria selection was determined to produce a combination of trade-off between reliability, costs, and minimum use of diesel generator sets [6–8,12–16]. The optimal combination point was determined at a unit cost of Rs. 6.5/kWh for the case area where the micro-wind-hydro system was found to be the optimal combination for electricity. This maintains a 100% renewable energy source while eliminating the diesel generator [17].

The feasibility analysis of a wind-hydrogen system for Grimsey Island to generate electricity for the location is examined for optimal system solution in another three scenarios: design analysis of wind-diesel, wind-diesel-hydrogen and wind-hydrogen systems. The overall result suggests the order of installation of scenarios in succession from a wind-diesel system, to a wind-hydrogen-diesel system and then a wind-hydrogen system, with that hierarchy [18,19]. It is observed that in a 20-year period, the system running costs were significantly reduced, although not without substantial investments at the onset. From a practicality standpoint, the wind-hydrogen-diesel system had the lowest operational cost from the configuration design of the three scenarios [20]; also, speculation on changes in oil price and costs of renewable technology is cited as a major determinant for the future direction of renewables systems, progressively or otherwise. The roadmap of the study highlights the practical application of the system to real-life situations, with the result of achieving 100% renewable electricity less likely, for now, due to other contending factors examined simultaneously within the system design. In multiple studies of the techno-economic feasibility of hybrid systems, optimizations techniques and modelling, the most viable option is predetermined by examining and evaluating the potential of available energy sources to location. The specific details of the results are not mentioned here but overall the result indicates strong potential for renewable energy production especially—from solar energy for electrification to wind power for hydrogen production [21–25].

The slow adoption of the HRES has been attributed to its high costs [26]; it is essential to select the appropriate system size in a techno-economic analysis to determine the costs associated with this.

Though the HRES is considered a more sustainable option to fossil fuel resources as it has less negative environmental impact and greater reductions of global warming. The HRES is also considered very challenging in its design, especially for PV, wind, diesel generators and energy storage systems due to many variable factors and much uncertainty [11,27]. The renewable resources are argued to be unpredictable in some areas in relation to its intensity and energy-generating component, such as sunshine and wind speed and wind direction; the major concern lies within its ability to satisfy demand which is often cushioned with energy storage units as backup.

Despite the measures taken to ensure accuracy, this unpredictability makes it necessary to run a feasibility and performance design for each case area. In the optimization of PV/Wind/Diesel Generator and energy storage units, the first step was a design to optimize all the component parts to achieve minimum costs while satisfying energy demand [11]; it manages the customer demand side response for energy demand effectively and efficiently, as it often requires an estimation of the HRES when compared to the standalone traditional energy systems to further ensure its cost effectiveness. This is the case for Barwani, India where the stability and cost effectiveness of the PV/Wind/Biomass hybrid solution was achieved through a practical application of system where the control strategy, techno-economic analysis and social effects were considered [28].

In the optimization of PV-biomass-diesel and grid base hybrid energy systems for rural electrification using HOMER Pro Software tool developed by the National Renewable Energy Laboratory (NREL), Golden, CO, USA, this study examined the economic impact of a decentralized renewable energy base system with no grid extension for Jhawani village, Tezpur area, India. The design was optimized by configuring different load profiles, costs of energy at different peak loads, energy demand profile and grid availability [29,30]. The electricity costs depend on load factor, which has an inverse relationship between peak load/energy demand and cost of electricity generation. The comparison between grid extension and off-grid is a matter of economic perspective in decision-making. Overall, the hybrid energy system is a feasible reliable source, and the result shows the optimal scenario to be the biomass gasification system rather than a photovoltaic system. There is also an emphasis on the unforeseen challenges that may arise from practical application of proposed configurations. An analyzed performance rate of off-grid wind-PV-diesel-battery hybrid energy system was feasible for remote areas of Selangor, Malaysia. The system design considers a load size profile of 33 kWh/day and peak load of 3.9 kW, net present economic costs, available energy sources and size, and CO_2 emissions. The net present costs and CO_2 emission can be reduced by 29.65% and 16 tons per year in comparison to the conventional power plants; it can be applicable to areas with similar climatic conditions. It is environmentally and economically feasible in the long-run to replace the conventional plants with the renewable plants [31].

2. Materials and Methods

The central energy source for this study is Solar PV, though there are different factors which determine the PV outcome such as solar irradiance level, intensity, optimization of PV, energy load, design spacing of PV cells, tilt, angle, etc. These factors must be considered as PV efficiency decreases with an increase in cell temperature and solar irradiance and areas of concentration [18]. Detailed analysis and test conditions of various PV arrays was not considered in this study; a generic flat panel PV is used as configured within the HOMER Pro software (Version 3.11.1) developed by NREL, Golden, CO, USA. The functional operation can be further analyzed in a comparative assessment of the performance levels of solar PVs and other resources in a standalone system, for grid connection and HRES. The PV system as a standalone is time sensitive and seasonal unit which yields considerable output when the solar irradiance is highly intense and reliable, depending on the design of PV array. When the PV standalone system is compared with a stand-alone biomass energy system, the biomass system has a higher efficiency and lower costs in rural areas while the PV system decreases in its performance output with a significant difference in its levelized cost of energy (LCOE) for certain areas [18,32].

In the PV system for a grid-connected system, it reduces its dependence on a diesel generator and utilizes the power generated by saving energy in a storage unit. PV/diesel generator/battery is considered more economical more beneficial for electrification as seen in a study of northern Nigeria, [31] but this is not the case for Gwakani village.

The provision of electricity and energy by the South African government prioritizes by demographics, geographical regions and areas of higher economic value which perpetuates trade, commerce, and industry [33]. With the growing population of South Africa and interconnectedness of the global community at large, this makes the demand for electrification imminent. This is not only a major concern for cities and urban areas but also rural, local communities and small villages in South Africa which require energy resources and electrification for daily living. In a forecast projection of electrification for South Africa from 2014 to 2050 [34], the supply and demand pattern from electrification and the driving forces are unique and particular to South Africa, part of which remains socio-cultural and socio-political. Despite the challenges, local communities are continuously embracing technological advancements and seeking alternative solutions. This is predominantly evident with the various users of HRES at household level [35]. This framework designs the optimal functional and cost-beneficial system model for Gwakwani village, by estimating the energy demand and time constraints for optimality, costs incurred and overall benefits. The use of renewable resources, though beneficial in the long run, usually require an investigation into the framework for design and establishment. It is important to understand HRES scenario dynamics, reliability, expected outcomes, possibilities, and potential before fully investing into HRES. The flexibility it offers ensures for easier calibration of the system.

2.1. Data Collection

The collection of data is derived from primary and secondary sources—literature reviews and demographical distribution the case study. Data for renewable energy sources are retrieved from NASA, 2017 accessed within the NREL Database System in real time.

Gwakwani is a small rural village in the northern part of the Limpopo province in South Africa located on latitude 22°34.3′ S and longitude 30°48.2′ E. There are between 70 and 100 people living in the village and this is projected to decrease gradually due to socio-economic strain, and challenges with electricity and telecommunications as people migrate to urban settlements where their needs are met. There is very little information about this rural village; however, the relevant data collected via literature indicates the demand need for electrification to the village, particularly for sustenance. The data collection of solar energy availability potential energy requirement and cost assumptions were determined [36–38].

2.1.1. Solar Radiation

Solar radiation data for specific location can be extracted by different means; for example, solar radiation can be obtained from metrological stations that are distributed across the country in question or it can also be extracted by transporting the latitude and longitude figures of the region into the NASA (2017) portal found on the website. The same steps are applied for calculating the PV watts as provided by the NREL, the U.S. Department of Energy, 2017 and the South African Weather Service, 2017. Solar radiation for the region of study are obtained from South Africa Meteorological Organization, 2010 [39,40]. The global solar radiation data for Gwakwani is shown in Figure 1 which highlights the pattern by hour of the day and day of the year. It shows January to March and September to December as the peak months for solar radiation while from April to August exhibits the lowest solar radiation [41–43].

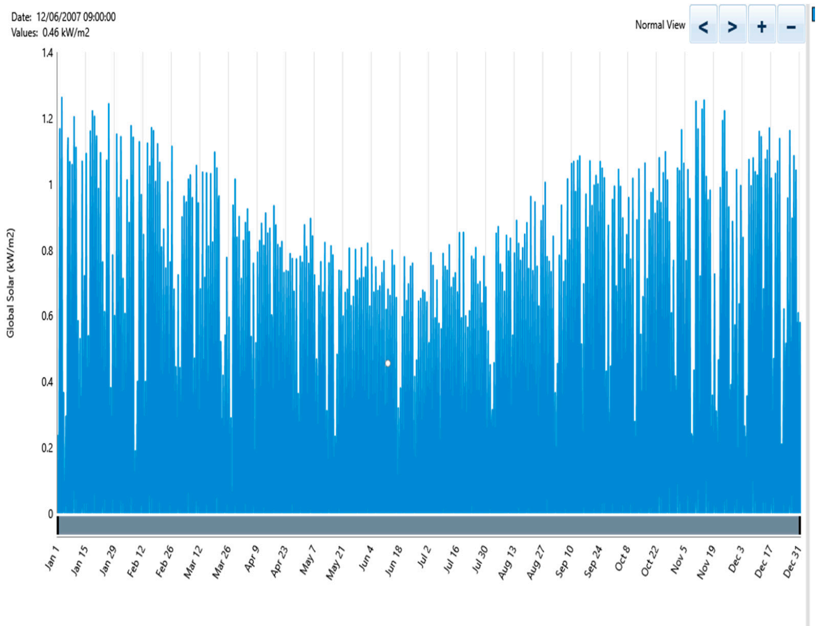

Figure 1. Yearly solar irradiance pattern for Gwakwani area.

There are between 70 and 100 people living in this village with no electricity and a very simple lifestyle. This village has few activities that require electricity beyond a few hours of lighting for houses (preferably during night time hours), mobile phone charging and water pumping for water production. Figure 2 below is a background into the simple lifestyle in Gwakwani area.

(**a**)

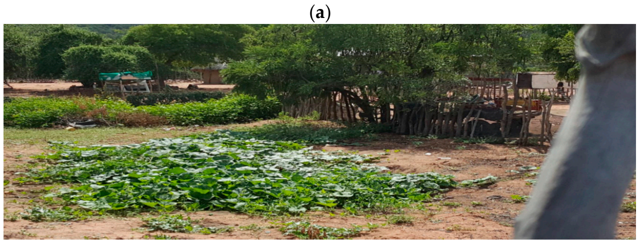

(**b**)

Figure 2. Housing and agriculture activities in Gwakwani village. (**a**) Cross section of Gwakwani village; (**b**) Cross section of agricultural farm.

The village is assumed to have on average 17 houses. The size of houses are unknown, therefore simple arithmetic assumptions are made to enable the demand estimation. It is assumed that this village runs community-based living and the rules of engagement within a community apply and are imposed. The local type of employment is predominantly simple agriculture which requires minimal irrigation and animal husbandry. The electrical demand will be required for lighting, mobile phone charging and water pumping. One mobile cell phone is assumed for each household, and one lamp per household is assumed for electricity supply. One water pumping device is assumed for the entire village and this is run for 3 h.

Table 1 below will summarize the energy demand during the day based on the above appliances and their time of operation.

Table 1. Electricity consumption devices and its energy consumption.

Device	Load Point in Village	Rating (W)	Load (W)	Operation Time (h)	Load Duration (h)	Energy Demand (Wh/day)
Lighting [5,6,9]	17	20	340	17:00–21:00	5	1700
Mobile Phone [23]	17	25	425	7:00–10:00	3	1275
Water pumping [34]	1	598	1196	7:00–10:00	3	3588
Total	35	643	1961	10	11	6563

The hourly demand of the village is shown in Figure 3 below. As it is presented, the electricity required will be operational during two periods of the day—morning and evening time. Adding more appliances such as a television set as a communal social gathering for the village is a plausible option due to the surplus power generated.

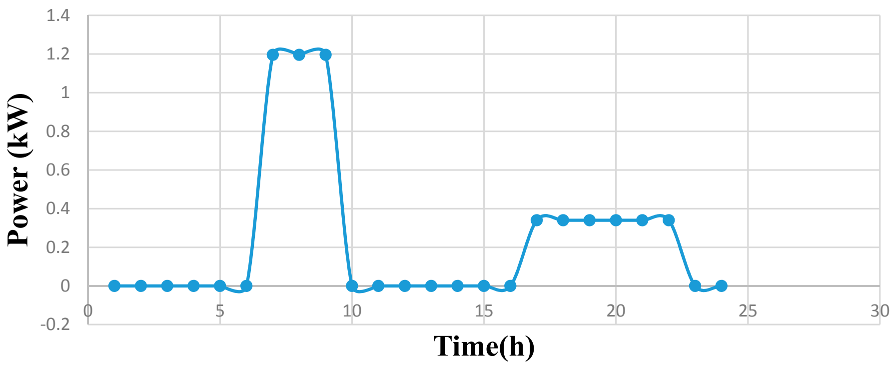

Figure 3. Hourly demand for Gwakwani based on the aforementioned devices.

2.1.2. Energy Demand

In the Morning between the hours of 7 a.m. and 10 a.m. (3 h) the total demand is 4863 W/h/day and in the Evening the total demand is 1700 W/h/day (as shown in Table 1 above).

The average energy consumption is 1.2 kW. This is required for Mobile Charging and Water Pumping; while in the Evening between the 17:00 and 21:00 (4 h), the average energy consumption is 0.35 kW (this is required for Lighting purposes).

2.1.3. System Components and Cost Assumptions

In this paper, two different scenarios of operations will be applied to cover the electricity demand of this village. These scenarios are built based on three main points which are: (i) Reduce the system cost to the lowest possible value—the priority of the production will be given to renewable energy sources to decrease the system cost (ii) and reduce the emissions—considering the environmental impact on life and welfare; (iii) and providing electricity to consumers efficiently without interruptions. Based on these aforementioned conditions, two systems are suggested which are:

- Photovoltaic system plus diesel generator for the time shortages and night time (for daily usage).
- Photovoltaics system plus battery storage to store the excess energy produced via PV system and meet any deficiency periods and during the night (for daily usage).

2.2. Simulation

HOMER energy software from NREL is applied for the system simulation. The software can be used for different energy management scenarios such as off-grid, on-grid, and mini-grid systems. The main points of the paper can be investigated running this software as it assesses the system based on a techno-economic view. In this paper, three different systems are designed using the main energy source (PV) and applied in a scenario to verify the best optimal solution for the village in a cheaper sustainable way [23].

1. In the first scenario the PV system with battery to store excess energy is used to meet any demand shortages. Four PV sizes are tested, and the optimal sizing is selected and compared with the second scenario.
2. In the second scenario the PV system and diesel generator is added. The shortages during operation are matched using a diesel generator. The same four PV sizes used in the first scenario are applied and tested here and the optimal sizing is also selected and compared with the first scenario.
3. In the third scenario, the PV system and both the diesel generator and battery storage unit are added, and four PV sizes are tested. The load following dispatch strategy ensures that the generator produces only enough power to meet the load as the optimal system is more efficient in renewable powered systems which exceeds the load. HOMER automatically turns the generator off, if the load is supplied by other renewable sources [10,16,37].

Finally, a comparison between the optimal solutions in the first, second and third scenarios have been presented. The criteria established between those two scenarios are: (a) the system cost; (b) the renewable energy penetration; and (c) the demand satisfaction. The figures below show the three model scenarios.

(a) Photovoltaics System plus Battery Storage

This scenario consists of PV system and battery storage without any conventional electricity sources such as a diesel generator. Different sizes of PV system are tested and the optimal solution selected to compare with other scenarios. The PV will satisfy different purposes at the same time to satisfy the demand and to charge the battery for Evening time or periods with shortage of PV power. In this scenario the total energy supply to village is supplied via PV system either directly from the PV to the load or indirectly from the battery to the load. Technical and economical details of all components including battery and PV inverter are presented in Table 2 below. This scenario has two advantages in comparison with the previous scenario, which are environmental friendliness and being totally self-dependent since there is no need to travel long distances to buy diesel fuel. The autonomous hybrid PV/battery power system considered is a combination of a PV array, battery bank, direct current DC/DC and alternating current AC/DC converter, DC/AC inverter, DC, and AC load as shown in Figure 4.

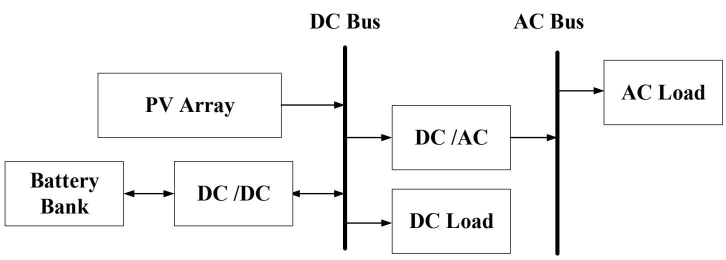

Figure 4. Block diagram of autonomous hybrid PV/battery storage system.

(b) Photovoltaic System plus Diesel Generator

This scenario consists of a photovoltaic system plus diesel generator, with different PV system sizes tested. These sizes are 1 kW, 0.8 kW, 0.6 kW and 0.4 kW. Then the optimal PV size is compared with the optimal PV size of other scenarios. The PV system supplies the demand during the daytime and any other surplus power is wasted because of the absence of energy storage. Any deficiency in meeting the demand leads to the diesel generator being run, even during the daytime. In this case, the diesel generator has the potential to meet the total demand load due to full rate operation of diesel generator while all PV power production is curtailed or dissipates. Technical and economical details of diesel generator and PV are presented in Table 2 below. The autonomous hybrid PV/diesel power system considered is a combination of a PV array, diesel generator, direct current DC/DC and alternating current AC/DC converter, DC/AC inverter, DC, AC load as shown in Figure 5.

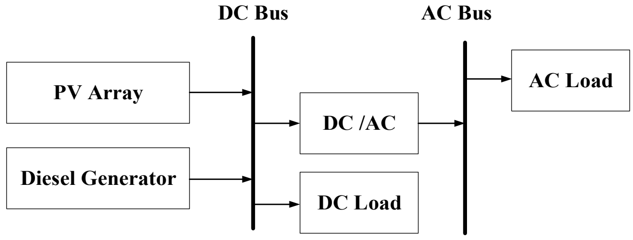

Figure 5. Block diagram of autonomous hybrid PV/diesel generator system.

Table 2. Component parts and characteristics.

Components	Specification	Description
PV array	Size	1, 0.8, 0.6, 0.4 kW
	Capital Cost	$300
	Replacement Cost	$200
	O&M Costs	$200
	Lifetime	5 years
Diesel generator	Size	Auto size to Load (500 kW)
	Capital Cost	$1500
	Replacement Cost	$200
	O&M Costs	$200
	Lifetime	15 years
	Fuel Cost	1.75 $/L
Battery	Type	Lead acid
	Nominal Voltage	12 V
	Nominal Capacity	1 kWh
	Maximum Capacity	83.4 Ah
	Round Trip Efficiency	80%
	Capital Cost	$300
	Replacement Cost	$300
	O&M Costs	$10 year
Converter	Size	1 kW
	Capital cost	$300
	O&M cost	$60/year
	Replacement Cost	$300
	Efficiency	95%
	Lifetime	16 years
Project Lifetime	25 years	
Carbon Emission Factor	0.957 tCO_2/MWh in 2010	
Interest Rate	5%	
Fuel Heating Value	45 MJ/kg	

(c) Photovoltaics system, Diesel Generator plus Battery Storage

This scenario consists of photovoltaic system plus diesel generator and battery storage unit. The autonomous hybrid PV/diesel power system considered is a combination of a PV array, diesel generator, battery storage unit, direct current DC/DC and alternating current AC/DC converter, DC/AC inverter, DC, and AC load as shown in Figure 6. This scenario consists of a photovoltaic system plus diesel generator and battery storage which analyzes the different PV system sizes of 1 kW, 0.8 kW, 0.6 kW and 0.4 kW. The Load Following (LF) dispatch strategy is used as this enables the production of only enough power to meet the primary demand load of (6663 Wh/day) while the generator is in operation. The lower priority objectives such as storage bank and serving the deferrable load are left to the renewable power sources [12,16,17]. The deficiency in meeting the demand load activates the diesel generator which runs continuously until the storage unit is full (which usually requires an increase in storage unit size).

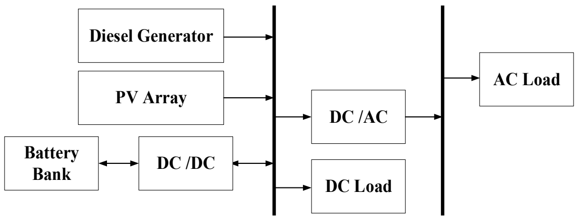

Figure 6. Block diagram of autonomous hybrid PV/diesel generator system/battery storage.

2.3. *System Components*

1- PV Module

In HOMER, the PV panels generate DC electricity in direct proportion to the solar radiation, independent of its temperature and voltage to which it is exposed. The output power of PV can be computed using the equation below.

$$P_{PV} = W_{PV} f_{PV} \frac{G_T}{G_S} \tag{1}$$

where W_{PV} the peak output power of PV system is (kW), f_{PV} is the PV panels derating factor (%), G_T is the solar radiation incident on the PV system in the current hour $(\mathrm{kW/m^2})$, and G_S is the incident radiation under standard conditions $(1\ \mathrm{kW/m^2})$.

2- Diesel Generators

Diesel generators are used to meet the peak demand, mainly when there is no output power from the PV system. It is important to note that the Gwakwani residents usually travel long distances of approximately 5 miles to buy fuel which leads to an increase in the fuel price above the normal rates. As of 2017, the fuel price in South Africa is fixed at around 1 $/L. So, the price of 1.75 $/L is considered to cover the transportation cost. Capital cost, maintenance cost and replacement cost are presented in Table 2.

3- Battery

In this study, the lead acid battery model is utilized, which provides good features combined with low cost. The lifetime and efficiency of the battery are set as five years and 85%, respectively. More details are presented in Table 2.

4- Inverter

A converter purpose is to convert the dc power obtained from PV panel to ac power. Usually, a converter is rated based on the power of PV system selected and the typical convertor efficiency of 85%. Technical and economical details of the converter are given in Table 2.

Since the objective aim for PV-Battery (in Scenario 1) is to satisfy the demand load regardless of the source, the PV simultaneously operates two goals: meeting the demand and charging the battery for later use. Due to the absence of a diesel generator, the PV system is running most of time except for three plausible periods: (i) when there is no demand load in the Afternoon (between the hours of 11:00 and 16:00); (ii) When there is not enough solar radiation (which can potentially occur between March to September and (iii) when there is not enough storage space within the battery size capacity. In second scenario, if the PV system cannot meet the demand, the diesel generator should be operated. Once the diesel generator is running, there is no need to operate the PV system at the same time since the power will be dissipated. The diesel generator is running at full capacity at any time and its capacity is sized according to the demand which can easily meet the demand without PV system production. Stop running the PV system when the production cannot meet the demand due to two main points: the absence of the storage system in this scenario and reduce the PV cost and increase the system lifetime.

The characteristics of the component parts for the hybrid systems are summarized in Table below:

2.4. Net Present Cost of the System and CO_2 Emission Cost

The net present value can be calculate using Equation (2) below.

$$C_{NPC} = \frac{C_{ann,tot}}{CRF(i, R_{proj})} \quad (2)$$

where $C_{ann,tot}$: Total annualized cost; CRF : Capital recovery cost; R_{proj} : Project lifetime; i : Interest rate.

The total CO_2 emissions from hybrid system can be computed using Equation (3) below.

$$tCO_2 = 3.667 \times m_f \times HV_f \times CEF_f \times X_c \quad (3)$$

where tCO_2 : Total amount of carbon dioxide; m_f : Fuel quantity; HV_f : Fuel heating value; CEF_f : Carbon emission factor (ton carbon/TJ); X_c : Oxidized carbon fraction; Another point that should be taken into account is that every 3.667 g of CO_2 contains 1 g of carbon.

3. The Three Hybrid Model Scenario Results

Scenario (1) Hybrid Energy System with Battery; Scenario (2) Hybrid Energy System with Diesel Generator; Scenario (3) Hybrid Energy System with Both Battery and Diesel Generator

1. Hybrid energy system with battery

3.1. System Architecture of the Hybrid Energy System with Battery

In Figure 7 the model scenario shows the Hybrid Energy System when Battery is used which consists of the electric load at 6.56 kWh/day and the peak at 2.75 kW. It has a 1 kWh lead acid (LA) battery for storage with a size of 11 strings, a flat plate PV of 4.25 kW is used, a System Converter of 4.38 kW was added and the cycle charging (CC) dispatch strategy used was as it tends to be optimal in systems with little or no renewable power.

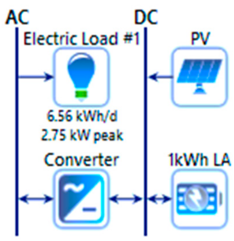

(a)

Figure 7. *Cont.*

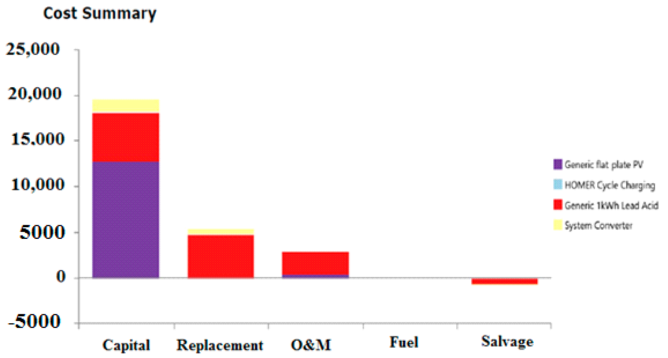

(**b**)

Figure 7. (**a**) Hybrid energy system with battery; (**b**) Cost summary.

The PV production is 7669 kWh/year, the consumption summary is 2394 kWh/year for AC Primary load and zero for the DC primary load. The excess electricity is valued at 4902 kWh/year and with an unmet electric load of 1.14 kWh/year. It also has a capacity shortage of 2.37 kWh/year. The levelized cost of Energy is $0.870 (kWh) and the total net present cost (NPC) is $26,916.03.

2. Hybrid Energy System with Diesel Generator

3.2. System Architecture of the Hybrid Energy System with Diesel Generator

The model scenario in Figure 8a below has an electric load of 6.56 kWh/day and 2.75 kW during peak hours. The PV array size is 0.00912 kW, the Diesel Generator Set of 500 kW is used with a system converter of 0.00651 kW and the dispatch strategy is set at cycle charging.

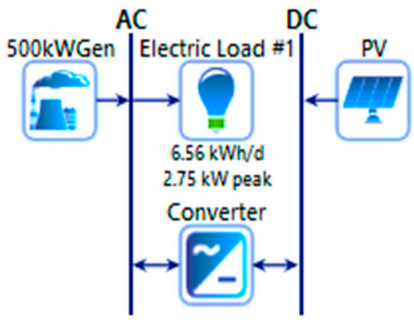

(**a**)

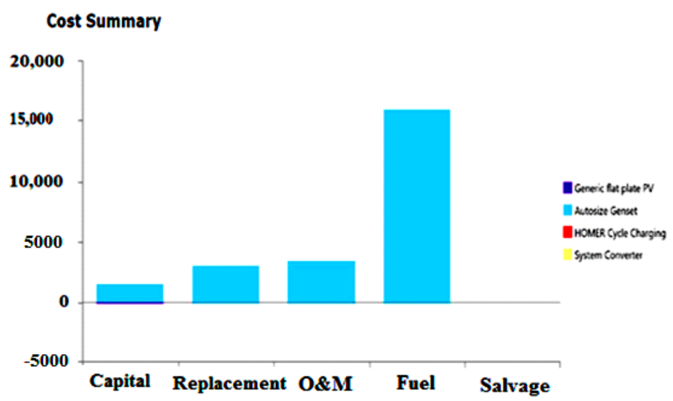

(**b**)

Figure 8. (**a**) Hybrid energy system with diesel generator; (**b**) Cost summary.

The Levelized Cost of Energy is $0.780 (kWh) and the total net present costs (NPC) is $24,166.58.

3.3. System Architecture of the Hybrid Energy System with Both Battery and Diesel Generator

In Figure 9 the model scenario shows the Hybrid Energy System when both Battery and Diesel Generators are used, which consists of the electric load of 6.56 kWh/day and the peak of 2.37 kW, a converter and solar PV. HOMER optimized the model scenario and produced a series of lower cost options of the overall costs associated with system. The results are presented below in Table 3. Below. The flat plate PV of 3.52 kW was determined as the optimum size to meet the demand load for the Gwakwani village with the diesel generator and the battery storage using the dispatch strategy of Load Following (LF). However, this scenario does not satisfy the objective optimal system requirement as mentioned earlier in literature of energy demand satisfaction, system cost and pollution in a sustainable manner. The system has a battery storage unit of 1 kWh Lead Acid Battery with a size of 18 strings and the Diesel Generator is at fixed capacity of 500 kW with a System Converter of 2.66 kW, CO_2 emissions of 295 kg/year, and a total net present cost of $140,970.60/year.

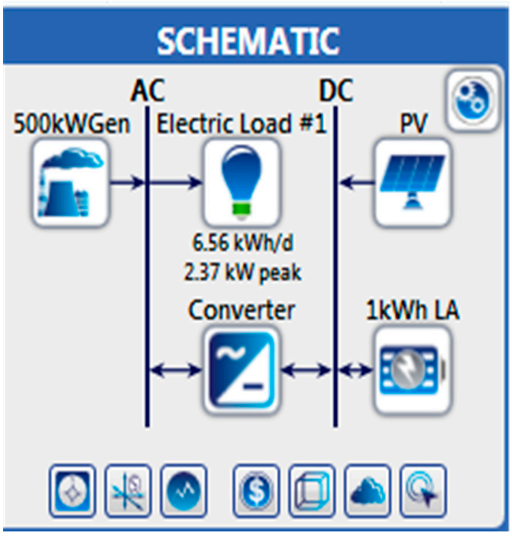

Figure 9. Hybrid energy system with diesel generator and battery.

Table 3. Cost Summary.

Annualized Costs	Capital	Operating	Replacement	Salvage	Resource	Total
Generic 1 kWh Lead Acid	$417.71	$180.00	$369.02	−$50.03	$0	$916.70
Generic 500 kW Fixed Capacity Genset	$11,603	$15.00	$0	−$2766	$112.50	$8965
Generic Flat Plate PV	$81.71	$704.19	$0	−$2.17	$0	$783.73
System Converter	$61.66	$159.42	$24.71	−$6.46	$0	$239.33
System	$12,164	$1059	$393.73	−$2824	$112.50	$10,905
Net Present Costs	**Capital**	**Operating**	**Replacement**	**Salvage**	**Resource**	**Total**
Generic 1 kWh Lead Acid	$5400	$2327	$4771	−$646.81	$0	$11,851
Generic 500 kW Fixed Capacity Genset	$150,000	$193.91	$0	−$35,754	$1454	$115,894
Generic Flat Plate PV	$1056	$9103	$0	−$28.12	$0	$10,132
System Converter	$797.12	$2061	$319.41	−$83.54	$0	$3094
System	$157,253	$13,685	$5090	−$36,512	$1454	$140,971

3.4. System Operation

Within HOMER software, there are sets of rules used to control generator and storage bank operation whenever there is insufficient renewable energy to supply the load. This is activated through a dispatch strategy technique of which there are two options: these are the Cycle Charging Strategy (CC) and Load Following Strategy (LF). The CC Strategy operates where the generator serves the primary load and operated in full output power, surplus electrical production goes towards the lower priority objectives in order of decreasing priority such as severing the deferrable load and charging the storage bank. In HOMER, the CC dispatches the controllable power sources (which are generators and storage banks for this design) each time step of the simulation in a two-step process. First, it selects the optimal combination of power sources to serve the primary load and the thermal load at the least total cost, while satisfying the operating reserve requirement. Secondly, HOMER maximizes the output of the generator in that optimal combination to its rated capacity, or as close as possible without producing excess electricity. While the operation within the LF Strategy produces only enough power to meet the primary load when a generator is in operation. The lower-priority objectives, such as storage bank and serving the deferrable load, are left to the renewable power sources [12,16,17].

4. Results

4.1. PV System with Battery for Energy Storage

Four different sizes of system have been applied and the result has been analyzed for every size. These sizes are 1 kW, 0.8 kW, 0.6 kW and 0.4 kW. The total amount of energy production during the year of each system size is shown in Figure 10 below. The demand load for the Gwakwani village is 6563 W/h/day (see Table 1). The PV is designed based on the demand load and the daily solar irradiation in Figure 1. The use of PV size 0.6 kW meets the demand load, as well as the other PV sizes 0.8 kW and 1 kW. However, the increase in PV sizes consequently leads to an increase in its economic costs.

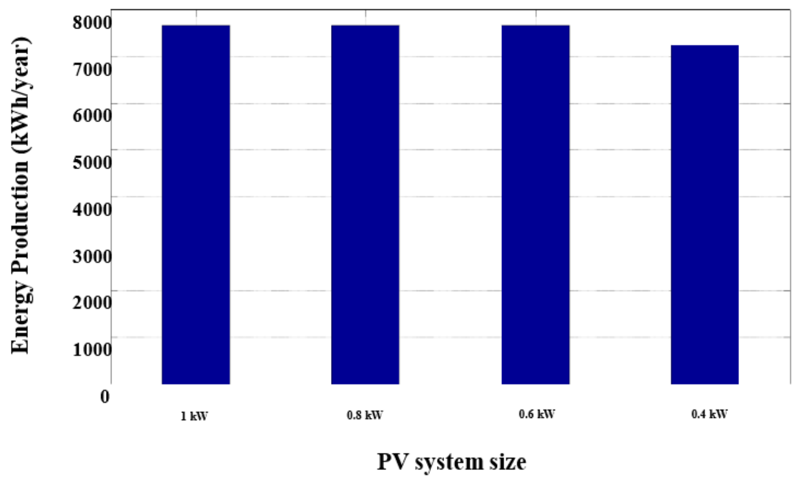

Figure 10. Energy production of different sizes of PV systems.

The cost difference between these scenarios mainly comes from the number and the O&M of the batteries in each scenario. For example, in the first scenario the 1 kW PV size activates the battery string at 18 cell while the 0.4 kW PV activates the battery string at 19 cell. In addition, due to the small size of the PV system in 0.4 kW and 0.6 kW, the battery will take more time to fully charge, which will lead to more operation and maintenance (O&M) cost. Degradation is the main issue of the battery and has a direct relation to the period of operation. The operation and maintenance cost were $2327, $2327, $2327, and $2456 for the 1 kW, 0.8 kW, 0.6 kW, and 0.4 kW respectively.

The O&M cost of the PV system also has an inverse relationship with the PV system size even though the operation costs per year (4388 h/year) for all sizes is the same. This possibility is because small sizes require more on-off connection to battery since it takes more time to fill the charge of battery. This interpretation shows the difference between lifetime throughput of the battery in each scenario since the large size has longer lifetime (11,234 kWh) compared with 11,666 kWh in 0.4 kW size. The rest of the calculations, such as the unmet demand, energy price and total system cost per size, are presented in Table 4.

Table 4. Summary of the system under different sizes of photovoltaics.

PV System Size	1 kW	0.8 kW	0.6 kW	0.4 kW
unmet demand (kWh/year)	1.14	1.14	1.14	1.22
energy price ($/kWh)	0.870	0.874	0.882	0.888
total net present cost ($/year)	26,916.03	27,053.39	27,311.95	27,484.29

The results reveal that changing the PV size does not strongly affect the main function of the system since the unmet demand remains the same during the other three sizes. The unmet demand is equal only for one day demand during the year. With regard to the system component part, a decrease in the system size led to an increase in cost and a corresponding increase in the system's battery size—which is required to meet any shortages due to the reduced PV size. Based on the calculation above, first size (1 kW) can be considered to be economically efficient to meet the demand in the village even though more surplus energy will be wasted due to the small size of battery. Alternatively, the next step would be to increase the size of battery but increasing the battery size will further increase the system costs as well.

Another option to combat this conundrum would be to introduce other household appliances to maximize the surplus energy for demand-side response by adding television and radio sets, etc. The highest energy price costs come from the energy storage cost. For example, in 1 kW, the levelized cost of energy produced via PV system is 0.134 $/kWh whereas the storage wear cost is 0.419 $/kWh. The rest comes from the annualized cost of other components.

4.2. PV System with Diesel Generators and without Battery

In this scenario the battery storage is replaced by diesel generator to meet the demand during the PV shortage times. The same PV system sizes are used as with the first scenario. These were tested, and two main points are observed even before the operation stage: the increase in CO_2 emissions due to the fossil fuel usage and the amount of renewable energy wasted is higher than the last scenario—because of the lack of energy storage equipment. It is important to note that the Gwakwani residents usually travel long distances of approximately 5 miles to buy fuel which leads to an increase in the fuel price above the normal rates. As of 2017, the fuel price in South Africa is fixed at around 1 $/L. Therefore, the price could be considered 1.75 $/L to cover the transportation cost.

In Figure 11 above, when 1 kW of PV system plus diesel generator is applied, the energy production is more than double other PV sizes due to the highest share of the PV system in the total production. Regardless of the PV sizes, 1 kW, 0.8 kW, 0.6 kW and 0.4 kW produced nearly the same amount of energy and most energy coming from diesel generator as shown in Figure 12 below.

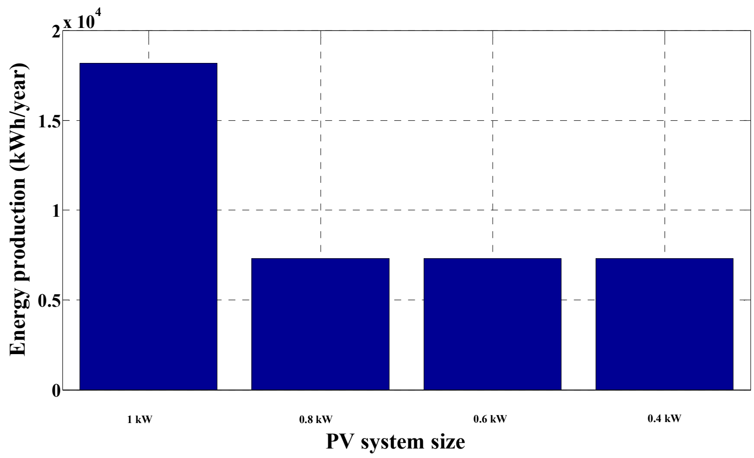

Figure 11. The sharing cost of each component of the system.

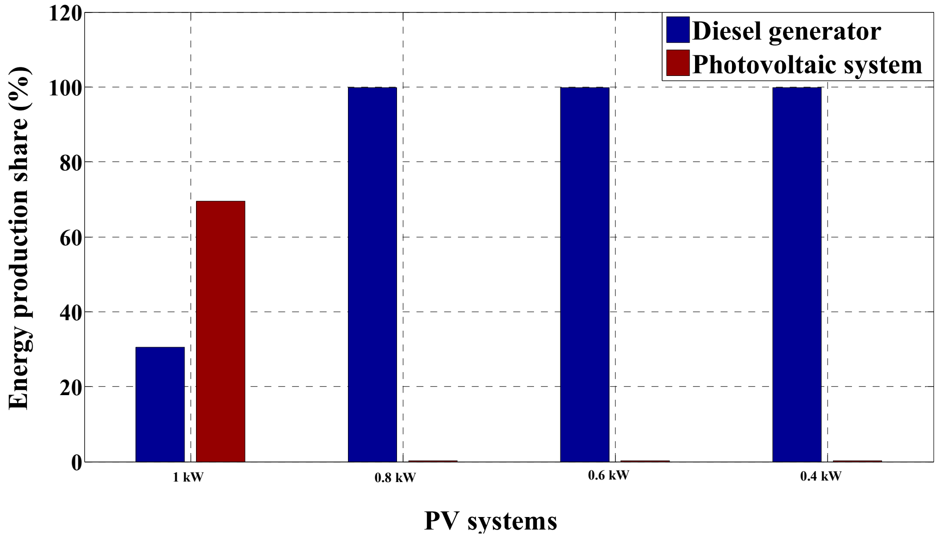

Figure 12. Energy production share of diesel generator and PV in each scenario.

The total power generated by the PV arrays when the diesel generator is added increases, and this uses the solar irradiance as retrieved for the case location of Gwakwani Village. The solar irradiance fluctuates throughout the year with the highest months from January to March, September to December, while it dips at its lowest months from 12 March to 10 September (see Figure 1).

The wasted energy is higher in 1 kW PV size compared with other scenarios due to the absence of energy storage equipment during the period of high PV productivity and low demand.

However, in other scenarios the surplus energy comes from a mismatch between the diesel generator production and demand since the diesel generator is operating at full capacity at any time of operation regardless of the required energy demand. The surplus energy is estimated to be 15,734 kWh, 4922 kWh, 4922 kWh, and 4922 kWh for 1, 0.8, 0.6, and 0.4 kW system sizes respectively; which is wasted without proper storage units. In terms of demand satisfaction, all scenarios can meet the total demand without any deficiency due to the sustainable and efficient source of energy (diesel generator). The cost details of the total system under different PV sizes are presented in Figures 13 and 14.

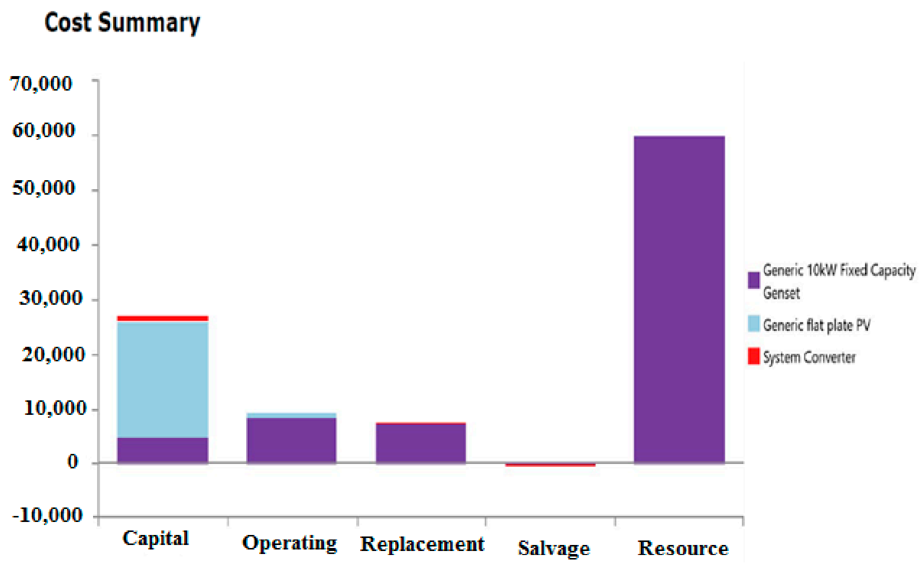

Figure 13. Cost summary of the system (1 kW PV).

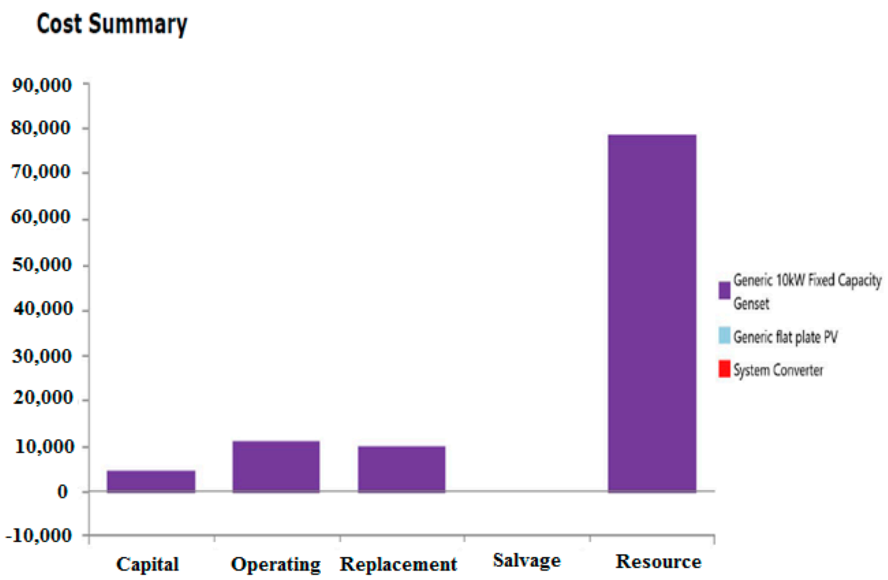

Figure 14. Cost summary of the system (0.8 kW PV).

There is a clear share of the 1 kW PV in the total capital cost of the system since the size is relatively high compared to other tested sizes and the PV. The PV system (1 kW) is responsible for nearly 60% of the total production. However, in other scenarios, most costs come from the diesel generator as in Figure 14 and the resources cost represents the highest part of the cost in both sizes since the fuel price is quite high. Other sizes will be same as in Figure 14. The effect of diesel operation on the environment can be considered as one of main disadvantage of this scenario, especially if the system extended to include more villages. More cost can be added to the system due to the emissions and based on the social carbon cost (SCC) of South Africa. The carbon dioxide (CO_2) is 6.9 ton/year for first year in contrast with 9.1 ton/year in other scenarios. The difference in emissions can be linked to the operation hours of diesel generator in each scenario. For 1 kW scenario, diesel generators were running for 2219 h/year whereas the running hours was estimated to be 2920 h/year. Finally, the average price of energy per kWh was 3.34 $/kWh in first scenario in contrast 3.4 $/kWh in other scenarios. To sum up, first scenario can be considered as a best optimum scenario based on the system cost, pollution levels and energy price. The first scenario has less surplus energy than scenario two, but slightly more surplus than scenario three. Scenario three has more CO_2 emissions than the first scenario and it also has a higher net present cost (see Table 5 below).

Table 5. Comparison between the operation of the three scenario hybrid energy systems—PV with Battery, PV with diesel generator and PV with both diesel generator and battery.

Caption	Photovoltaic with Battery	Photovoltaic with Diesel Generator without Battery	Photovoltaic with Both Diesel Generator and Battery
unmet demand (kWh/year)	1.14	0	0
energy price ($/kWh)	0.870	3.34	4.55
total net present cost ($/year)	26,916.03	$103,496.20	$140,970.60
surplus energy (kWh/year)	4902	15,735	3508
CO_2 emissions (kg/year)	0	6928	295

5. Discussion

HOMER Pro as used for this study analysis is distinctively different from HOMER Grid. It enables start-up designs for regions such as Gwakwani lacking in any form of variable data for analysis and connectivity and access to grid. The simulation results give an overview into the viability of a HRES with the potential for further expansion in a HOMER Grid, if the demand arises [10,23,29]. A simulation of the energy demand load requirement is necessary before the optimal planning design of the HRES and the configuration of the system is also dependent on the output power for generation and the load on the system [4,38]. It is important to consider the reliability status of the entire system, and while the reliability is considered to be relatively higher in a HRES (which is often a combination of both renewable and non-renewable resources), there is noticeably a considerable amount of savings on the total annualized costs associated with the system [18].

In HOMER, the distribution of the energy system is regulated by the dispatch strategy and controller systems, where the economic dispatch controllers CC and LF and are pre-set at default in HOMER and this enables the system design to match the load without any considerations for future adjustments. Due to this operational strategy (which is active only in the moment), the LF dispatch strategy of the diesel generators enables it to produce just enough power to serve the load, without producing any surplus energy [28]. While in the CC dispatch strategy, the generators produce as much power as required, without producing excess electricity and then further charges generators with the surplus power [23]. This allows the engine to operate storage and power sources to serve the load in a systematic way through a dispatch strategy, with the deferrable load of higher priority to battery charging. The dispatch strategies used in the three scenarios are:

- Scenario (1) PV-Battery: Cycle Charging (CC)
- Scenario (2) PV-Diesel Generator: Cycle Charging (CC)
- Scenario (3) PV-Diesel Generator plus Battery: Load Following (LF)

Comparison between PV-Battery Scenario and PV-Diesel Generator Scenario

The comparison will include only 1 kW PV system since this was observed as the optimal mode of operation in each scenario. Based on the result above, the operation of photovoltaic with the battery has many advantages in contrast with its operation with diesel generator. There is a clear difference in system costs and energy price per kWh between different scenarios, regardless of its economic advantages. The operation of the photovoltaics with battery has no emissions—and this can be an added feature benefit in environmental factors. The comparison summary between these scenarios is given in Table 5.

6. Conclusions and Future Work

Renewable energy-based off-grid rural electrification programs are one of the most effective ways to increase access to energy in remote areas of developing countries. In this paper, three scenarios of off-grid system have been investigated and compared to provide sustainable energy for a small village in South Africa. These scenarios are (1) PV-battery system, (2) PV-diesel generator and (3) PV—both diesel generator and battery system. Based on this research analysis both battery and diesel generator systems achieved the same objective function of backing up the PV system at periods of supply shortages. The four different PV sizes used in each model scenario indicated different optimal sizes and this was used as the rallying point for optimization. The optimal size selection satisfied the criteria conditions of: overall system cost, pollution emissions and demand satisfaction. As it is presented in the result section in scenario (1) the PV-Battery model—1 kW PV size was the optimal option between all sizes. The total cost of this size is the cheapest between all sizes which was approximately $26,916.03 compared with $27,053.39, $27,311.95, and $27,484.29 for 0.8 kW, 0.6 kW and 0.4 kW. This leads to the cheapest energy price per kWh between all sizes. Other advantages can be noticed in 1 kW size related to the demand satisfaction and battery degradation.

In scenario (2) the PV-Diesel Generator model, same size (1 kW) was the optimum in contrast with other scenarios. The power share of the PV system in 1 kW size is nearly 60% of the total energy produced whereas the share is nearly zero in other scenarios. In terms of the pollution, 6 tCO_2/year is released by 1 kW scenario compared with 9.6 tCO_2 in other scenarios. The only problem with this scenario is the wasted energy will be higher than other scenarios.

In scenario (3) the PV-Diesel Generator and Battery model, adequately satisfies demand with a surplus energy of 3508 (kWh/year) and energy price per 4.55 ($/kWh), the emissions rates however are 295 (kg/year) and the system net present costs at $140,970.60 ($/year).

The three model system scenarios can be used for electrification and match the energy demand at some considerable cost. The optimal solution however, ensures a more reliable cost-beneficial system as seen in scenario (1). The costs of adopting scenario (3) is not economically viable for a small village setting such as Gwakwani at $140,970.60 NPC, however the surplus energy per year of 3.508 (kWh/year) indicates the potential for cost minimization through the application of economics of scale, which is a more viable option. This would be more beneficial if the Gwakwani village had access and connection to a grid system to supply surplus energy at a fixed cost, to earn income and invariable reduce CO_2 emission. Thereby offsetting the initial capital investment costs of $157,253 in the scenario (3) model. Also, the combination of the PV-wind system is economically beneficial for remote areas with less than a daily load of 75 kWh/day and a load point of 50 km or more away from grid [18]. This situation is characteristic to the Gwakwani village with a daily load point of 6.56 kWh/day. With the source of sustenance of the Gwakwani village is farming and agriculture; biomass and wind are available renewable energy resources which can be further considered in a more detailed simulation analysis using biomass and wind turbine; based on the results, this can be added, swapped, or supplemented with the PV in a techno-economic assessment. Alternatively, this can be applied as a standalone system and compared. A simple tariff builder system can also be installed to evaluate costs per kWh of each family unit (in a demand-side response) to give allowance for any future increase.

Lastly, while the optimal sizes aim to satisfy three main conditions of system cost, pollution emissions and demand satisfaction, distinctive disparities exist between the model scenarios. The first and second scenario can sufficiently meet the demand without any a considerable interruption. The reliability of the system is significantly reduced in a HRES with an uneven power sharing control dynamic in the DC/AC Bus connection, which can occur when the system malfunctions in the DC/AC converter, since the main challenge of power sharing is to achieve a desired load distribution when the system is connected to a DC-bus configuration and the AC power is lost (due to malfunctioning) [4]. The size under PV-Battery scenario (1) does not release any harmful emissions compared with nearly 6 tCO_2/year in PV-Diesel scenario. There is a huge different in cost between these scenarios. The cost in PV-Battery represents 26% of the cost in PV-Diesel Generator scenario. In addition to all the mentioned differences that clearly support the PV-Battery scenario, there is a global trend towards enhancing renewable energy penetration and this approach requires a high capacity to store energy in several ways, including batteries, flywheels, and hydrogen. This will inevitably lead to a reduction in the storage technique prices. In contrast, the emission penalty is increasing, and most industrialized countries are trying to move away from conventional fuels to preserve the environment and build a strong and sustainable economy. Future research studies will include more appliances to accommodate the wasted energy, and different energy storage techniques can be tested and compared with batteries. A controller system dynamic model using either a MATLAB simulation or a combined dispatch algorithm which modulates start time, finish time and allows for an out-of-the-box controller algorithm which enables a flexible design to recalibrate itself in periods of higher energy demand, solar irradiation fluctuations and other unforeseen climatic challenges, storage and high emissions is proposed to actively choose between the LF and CC strategies at every step of the process.

Author Contributions: Conceptualization and Methodology, M.M. and A.R.; Software, M.M.; Validation, M.M., A.R.; Formal Analysis & Investigation, A.R. and R.M.; Resources, Data Curation, Writing-Original Draft Preparation, M.M. and A.R.; Writing-Review & Editing & Visualization, M.M., A.R. and R.M.; Supervision, R.M.; Project Administration & Funding Acquisition, M.M. & A.R.

Funding: This research received no external funding.

Acknowledgments: We would like to extend our gratitude to the NREL HOMER Pro Software management team, USA for the continued support and software update management and access and also, De Montfort University, Leicester for the opportunity to conduct this research study.

Conflicts of Interest: The authors declare no conflict of interest.

Nomenclature

CO_2	Carbon dioxide
CC	Cycle Charging
HRES	Hybrid Renewable Energy Systems
KM	Kilometer
kWh	Kilowatt Hours
kW	Kilowatt
LF	Load Following
LCOE	Levelized Costs of Energy
PV	Photovoltaic

References

1. Kolhe, M.; Ranaweera, K.M.I.U.; Gunawardana, S.A.G.B. Techno-economic sizing of off-grid hybrid renewable energy system for rural electrification in Sri Lanka. *J. Sustain. Energy Technol. Assess.* **2015**, *11*, 53–64. [CrossRef]
2. Qolipour, M.; Mostafaeipour, A.; Tousi, M.O. Techno-economic Feasibility of a Photovoltaic-Wind power plant construction for electric and hydrogen production: A Case Study. *Renew. Sustain. Energy Rev.* **2017**, *78*, 113–123. [CrossRef]
3. Hope, G.; Gilding, P.; Alvarez, J. *Quantifying the Implicit Climate Subsidy Received by Leading Fossil Fuel Companies*; Working Paper No. 2; Cambridge Judge Business School: Cambridge, UK, 2015.
4. Eltamaly, A.M.; Addoweesh, K.E.; Bawah, U.; Mohamed, A.M. New Software for Hybrid Renewable Energy Assessment for Ten Locations in Saudi Arabia. *J. Renew. Sustain. Energy* **2013**, *5*, 033126. [CrossRef]
5. Rahil, A.; Gammon, R.; Brown, N. Techno-economic assessment of dispatchable hydrogen production by multiple electrolysers in Libya. *J. Energy Storage* **2018**, *16*, 46–60. [CrossRef]
6. Hossain, M.; Mekhilef, S.; Olatomiwa, L. Performance Evaluation of a Stand-Alone PV-Wind-Diesel-Battery Hybrid System Feasible for a Large Resort Center in South China Sea, Malaysia. *Sustain. Cities Soc.* **2017**, *28*, 358–366. [CrossRef]
7. Iaquaniell, G.; Montanari, W.; Salladini, A. Standalone CSP-DG system for electrification of remote areas and desalinated water supply. *J. Sol. Energy* **2017**, *157*, 1056–1063. [CrossRef]
8. Koutroulis, E.; Kolokotsa, D.; Potirakis, A.; Kalaitzakis, K. Methodology for optimal sizing of stand-alone photovoltaic/wind-generator systems using genetic algorithms. *J. Sol. Energy* **2006**, *80*, 1072–1088. [CrossRef]
9. Kaur, T.; Segal, R. Designing Rural Electrification Solutions Considering Hybrid Energy Systems for Papua New Guinea. *J. Energy* **2017**, *110*, 1–7. [CrossRef]
10. Zahboune, H.; Zouggar, S.; Krajacic, G.; Varbanov, P.S.; Elhafyani, M.; Ziani, E. Optimal hybrid renewable energy design in autonomous system using Modified Electric System Cascade Analysis and Homer software. *Energy Convers. Manag.* **2016**, *126*, 909–922. [CrossRef]
11. Chang, K.-U.; Lin, G. Optimal Design of Hybrid Renewable Energy Systems using Simulation Optimization. *Simul. Model. Pract. Theory* **2015**, *52*, 40–51. [CrossRef]
12. Jose, L.; Bernal-Agustin, L.J.; Dufo-Lopez, R. Design and control strategies of PV-Diesel systems using genetic algorithms. *J. Sol. Energy* **2005**, *79*, 33–46.
13. Dufo-López, R.; Bernal-Agustín, J.L. Multi-objective design of PV–wind–diesel–hydrogen–battery systems. *Renew. Energy* **2008**, *33*, 2559–2572. [CrossRef]
14. Krishan, O.; Sathans. Design and Techno-Economic Analysis of a HRES in a Rural Village. *Procedia Comput. Sci.* **2018**, *125*, 321–328. [CrossRef]
15. Kim, H.; Jung, Y.T. Independent solar photovoltaic with Energy Storage Systems (ESS) for rural electrification in Myanmar. *J. Renew. Sustain. Energy Rev.* **2017**, *82 Pt 1*, 1187–1194. [CrossRef]

16. Sureshkumar, U.; Manoharan, P.; Ramalakshmi, A. Economic cost analysis of hybrid renewable energy system using HOMER. In Proceedings of the 2012 International Conference on Advances in Engineering, Science and Management (ICAESM), Tamil Nadu, India, 30–31 March 2012; pp. 94–99.
17. Amutha, W.M.; Rajini, V. Cost benefit and technical analysis of rural electrification alternatives in southern India using HOMER. *J. Renew. Sustain. Energy Rev.* **2016**, *62*, 236–246. [CrossRef]
18. Goel, S.; Sharma, R. Performance evaluation of standalone, grid connected and hybrid renewable energy systems for rural application: A comparative review. *J. Renew. Sustain. Energy Rev.* **2017**, *78*, 1378–1389. [CrossRef]
19. Ghaib, K.; Ben-Fares, F.-Z. A design methodology of stand-alone photovoltaic power systems for rural electrification. *Energy Convers. Manag.* **2017**, *148*, 1127–1141. [CrossRef]
20. Chade, D.; Miklis, T.; Dvorak, D. Feasibility Study of Wind-to-Hydrogen System for Artic Remote Locations—Grimsey Island Case Study. *Renew. Energy* **2015**, *76*, 204–211. [CrossRef]
21. Hosseinalizadeh, R.; Shakouri, G.H.; Amalnick, S.M.; Taghipour, P. Economic sizing of a hybrid (PV-WT-FC) renewable energy system (HRES) for stand-alone usages by an optimization-simulation model: Case study of Iran. *Renew. Sustain. Energy Rev.* **2016**, *54*, 139–150. [CrossRef]
22. Rahil, A.; Gammon, R. Dispatchable Hydrogen Production at the Forecourt for Electricity Demand Shaping. *Sustainability* **2017**, *9*, 1785. [CrossRef]
23. Singh, A.; Baredar, P.; Gupta, B. Computational simulation & optimization of a solar, fuel cell and biomass hybrid energy system using HOMER pro software. *J. Procedia Eng.* **2015**, *127*, 743–750.
24. Schenbel, C.; Zipperle, T.; Tzscheutschler, P. Modeling of industrial-scale hybrid renewable energy systems (HRES)—The profitability of decentralized supply for industry. *Renew. Energy* **2017**, *108*, 52–63. [CrossRef]
25. Sawle, Y.; Gupta, S.C.; Bohre, K.A. Review of hybrid renewable energy systems with comparative analysis of off-grid hybrid systems. *J. Renew. Sustain. Energy Rev.* **2017**, *81 Pt 2*, 2217–2235. [CrossRef]
26. Shezan, S.K.A.; Das, N.; Mahmudul, H. Techno-Economic Analysis of a Smart-grid hybrid renewable energy system for Brisbane of Australia. *Energy Procedia* **2017**, *110*, 340–345. [CrossRef]
27. Shafiullah, G.M. Hybrid Renewable Energy Integration (HREI) System for Subtropical Climate in Central Queensland, Australia. *Renew. Energy* **2016**, *96*, 1034–1053. [CrossRef]
28. Yang, Y.; Bremner, S.; Menictas, C.; Kay, M. Battery Energy Storage System Size Determination in Renewable Energy Systems: A Review. *Renew. Sustain. Energy* **2018**, *91*, 109–125. [CrossRef]
29. Rahil, A.; Gammon, R.; Brown, N. Dispatchable hydrogen production at the forecourt for electricity grid balancing. *AIP Conf. Proc.* **2017**, *1814*, 020011.
30. Voice of Africa News Forum Remote South Africa Village Gets Electricity for First Time—In 2014. Available online: https://www.voanews.com/a/remote-south-africa-village-gets-electricity-for-first-time---in-2014/1887672.html (accessed on 15 December 2017).
31. Adaramola, M.S.; Paul, S.S.; Oyewola, O.M. Assessment of Decentralized Hybrid PV Solar-Diesel Power System for Applications in Northern Part of Nigeria. *Energy Sustain. Dev.* **2014**, *19*, 72–82. [CrossRef]
32. Makukule, N.A.; Sigauke, C.; Lesaoana, M. Daily electricity demand forecasting in South Africa. *Afr. J. Bus. Manag.* **2012**, *6*, 3246–3252. [CrossRef]
33. Holloway, J.P.; Mokilane, P.; Makhany, S.; Magadla, T.; Koen, R. *Forecasts for Electricity Demand in South Africa 2014–2050 Using the CSIR Sectoral Regression Model*; Project Report Eskom; Council for Scientific and Industrial Research (CSIR): Pretoria, South Africa, 2016.
34. University of Johannesburg Gwakwani, the Forgotten People. Community Engagement Project. Available online: https://gwakwanielectrifyingaforgottenvillageinlimpopowordpress.files,wordpress.com/2016/05/gwakwani-project-presentation.pdf (accessed on 15 December 2017).
35. Belfkira, R.; Zhang, L.; Barakat, G. Optimal sizing study of hybrid wind/PV/diesel power generation unit. *J. Sol. Energy* **2011**, *85*, 100–110. [CrossRef]
36. Dufo-Lopez, R.; Bernal-Agustin, J.L.; Yusta-Loyo, J.M.; Dominguez-Navarro, J.A.; Ramirez-Rosado, I.J.; Lujano, J.; Aso, I. Multi-objective optimization minimizing cost and life cycle emissions of stand-alone PV-wind-diesel systems with batteries storage. *J. Appl. Energy* **2011**, *88*, 4033–4041. [CrossRef]
37. Yilmaz, S.; Dincer, F. Optimal Design of Hybrid PV-Diesel-Battery Systems for Isolated Lands: A Case Study for Kilis, Turkey. *Renew. Sustain. Energy Rev.* **2017**, *77*, 344–352. [CrossRef]

38. Mavroyeoryos, K.; Engonopoulos, I.; Tyralis, H.; Dimitriadis, P.; Koutsoyiannis, D. Simulation of Electricity Demand in A Remote Island for Optimal Planning of the Hybrid Renewable Energy System. *Energy Procedia* **2017**, *125*, 435–442. [CrossRef]
39. Lao, C.; Chungpaibulpatana, S. Techno-economic analysis of hybrid system for rural electrification in Cambodia. *Energy Procedia* **2017**, *138*, 524–529. [CrossRef]
40. Mamaghani, H.A.; Escandon, A.A.S.; Najafi, B.; Shirazi, A.; Rinaldi, F. Techno-economic feasibility of photovoltaic, wind, diesel and hybrid electrification systems for off-grid rural electrification in Colombia. *J. Renew. Energy* **2016**, *97*, 292–305. [CrossRef]
41. Shezan, S.K.A.; Julai, S.; Kibria, M.A.; Ullah, K.R.; Saidur, R.; Chong, W.T.; Akikur, R.K. Performance Analysis of an Off-grid Wind-PV-Diesel-Battery Hybrid Energy System feasible for Remote Areas. *J. Clean. Prod.* **2016**, *125*, 121–132. [CrossRef]
42. Sawle, Y.; Gupta, S.C.; Bohre, A.K. Review of Hybrid Renewable Energy Systems with Comparative Analysis of Off-Grid Hybrid System. *Renew. Sustain. Energy Rev.* **2018**, *81*, 2217–2235. [CrossRef]
43. Olatomiwa, L.; Mekhilef, S.; Huda, A.S.N.; Ohunakin, S.O. Economic evaluation of hybrid energy systems for rural electrification in six geo-political zones of Nigeria. *J. Renew. Energy* **2015**, *83*, 435–446. [CrossRef]

Synthesis and Characterisation of Polytetrafluoroethylene Composite for Electrical Insulation and Dielectrics

Laith M. Rasheed[1], and Riyadh Mansoor[2]

[1]College of Education, Al-Muthanna University, Samawa, Iraq.
[2]Engineering College, Al-Muthanna University, Samawa, Iraq.
r.m.2015@ieee.org

Abstract. This work provides an experimental study to measure the electrical properties of Polytetrafluoroethylene polymer and how it improves through the process of mixing with different volume rates of Poly (methyl methacrylate) PMMA. The relationship of the actual dielectric constant with frequency for pure and dopped models with different concentrations of PMMA (5%, 7%, 10%) and for a range of frequencies ranging between 1-1000 KHz, at the room temperature was investigated. The results show an increase in the dielectric constant of the composites compared to the pure models for all concentrations, which indicates that the polymers interaction gives support to the polytetrafluoroethylene infrastructure. The mixing process, also, leads to an increase in the values the imaginary part of the dielectric constant compared to the pure model, and this is due the significant increase in the number of dipoles resulting from the addition process which in turn led to increase the amount of energy lost due to rotation or friction of the dipoles with each other. This increase, in turn, led to a corresponding rise in the values of the loss tangent tanδ and the AC conductivity of the models. The experimental results show a 90 % increase in the dielectric constant of the composite at 500 KHz compared to the pure Polytetrafluoroethylene, which provide a good electrical insulation material for electronic circuits.

1. Introduction

Polymeric materials contain in their individual cases many defects that cause a limitation of use such as fragility, excessive stiffness, and fracture. However, these defaults can be eliminated or at least reduced by mixing it with other types of polymers to enhance the desirable characteristics [1].

Polymers today have the greatest impact for enriching our technology, as they have entered all fields of science; scientific research groups and companies are in a competition to introduce new materials and to obtain alternatives to some existing materials. Improving their properties and the knowledge of their internal structure as well as modifying the identity of its elements by adding atoms of other elements to it or removing /mixing atoms are examples of the research trends in the field of polymers now a days [2].

Polymeric composites are the physical blending of two or more polymers that resulting a composite which has the desirable mechanical or electrical properties [3]. The wide uses of polymers in technological fields have made it of a particular importance. This importance resulted from the fact that polymers generally exhibit different variations in its electrical and isolating behavior when it dopped or mixed with other materials. However, some engineering problems still exist for polymers such as their lack of stiffness and strength compared to minerals. Therefore, several methods have been used to improve these deficiencies such as fiber reinforcement method [4]. In this method, fibers are either continuous or random. Also, it can be in the form of particles, flakes, or laminates to improve the polymer properties.

Thin film technology [5] is the best way to give a clear idea of the physical properties of polymers; the term thin films is used to describe one or more layers of atoms of a thickness that does not exceeds one micrometre. The concept of thin films is to arrange the atoms of that substance in two dimensions, so that the third dimension is very small (in the order of the nanometers) called the thickness. The main difference between a substance in a solid state and a thin-film state is that substance in the solid state neglects the effect of surfaces on its properties while in the case of thin films it is exactly the opposite i.e. the effect of surfaces on properties is the most dominant. Although there are many techniques used to produce thin films, it can be categorized under two technical methods known as the physical and chemical methods. Of the most important methods used is the thermochemical pyrolysis method where the films are highly adherent to the base and have high stability in their physical properties with the time [6]. This is the method used in this study.

This method is performed by spraying the solution of the material from which the films are to be prepared with the help of a high-pressure air on a hot bases at a certain temperature depends on the type of material. The reaction between atoms of the substance and the hot base producing the films. Polymer blending is an important and widely used method to enhance the properties to obtain high dielectric constant compared to the values of these materials in its single case.

In this study, the electrical properties of some polymeric material that are known to be used as insulators are studied in order to obtain high dielectric values higher than that of any of those substances when they are in their single state.

2. Material used

2.1. Polytetrafluoroethylene (C2F4)

Also expressed as PTEF, is a synthetic polymer containing fluorine and is known commercially (Teflon) [7]. It is a non-flammable waxy solid produced from the polymerization of tetrafluoride. It needs at least 327 oC for melting and found with a density of 2200kg /m3. It has a very low coefficient of friction, so it is used in devices that do not require lubricants such as the lining of the equipment that are used to store and transport strong acids and organic solvents. Also, it is used as an electrical insulating material in addition to its common use for coating materials that are used in cooking which does not require the use of fats or oils because the substance does not flow easily above the melting point.

2.2. Poly (methyl methacrylate) PMMA

It is a colorless, transparent plastic material with high flexibility and transparency with a high refractive index. The chemical formula is {CH2C(CH3) COOH3}, melting point (213 oC), molecular weight (4000 gm / mol) and density (1.2 gm / cm3).

2.3. Dimethylformamide (DMF)

The molecular formula {C3H7NO}, molecular weight (73.1 gm / mol), boiling point 153 oC, and the density is (0.9445 gm / cm3).

3. Experimental setup

The density of the polymeric solutions is measured using a 25 ml density cannula and a digital scale type (Sartorius) with a sensitivity up to 1x10-4 gm by changing the mass to the size. While the gravimetric method was used to measure the thickness of the prepared films using the sensitive scale. The film is weighed before and after sedimentation, the difference is calculated, and the following relationship is used

d= $\Delta \boldsymbol{m} \backslash \boldsymbol{\rho A}$

Where Δm is the difference between the weight of the film and ρ the density of the film in units of (g/cm2) and A is the film area.
Different weights were measured for polytetrafluoroethylene and PMMA. Polytetrafluoroethylene is preheated first in a glass baker until fusion and then add to it a calculated amount of PMMA with different proportions (5, 7%. 10%) and the composite were heated with shaking to obtain a homogeneous solution. The solutions were thermally treated by placing them in an oven to gradually raise their temperature to 70 degrees, then gradually reduce its temperature to room temperature. The main purpose of heat treatment is to give the atoms the necessary kinetic energy to rearrange the crystal lattice, which leads to the regulation of the crystal structure of the material and thus reduce crystal defects in it. To study the electrical properties, an RLC circuit was used, and the measurements were made in a range of frequencies ranging from 1 to 1000 KHz.

4. Results and discussion

Figure 1 shows the relationship of the real part of the dielectric constant with frequency for pure and dopped models with different proportions of PMMA (5%, 7%, 10%) and for a range of frequencies ranging between 1-1000 KHz, at the room temperature. It is observed that the dielectric constant values of the dopped models increased significantly compared to the pure models for all concentrations, which indicates that the two polymers interaction gave support to the polytetrafluoroethylene infrastructure. Also noted that the dielectric constant values were high in the low frequency region up to 12 KHz where the dipoles find a sufficient time to rotate in the direction of the applied electric field. Then the values started to decrease with increasing frequency as these dipoles are no longer able to catch up with the electric field. After 175 KHz, the values of the dielectric constant were stabilized due to the restriction of the total polarization to the electronic polarization that does not change with frequency.

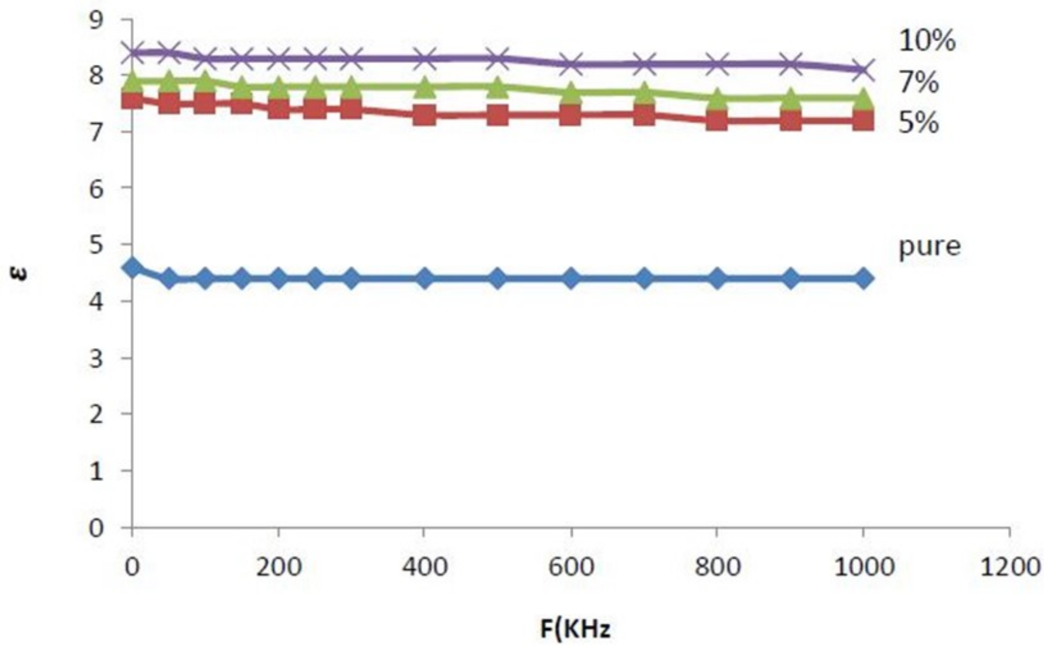

Figure 1 Relationship of the real part of the dielectric constant with frequency for pure and dopped models with different proportions of PMMA (5, 7%, 10%) and for a range of frequencies ranging from 1-1000 (KHz) and at the room temperature.

Figure 2 shows the change in the imaginary part of the dielectric constant with frequency. It shows that the mixing process led to an increase in the values compared to the pure model, and this is due the significant increase in the number of dipoles resulting from the addition process which in turn led to increase the amount of energy lost due to rotation or friction of the dipoles with each other. This increase, in turn, led to a corresponding rise in the values of tanδ and the AC conductivity of the models as shown in Figure 3,4.

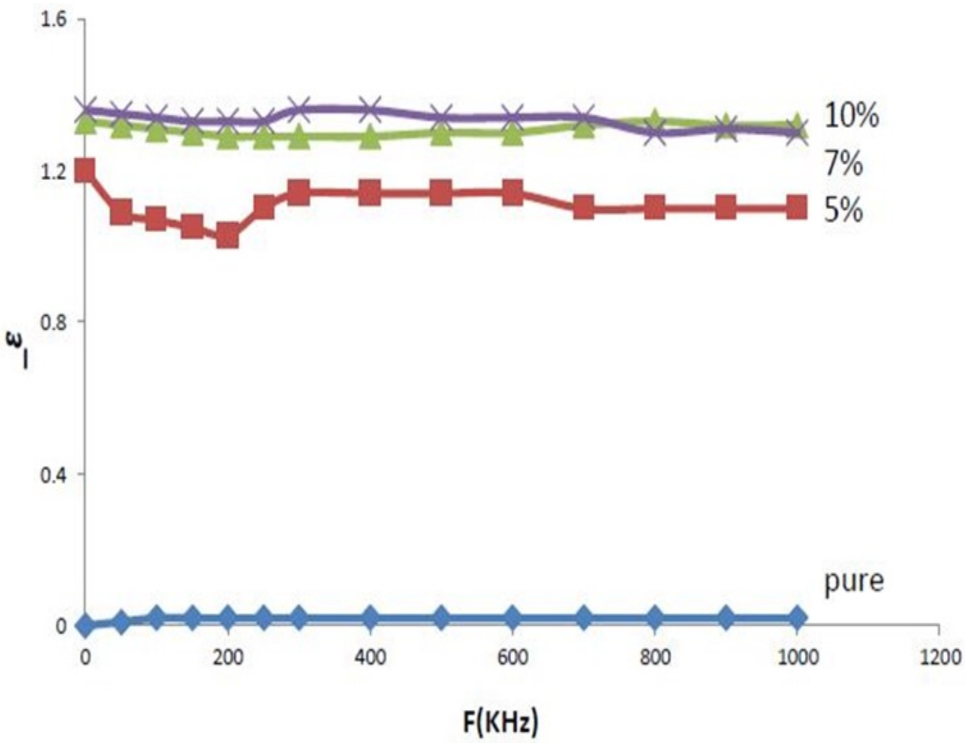

Figure 2 The relationship of the change in the imaginary part of the dielectric constant with frequency

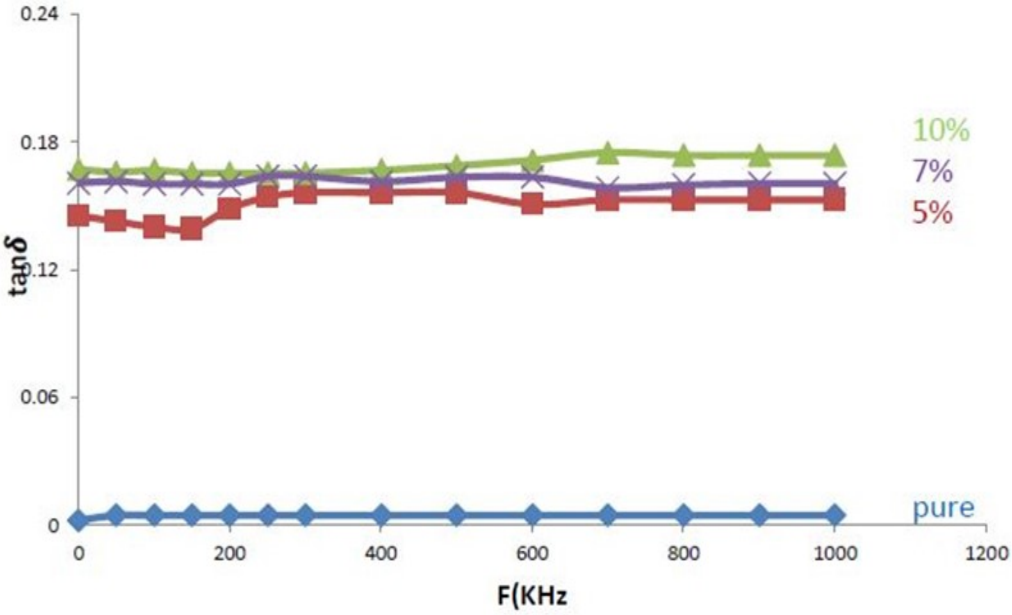

Figure 3 Relationship between tanδ and frequency of pure and dopped polymer with different volume rates of PMMA.

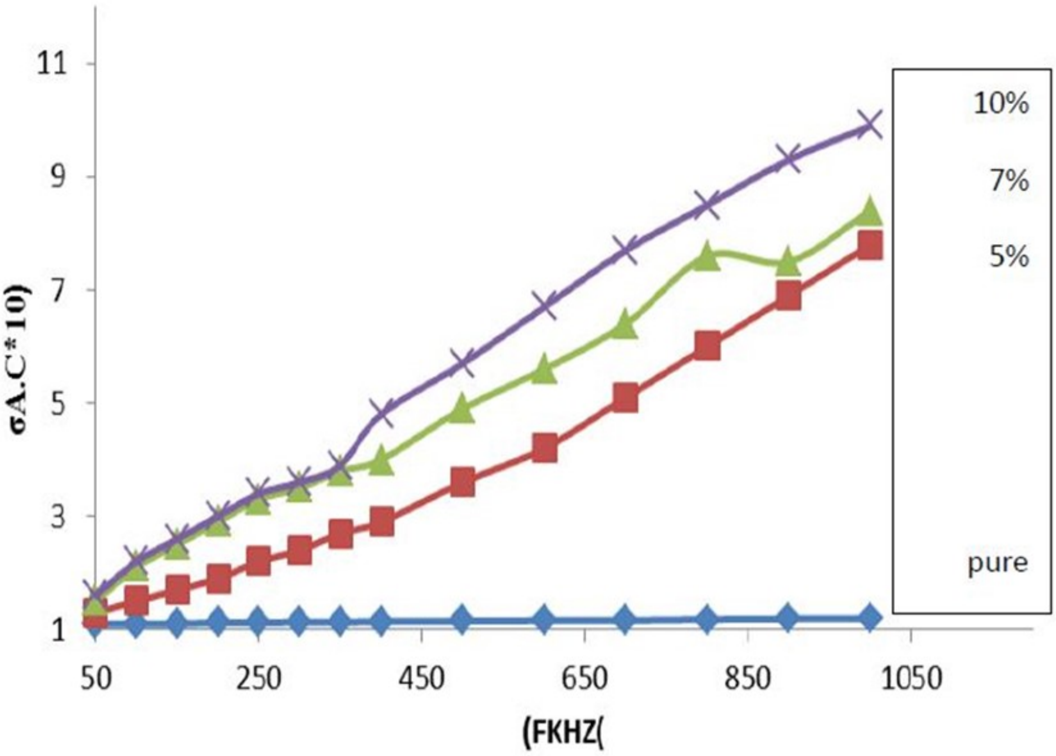

Figure 4 The relationship between the alternating conductivity and frequency of a pure and dopped polymer.

Figure 5 shows the relationship of the real part of the dielectric constant with the pure and the dopped model at the frequency of (500) KHZ, where it is noticed from that the doping process has a positive effect on the values of the dielectric constant and the highest values was at 15%, as it was around (9) (at the low frequency region). Taking into account that the value of the real part of the dielectric constant of the pure polymer is around 4.52, then the resulted value in fig.5 shows a big enhancement due to the process of mixing the pure polymer with PMMA. Enhancing the dielectric constant for the composite improves the refractive index and allows for using it with the emerging applications such as in optical ring resonators to control the resonance frequency by changing the cavity refractive index [8].

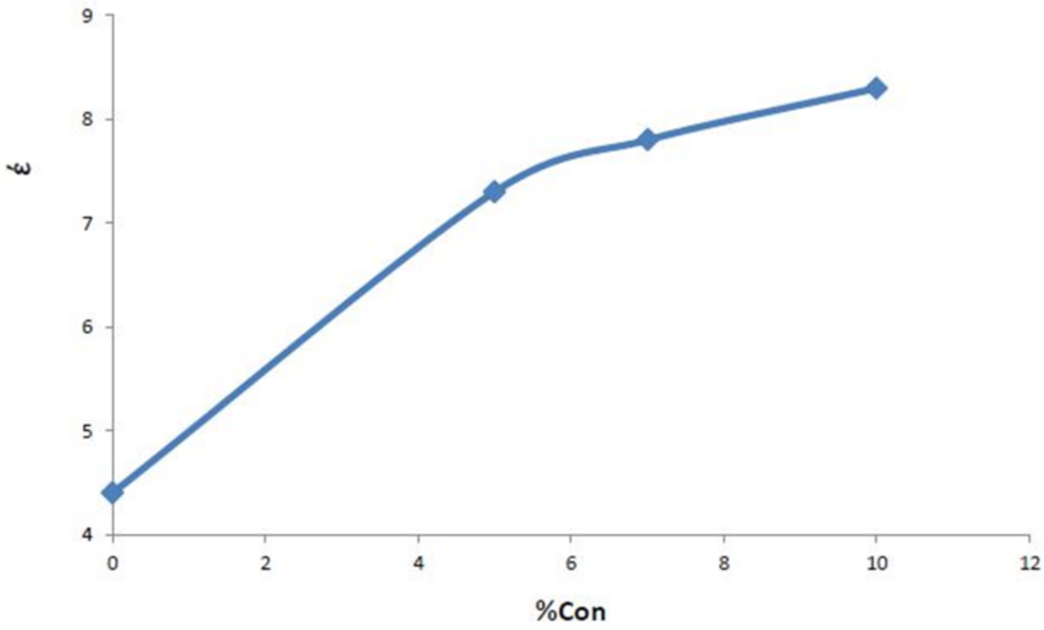

Figure 5 The relationship between the dielectric constant and different concentrations of pure polymer dopped with PMMA at different rates.

5. Conclusion

Polytetrafluoroethylene composites are synthesized and tested experimentally using different volume rates of PMMA to produce good insulators for electrical circuits applications. The thermochemical pyrolysis method, where the films are highly adherent to the base and have high stability in their physical properties with the time, is used in this work. Polytetrafluoroethylene and Poly (methyl methacrylate) are mixed at the room temperature with different volume rates and tested for different frequencies. The real and imaginary parts of the dielectric constants are calculated and presented for different frequencies and concentrations. The results show a high increase (more than 90%) of the dielectric constant of the composite compared to the pure model at 500 KHz which provide a good insulator for electrical and electronic circuits.

References

[1] Mansoor, Riyadh D., and Laith M. Rasheed. "A Study on The Conductivity of Polyaniline Polymers." IOP Conference Series: Materials Science and Engineering. Vol. 571. No. 1. IOP Publishing, 2019.

[2] Koleva, Milena, et al. "Strength characteristics of polymer composites with waste dust from power production." Proceedings of International Scientific Conference UNITEH. Vol. 7. 2007.

[3] Gledhill, Sophie, et al. "Doping induced structural and compositional changes in ZnO spray pyrolysed films and the effects on optical and electrical properties." Thin Solid Films 519.13 (2011): 4293-4298.

[4] Hargittai, Istvan. "Structures and mechanisms in chemical reactions: George A. Olah's life-long search of chemistry." (2017): 259-277.

[5] Wang, Moran, et al. "Three-dimensional effect on the effective thermal conductivity of porous media." Journal of Physics D: Applied Physics 40.1 (2006): 260.

[6] Linz Jr, Arthur. "Some electrical properties of strontium titanate." Physical Review 91.3 (1953): 753.

[7] Wu, C. W., and H. Conrad. "Negative electrorheological effect and electrical properties of a Teflon/silicone oil suspension." Journal of Rheology 41.2 (1997): 267-281.

[8] R. Mansoor and A. Duffy, "Optical racetrack resonators for strain sensing applications," Tenth International Conference on Computational Electromagnetics (CEM 2019), Edinburgh, UK, 2019, pp. 1-6, doi: 10.1049/cp.2019.0120.

IET Digital Library

Optical Racetrack Resonators for Strain Sensing Applications

Author(s): **R. Mansoor** [1] and **A. Duffy** [2]
View affiliations

Source: Tenth International Conference on Computational Electromagnetics (CEM 2019), 2019 page (6 pp.)
Conference: **Tenth International Conference on Computational Electromagnetics (CEM 2019)**

Access Full Text

Recommend Title Publication to library

- « Previous article
- Table of contents
- Next article »

Abstract

A strain gauge based on the design of a silicon photonic racetrack resonator is presented and simulated. In this photonic strain gauge, light is guided in a silicon waveguide coupled to a racetrack shaped waveguide through Evanescent mode coupling. The resonance sensitivity of this closed loop resonator to the change in length due to applied strain is calculated and modelled. The loop deformation results in resonance frequency shifts of the racetrack resonator. These shifts are measured numerically by calculating the through port power. The linear relationship between loop deformation, induced by the applied strain, and the resonance shifts allows for using this model for strain sensing applications. A grating-assisted racetrack sensor, where resonance splitting can be used to estimate the amount of the strain rather than the resonance shift itself, is discussed and proposed for future work. Silicon-on-insulator strain gauge technology can provide cheap and reliable sensors which are integrable in photonic circuits and immune from external electromagnetic interference.

DOI: 10.1049/cp.2019.0120
ISBN: 978-1-83953-066-1
Location: Edinburgh, UK
Conference date: 19-20 June 2019
Format: PDF

Inspec keywords: silicon-on-insulator; optical resonators; integrated optics; electromagnetic interference; strain gauges; silicon; microsensors; fibre optic sensors; optical waveguides; elemental semiconductors; strain sensors
Subjects: Mechanical variables measurement; Integrated optics; Optical waveguides; Optical waveguides and couplers; Fibre optic sensors; fibre gyros; Micromechanical and nanomechanical devices and systems; Integrated optics; Sensing and detecting devices; Sensing devices and transducers; Microsensors and nanosensors; Electromagnetic compatibility and interference; Fibre optic sensors

Related content

Fibre optic distributed strain sensing for open-holes specimen axial test

- L. Schenato ; E. Garbin ; L. Palmieri ; A. Pasuto ; C. Modena ; A. Galtarossa
- View description Hide description
- We have applied a commercial optical frequency domain reflectometer with high spatial resolution to measure the strain exerted on an aluminium specimen under tensile strength (open hole) test. The strain profile has been measured until failure by means of an optical fibre and by ten standard electric strain gauges. The matching between the measurement data provided by the two techniques at the strain gauges positions is excellent, except in the proximity of the hole, where the strain gradient is maximum. Due to that, a precise

correspondence between optical fibre and strain gauges position near the hole is mandatory in order to measure the same strain value. The resolution attainable by the optical system, that has not counterpart in any electrical systems, enables an unprecedented spatial sampling, thus allowing a much better characterization of the strain profile along the sample.

Design and verification of FBG strain gauge

- Zhinan Wang ; Shihai Hua ; Dajian Wang ; Wenjun Xu ; Sujun Yang
- View description Hide description
- Compared with the traditional electrical resistance strain gauge, the fibre Bragg grating (FBG) is a new material that can be used to produce the strain sensor, which has many advantages such as convenient installation, low temperature drifting, less signal interference and higher transmitted quality. In this study, FBG sensor system configuration, design principle, numerical simulation and loading tests for the FBG strain gauge are expatiated extensively. At the last, one-axial and three-axial strain gauges are produced and some conclusions have been put forward. So the FBG strain gauge can meet the precision of the structure monitoring and replace the traditional sensors.

Coupled π-shifted fibre Bragg grating ring resonant strain sensors

- C.E. Campanella
- View description Hide description
- Resonant optical strain sensors, obtained by closing in loop coupled π-shifted Bragg gratings (π-FBGs), are reported. Despite of a conventional π-FBG, showing a transmission Lorentzian resonance in the reflection band, the coupled π-shifted Bragg grating structure is characterised by a spectral response formed by a split doublet of the primary transmission Lorentzian mode of π-FBG. By closing in loop this structure, the coupled π-shifted Bragg grating ring resonators show better performance than π-shifted Bragg grating ring resonators in terms of strain sensitivity (i.e. 2.86 pm/με) is demonstrated. Thus, the coupled π-FBGRR is suitable for enhanced sensitivity strain sensing applications.

Silicon resonant strain gauges fabricated using SOI wafers

- S.P. Beeby ; G. Ensell ; N.M. White
- View description Hide description
- This paper details the design and fabrication process for a dynamically balanced silicon resonator. To optimise the degree of dynamic balance extensive finite element modelling (FEM) of the mechanical structure was carried out. A method of driving and detecting the optimum mode of the resonator was chosen in order to avoid compromising the mechanical design of the structure. The degree of dynamic balance has important implications for the use of the resonator in strain sensing applications. In the fabrication process silicon-on-insulator (SOI) wafers are used that enable the manufacture of the resonator in single-crystal silicon. This is an ideal mechanical material for such an application and is mechanically superior to polysilicon with wholly repeatable material properties. The fabrication process described in this paper has been designed to be relatively straightforward, thereby enabling the application of resonant strain gauges to a wide range of devices. (4 pages)

Mechanical Sensors and Actuators

-
- View description Hide description
- The class of mechanical sensors includes a fairly large number of different sensors based on many principles, but the four groups of general sensors discussed here - force sensors, accelerometers, pressure sensors, and gyroscopes - cover most of the principles involved in the sensing of mechanical quantities either directly or indirectly. Some of these sensors are used for applications that initially do not seem to relate to mechanical quantities. For example, it is possible to measure temperature through the expansion of gases in a volume. The expansion can be sensed through the use of a strain gauge, which is a classical mechanical sensor. In this application an indirect use of a strain sensor is made to measure temperature. On the other hand, some

mechanical sensors do not involve motion or force. An example of this is the optical fiber gyroscope, which will be discussed later in this chapter.

Study on the performance of temperature-stabilised flexible strain sensors based on silver nanowires

- Yi Du ; Qiang Zhang ; Kai Zhuo ; Jianlong Ji ; Zhongyun Yuan ; Chao Ji ; Wendong Zhang ; Shengbo Sang
- View description Hide description
- Nowadays, flexible strain sensors applied in the fields of health care and electronic skin have been widely studied and applied. In fact, the temperature characteristic of flexible strain sensors based on metal nanomaterials is rarely concerned. In this work, the ohmic and tensile properties of the flexible strain sensor based on silver nanowires–polydimethylsiloxane were tested and it was found that the sensor has good ohmic characteristics and a maximum gauge factor of 536.98. In addition, the resistance of the sensor was affected little by temperature when the temperature environment of the sensor was changed, and the resistance temperature coefficient of the flexible strain sensor is −1050 ppm/°C. Furthermore, it was found that the sensor was sensitive to minute strain when the sensors were applied to the two application tests of strain and pulse.

IOP Conference Series: Materials Science and Engineering

PAPER • OPEN ACCESS

A Study on The Conductivity of Polyaniline Polymers

To cite this article: Riyadh D. Mansoor and Laith M. Rasheed 2019 *IOP Conf. Ser.: Mater. Sci. Eng.* **571** 012087

IOP Conf. Series: Materials Science and Engineering **571** (2019) 012087 doi:10.1088/1757-899X/571/1/012087

A Study on The Conductivity of Polyaniline Polymers

Riyadh D. Mansoor [1*], Laith M. Rasheed[2]
[1] Engineering College, Al-Muthanna University, Samawa, Iraq.
[2] Al-Muthanna University, Samawa, Iraq.
[*] riyadhdmu@mu.edu.iq

Abstract. Polyaniline (PANI) is a promising conducting material to be used in a variety of electronic applications ranging from sensors, through solar cells to touch screens. Enhancing the electrical characteristics of polyaniline by increasing the charge carriers, using doping materials, allows for using it as a good alternative for semiconductors in the fabrication of integrated circuits. Zinc sulfide (Zns) is considered one of the attractive doping materials that improve the electrical characteristics of polyaniline owing to the distinctive optical characteristics in the visible range. In this work, a practical study on the electrical properties of polyaniline doped with zinc sulfide is presented and compared with pure PANI. Different volume rates of doping are tested, experimentally, and the results are collected. Voltage-current characteristics and the activation energy levels are obtained for different temperatures. From the results, it has been observed that the conductivity increases by increasing the doping rate and inversely related to temperature. A low activation energy level and improved I-V characteristics are shown to be approachable by careful choice of doping rate. Polyaniline doped with zinc sulfide provides low cost conductors for integrated circuits industry.

1. Introduction

Polymers are the main stone of many modern sciences and the source of modern technological development, especially in the field of digital electronics such as diodes, light emitting diodes [1], field effect transistors and energy storage devices like rechargeable batteries [2], display screens, solar cells, and gas sensors [3]. The extensive use of polymers in the field of electronic devices has given it a special importance since they generally show different changes in their electrical behavior when doped or mixed. However, there are still some engineering problems such as the lack of hardness (stiffens and strength) compared to some metals. Therefore, several methods were used to improve the properties of polymers, including fiber reinforcement, etc. [4]. Polymers are preferable due to some of the characteristics that are distinguished from other semiconductors such as light weight and ease to perform. It can be produced as a powder, thin film, or fiber. Moreover, it can easily remove the doping by compensation method, which is performed by immersing these thin films in a strong base liquid such as ammonia fluid or ammonium hydroxide [5].

The study of thin film has been of interest to scientists since about a century and a half. A thin film has different uses and applications. The term thin film is used to describe a layer or several layers of material atoms that are in a micrometer or several nanometers range. It is thin and fragile and should be deposited on a solid material such as glass and aluminum.

There are different methods to enhance the conductivity of polymers, for example: band theory, space charge limited current effect, Schottky emission, Paul Frankl effect, tunnel effect and doping effect [6]. The conduction ability increases for some of the semiconductor polymers by increasing the doping and among these polymers is the polyaniline, which is under investigation in this paper. The electrical characteristics of polyaniline doped with different concentration rates of zinc sulfide, in different temperatures, are studied and compared with that of pure polyaniline.

2. Materials used

2.1. Polyaniline

Polyaniline is a conducting polymer also called vinylamine and chemically expressed as (C6H5NH2) [7]. The chemical properties of polyaniline are listed in table 1 [8].

Table 1. Chemical properties of Polyaniline.

Chemical formula	**C6H5NH2**
Specific density	1.02 g/cm^3
Molecular weight	93.13 h/Mol
PH value	8.8
The condition in which the polymer is available	Liquid
Color	Light blue
Boiling temperature	184 ^{0}C

2.2. Zinc Sulfide

One of the sulfide compound materials, it is similar to the lead's structure and has a chemical formula of (Zns). It is transparent of semi-transparent with a yellow color. Also, it is bivalent, and usually used in electronic devices since it shows high sensitivity towards electromagnetic radiations and when it doped with some chemical elements it lights up.
Zinc sulfide can be considered is of a high interest for light emitting diodes, laser and LCDs since it is of excellent lighting over wide range of wavelengths. Table 2 summaries the chemical properties of Zns.

Table 2 Chemical properties of Zns.

Chemical formula	**Zns**
The mass of the mole	97475 g/Mol
Shape	Yellow crystalline powder
Density	4.0090 g/cm^2
Melting point	1185 C
Melting in water	None

2.3. Doping

The best way to control the conductivity of semiconductors is to add small amounts of impurities to the semiconductor crystal, this process is called doping. Doping also gives us an idea about the possibility of controlling the density of free electrons or the density of holes. Therefore, semiconductors are classified into two types that are negative of n-type semiconductors and positive of p-type semiconductors.
Doping process means adding materials inside the pure polymer where the impurities propagate is inside the polymer chains. A physical and chemical interaction might happen depending on the nature

of impurities and polymer. One of the important methods of doping is the chemical method, which depends on the oxidation and reduction [9]. Also, the electrochemical method, where the doping process happens in a small cell of two electrodes immersed in an electrolyte solution [10]. The amount of doping material needed to be controlled by high doping leads to restricting the mobility of charge carriers, which in turns leads to a reduction of the electrical conductivity.

3. Experimental setup

Based on the experimental published results, the density of charge carriers affects the electrical conductivity [4]. However, the main factor that increases the conductivity is the mobility of charge carriers. The conductivity changes with temperature, time and electric field applied. The electric conductivity can be expressed as [11]:

$$\sigma = d/RA \qquad 1$$

Where R is the resistivity, d is the thickness and A is the area of the electrodes.

Also, it is possible to calculate the activation energy by using Arrhenius Equation:

$$\sigma = \sigma o \exp(-Ea/KBT) \qquad 2$$

Where, Ea is the activation energy, KB is the universal gas constant, T the temperature (Kelvin) and σo is the conductivity at absolute zero temperature.

The experiment steps were as follows:

1. Aluminum bases of dimensions (20 x 15 x 1 mm3) are prepared first by cleaning them with water for 15 minutes to get rid of impurities then immersed in ethanol solution.
2. They were dried using cloth and washed again with distilled water more than once before placing in a container.
3. Two milligrams of polyaniline were melted in 10 moles of DMF solution, and then a 0.5 mg of zinc sulfide also melted and left for two hours.
4. A magnetic mixer was used to obtain homogeneous composite.
5. The solution was filtered to get rid of impurities. These two materials were mixed with different rates as (1, 2, and 3%). Table 3 below shows the doped poly aniline polymer with different weighing rates of zinc sulfide.

Table 3. The doped poly aniline polymer with different weighing rate of zinc sulfide.

Polyaniline volume	Zinc sulfide volume	Weighing rate
10	0	0
9	1	10%
8	2	20%
7	3	30%

6. In order to prepare thin films, chemical analysis method was used. This method depends mainly on spraying the solution of the material required to prepare thin film on a hot bases at a specific temperature; this temperature depends on the type of material used. Based on the thermal/chemical interaction between material atoms and hot bases the film will exist.

IOP Conf. Series: Materials Science and Engineering **571** (2019) 012087 doi:10.1088/1757-899X/571/1/012087

7. Thermal processing using 40 C oven for 30 minutes was performed to obtain solid and non-fragile thin film.
8. The weighting method was used to measure the thickness of thin film using sensitive, balanced scale type (Mettler AE160) with four digits.

   Thin film thickness (t) was calculated based on the following equation.

   $$t = (M1-M2)/A.\rho \qquad 3$$

   Where A is the film area, M1 and M2 are the base weight before and after weighting, respectively, and ρ is the material density. The film thickness was ranging between 0.15 to 0.3 µm.
9. Deposition of Aluminium electrodes on the outer surface was done using an evaporation device under a pressure of 10-5 Torr. A circle shape electrodes of 0.03 cm2 area, and 1 cm separation distance were used.

Finally, the electrical measurements were performed on an electrical circuit using voltmeter, and current meter under different temperatures ranging 293 - 343 K.

4. Results and discussions

Figure 1 shows the difference between the conductivity of pure polyaniline and that of zinc sulfide doped polyaniline for different doping rates and temperatures. It can be seen that the doped polyaniline shows an ohmic behaviour at low temperature (293 -310 K). However, above 310 K, the relation between voltage and current obey different law depends on the space charge limited current (SCLC). The possibilities of the occurrence of this type of conductivity in materials that contain aromatic rings are relatively high due to the presence of traps as well as terminals. Also, it may result from the difference in the length of polymer chains at the surface from that inside the volume or due to surface defects as well as the interaction between the crystalline and non- crystalline regions. Figure 1 shows also that the conductivity increases with the increase of temperature, which means that the material has a negative temperature coefficient. Therefore, the ohmic resistance reduced by increasing the temperature due to the fact that the polymer chain and zinc sulfide ions are acting as traps and barriers against the moving charges through the process of jumping that increase with increasing the temperature. Increasing the temperature results in high movement of polymer's chains, therefore, more charge carriers released to the composite material

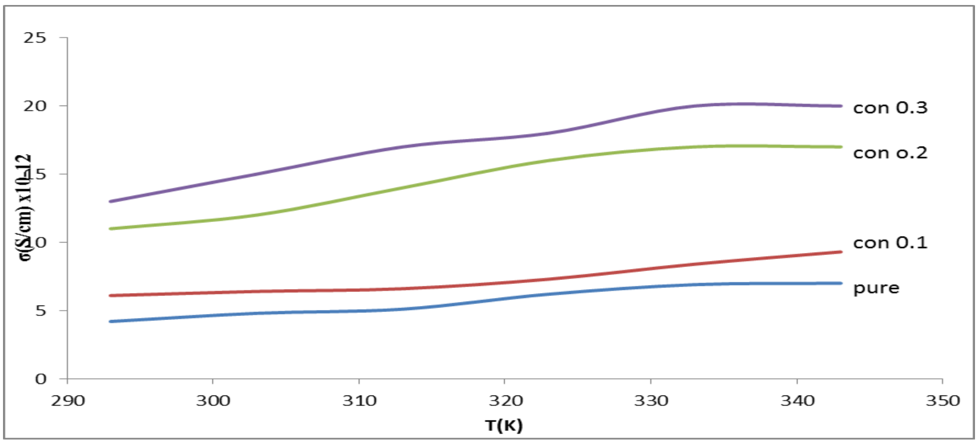

Figure 1 the difference between the conductivity of pure polyaniline and that of zinc sulfide doped polyaniline for different doping rates and temperatures.

IOP Conf. Series: Materials Science and Engineering **571** (2019) 012087 doi:10.1088/1757-899X/571/1/012087

Figure 2 shows the relation between the conductivity and the concentration ratio of the doped polyaniline at 313 K. It can be seen that the conductivity remains, almost, constant at low concentration ratio. Then it doubled by increasing the ratio compared with the pure polyaniline. This behaviour might result due to the dominant of the electrical characteristics at high concentrations compared to low concentrations of doped material, and therefore the conductivity increases by increasing the charge carriers.

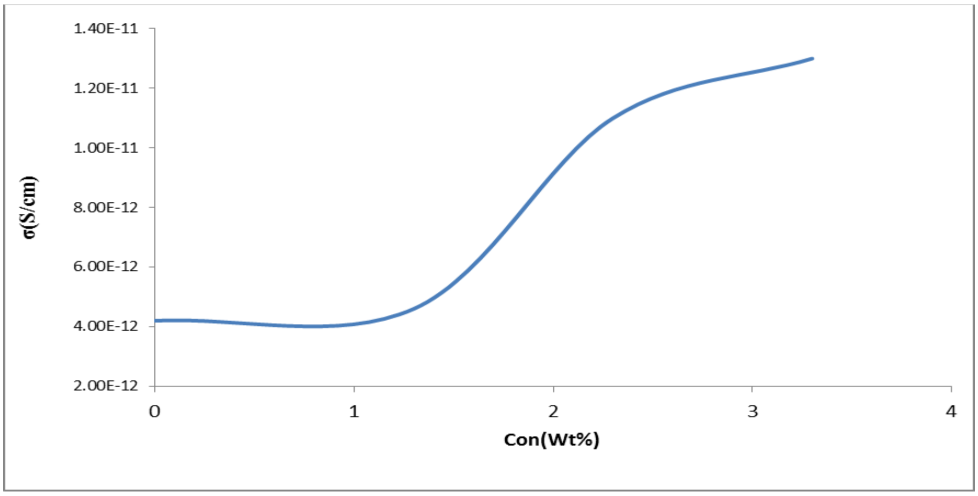

Figure 2 the relation between the conductivity and the concentration ratio of the doped polyaniline at 313 K.

Figure 3 shows the relation between the conductivity and the reciprocal of temperature. It shows that a high level of activation energy due to the presence of free ions resulting from the doping ratio. Also, it is found that at high concentration ratio, the activation energy reduces due to the effect of space charge. In addition, these concentrations lead to the creation of new energy levels in the forbidden region that acts as traps for the energy carriers and results in a reduction in the activation energy of the composite material, as in figure 4.

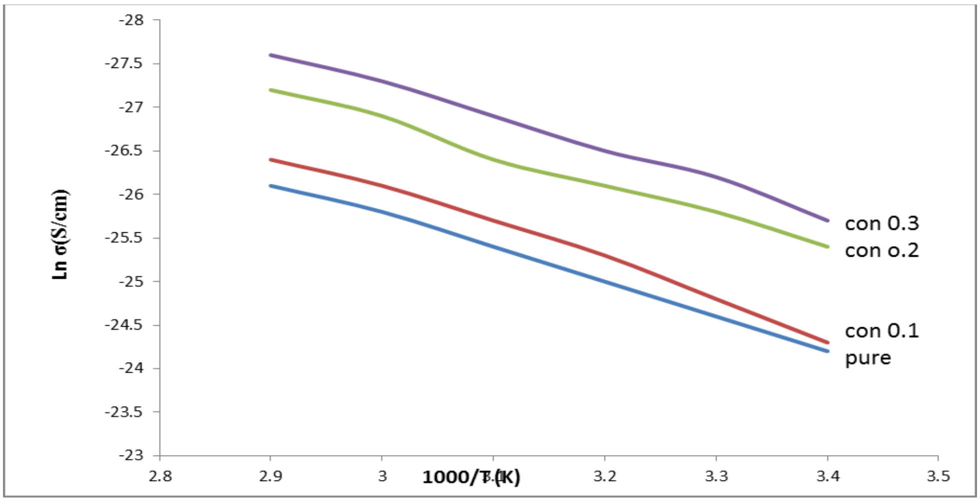

Figure 3 the relation between the conductivity and the reciprocal of temperature.

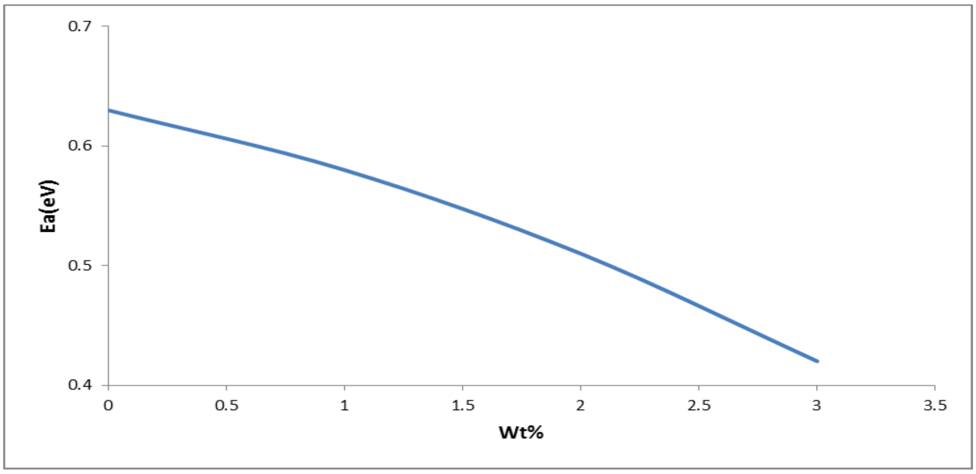

Figure 4 the relation between activation energy level and the concentration of doping material.

5. Conclusion

The conductivity of a composite material formed by a polyaniline doped with zinc sulfide is studied experimentally. The results were compared with that of a pure polyaniline. An electrical circuit was built, and the IV characteristics were measured for different doping concentration ratios and at for a wide range of temperature. The activation energy level, also, was measured and presented. The results show that the conductivity is increased by increasing the temperature, which gives a semiconductor like behavior of the composite under investigation. Also, increasing doping ratio improves the conductivity. The activation energy was shown to be reduced by increasing doping ratio, which helps in enhancing the electrical characteristics of the electronic devices made by these composites

References

[1] L. T. Tuyen, K. Potje-Kamloth and H. Liess, "Electrical properties of doped polypyrrole/silicon heterojunction diodes and their response to NOx gas," Thin solid films, vol 292, no 1-2, pp. 293-298, 1997.
[2] Y. Yang, E. Westerweele, C. Zhang, P. Smith and A. J. Heeger, "Enhanced performance of polymer light-emitting diodes using high-surface area polyaniline network electrodes," Journal of applied physics, vol 77, no 2, pp. 694-698, 1995.
[3] C.J. Brabec and S.N. Sariciftci, "Electroactive Materials," in Recent developments in conjugated polymer based plastic solar cells, Anonymous Springer, 2001, pp. 1- 1-11.
[4] Y. P. Mamunya, V. V. Davydenko, P. Pissis and E. V. Lebedev, "Electrical and thermal conductivity of polymers filled with metal powders," European polymer journal, vol 38, no 9, pp. 1887-1897, 2002.
[5] A. Z. Sadek, W. Wlodarski, K. Kalantar-Zadeh, C. Baker and R. B. Kaner, "Doped and dedoped polyaniline nanofiber based conductometric hydrogen gas sensors," Sensors and actuators A: Physical, vol 139, no 1-2, pp. 53-57, 2007.
[6] A. Abdel-All, A. Elshafie and M. M. Elhawary, "DC electric-field effect in bulk and thin-film Ge5As38Te57 chalcogenide glass," Vacuum, vol 59, no 4, pp. 845-853, 2000.
[7] T.A. Skotheim, Handbook of conducting polymers, CRC press, 1997.
[8] C. R. Schmid, J. D. Bryant, M. Dowlatzedah, J. L. Phillips, D. E. Prather, R. D. Schantz, N. L. Sear and C. S. Vianco, "Synthesis of 2, 3-O-isopropylidene-D-glyceraldehyde in high chemical and optical purity: Observations on the development of a practical bulk process," The journal of organic chemistry, vol 56, no 12, pp. 4056-4058, 1991.
[9] R. Murugesan and E. Subramanian, "Effect of organic dopants on electrodeposition and characteristics of polyaniline under the varying influence of H2SO4 and HClO4 electrolyte media," Materials chemistry and physics, vol 80, no 3, pp. 731-739, 2003.
[10] S. R. Moraes, D. Huerta-Vilca and A. J. Motheo, "Characteristics of polyaniline synthesized in phosphate buffer solution," European polymer journal, vol 40, no 9, pp. 2033-2041, 2004.
[11] H. Klauk, Organic electronics: Materials, manufacturing, and applications, John Wiley & Sons, 2006.

Accepted Manuscript

Numerical Modelling of Surface Plasmonic Polaritons

Riyadh Mansoor, Amin Habbeb AL-Khursan

PII: S2211-3797(18)30642-9
DOI: https://doi.org/10.1016/j.rinp.2018.04.052
Reference: RINP 1423

To appear in: *Results in Physics*

Received Date: 17 March 2018
Revised Date: 8 April 2018
Accepted Date: 19 April 2018

Please cite this article as: Mansoor, R., AL-Khursan, A.H., Numerical Modelling of Surface Plasmonic Polaritons, *Results in Physics* (2018), doi: https://doi.org/10.1016/j.rinp.2018.04.052

Numerical Modelling of Surface Plasmonic Polaritons

Riyadh Mansoor[(1),*] and Amin Habbeb AL-Khursan[(2),**]

[(1)]Engineering College, Al Muthanna University, Samawa, Al Muthanna, Iraq
[(2)]Nassiriya Nanotechnology Research Laboratory (NNRL), Science College, Thi-Qar University, Nassiriyah, Iraq.

[*]riyadhdmu@mu.edu.iq,
**Corresponding author: ameen_2all@yahoo.com.

Abstract

Extending optoelectronics into the nano-regime seems problematic due to the relatively long wavelengths of light. The conversion of light into plasmons is a possible way to overcome this problem. Plasmon's wavelengths are much shorter than that of light which enables the propagation of signals in small size components. In this paper, a 3D simulation of surface plasmon polariton (SPP) excitation is performed. The Finite integration technique was used to solve Maxwell's equations in the dielectric-metal interface. The results show how the surface plasmon polariton was generated at the grating assisted dielectric-metal interface. SPP is a good candidate for signal confinement in small size optoelectronics which allow high density optical integrated circuits in all optical networks.

Keywords: All-optical networks. Optical integrated circuits. Optoelectronics. Plasmons. Surface plasmon polariton.

1. Introduction

All-optical networks are a solution to the increased bandwidth requirements of data communication, allowing architectures to become increasingly integrated [1]. High integration density requires small size components that allow for high signal confinements especially at the bending regions. Light's wavelengths allow for optical waveguide cross-sections in the range of micrometers [2]. A possible way to extend optoelectronics into the nanometer regime is to convert the photon into plasmons which are existing at frequencies higher than that of light [3].

Plasmons are density waves in an electron gas in a similar manner of sound waves and exist mainly in metals with weakly bounded electrons [4]. Plasmons are collective waves where billions of electrons oscillate in sync. The electron gas has a resonance right at the plasma frequency w_p. This resonance frequency increases with the electron density n, since the electric restoring force is proportional to the displaced charge (analogous to the force constant f of a spring): $w_p \alpha \sqrt{n}$ [5].

An electric field cannot exist inside a metal, because metal electrons follow the field until they have compensated it. Above the plasma frequency, however, the external field oscillates too fast for the electrons to follow. A metal loses its reflectivity. The corresponding photon energy is the plasmon energy $E_p = w_p$, typically 10-30 eV (deep into the ultraviolet) [6]. To combine optoelectronics with plasmonic, one must convert light (photons) into plasmons. However, there are two types of plasmons, which are bulk plasmons with a longitudinal oscillation (parallel to the propagation direction) and surface plasmons with transverse oscillation. Photons are transverse, which means it is impossible to transfer the photon energy to the bulk plasmons due to oscillation mismatch. Only surface plasmons can be excited in the dielectric- metal interface and photon energy can be transferred to electrons using number of techniques to overcome wavenumber (k) mismatch.

Even though both photons and surface plasmons are transverse, however, they have different momentum [7]. Plasmon has energy E and momentum p as a quantum numbers. Photons and plasmons have their dispersion plots which are required to coincide to ensure the transfer of photon energy to surface plasmons. Different method to couple photons and surface plasmons were proposed. Prism coupling, near field coupling, waveguide mode coupling, and grating coupling are all used to excite surface plasmon polariton SPP.

Surface plasmon polaritons (SPPs) are propagating excitations that result from the light energy coupling with collective oscillations of the electrons at the dielectric-metal interface [8]. SPPs are highly localized and provide a good alternative for the photon as a promising carrier to make optical circuits more integrated. All optical networks with high density integrated circuits are more approachable by exploiting SPPs [9]. In this paper, the basic principles of surface plasmon are introduced and discussed, then followed by the observation of SPPs in 3D-simulation environments provided by the CST simulation software [10].

This paper is organized as follows, Mathematical representation of quantum numbers is presented in section 2. Section 3 is devoted to describing the dispersion relation of SPPs. The results of simulations are presented in section 4. Finally, the discussion is presented in section 5.

2. Surface Plasmon Polariton

Surface plasmons polaritons SPPs are a collective electrons density waves results from photon-electron energy exchange and localized at the surface of a metal. Fig. 1 shows the nature of the surface charge oscillation and the resulting fields associated with it. The coupling between light and the surface plasmon was proposed first by [12].

The Maxwell equations for the dielectric-metal interface can be used to derive the dispersion of SPPs. Starting with the dielectric-metal interface shown in Fig. 2, the *z*- and *x*- components of the electric field E can be written as E_z and E_x, respectively. The *y*- component E_y is zero. Also, the *x*- and *z*- components of the magnetic field H, i.e. H_x, H_z, respectively, are zero, i.e.;

$$E_y = 0,\ H_x = H_z = 0$$

Then, the electric and magnetic fields in the dielectric E_d, H_d, respectively, can be written as,

$$E_d = (E_{xd} = E_{zd})e^{j(k_{xd}x + k_{zd}z - wt)} \qquad (1)$$

$$H_d = H_{yd}e^{j(k_{xd}x + k_{zd}z - wt)} \qquad (2)$$

At metal,

$$E_m = (E_{xm} = E_{zm}) = e^{j(k_{xm}x + k_{zm}z - wt)} \qquad (3)$$

$$H_m = H_{ym}e^{j(k_{xd}x + k_{zd}z - wt)} \qquad (4)$$

where $E_{xd(m)}, E_{zd(m)}$ are the *x*-and *z*- components of the electric field in dielectric, *d* (metal, *m*) while $H_{yd(m)}$ is the *y*- component of the magnetic field in dielectric (metal). k_{xd}, k_{zd} are the *x*-and *z*-wave vector components in the dielectric (metal). *w* is the frequency.

By applying the boundary conditions,

$$D_m = D_d$$

$$\varepsilon_m E_{zm} = \varepsilon_d E_{zd}$$

$$E_{xd} = E_{xm}$$

$$H_{ym} = H_{yd}$$

$$\nabla \times B = \frac{1}{c^2}\frac{\partial E}{\partial t}$$

$$\mu[\nabla \times H] = \frac{1}{c^2}\frac{\partial E}{\partial t}$$

$$\nabla \times H = \frac{c}{\varepsilon}\frac{\partial E}{\partial t}$$

Where $D_{d(m)}$ is the dielectric displacement field in dielectric (metal). $\varepsilon_{d(m)}$ is the dielectric constant or relative permittivity in dielectric (metal). B is the magnetic induction field, ε, μ are the dielectric constant of the medium and magnetic permeability of the medium, respectively.

By applying curl function

$$\begin{vmatrix} x & y & z \\ \frac{\partial}{\partial x} & \frac{\partial}{\partial y} & \frac{\partial}{\partial z} \\ 0 & H_y & 0 \end{vmatrix} = \frac{\varepsilon}{c}\frac{\partial E}{\partial t}$$

This results in,

$$\frac{\partial H_y}{\partial z} = -\frac{\varepsilon}{c}\frac{\partial E_x}{\partial t}$$
$$\frac{\partial H_y}{\partial x} = \frac{\varepsilon}{c}\frac{\partial E_z}{\partial t}$$

x- component in metal

$$\frac{\partial H_{ym}}{\partial z} = -\varepsilon_m \frac{w}{c} E_{xm}$$
$$\frac{\partial H_{ym}}{\partial z} \rightarrow k_{zm} H_{ym} = -\varepsilon_m \frac{w}{c} E_{xm}$$

x-component in dielectric

$$-\frac{\partial H_{yd}}{\partial z} = -k_{zd} H_{yd}$$
$$k_{zd} H_{yd} = \varepsilon_d \frac{w}{c} E_{xd}$$

Z- component in metal

$$k_{xm} H_{ym} = -\varepsilon_m \frac{w}{c} E_{zm}$$

z- component in dielectric

$$k_{xd} H_{yd} = -\varepsilon_d \frac{w}{c} E_{zd}$$

By dividing x components in metal and dielectric

$$\frac{k_{zm}H_{ym}}{k_{zd}H_{yd}} = -\frac{\varepsilon_m E_{xm}}{\varepsilon_d E_{xd}} \qquad (5)$$

Again, by applying the boundary conditions

$$\frac{k_{zm}}{k_{zd}} = -\frac{\varepsilon_m}{\varepsilon_d}$$

$$\frac{k_{zd}}{\varepsilon_d} + \frac{k_{zm}}{\varepsilon_m} = 0$$

Notice that

$$k_x^2 + k_z^2 = \varepsilon \frac{w^2}{c^2}$$

At the interface

$$k_{xd} = k_{xm}$$

Dielectric

$$k_x^2 + k_{zd}^2 = \varepsilon_d \frac{w^2}{c^2} \qquad (6)$$

Metal

$$k_x^2 + k_{zm}^2 = \varepsilon_m \frac{w^2}{c^2} \qquad (7)$$

Solving these equations

$$k_x^2 = \frac{w^2}{c^2}\frac{\varepsilon_m \varepsilon_d}{\varepsilon_m + \varepsilon_d} \qquad (8)$$

To plot the dispersion relation, we can use the following equation

$$w = \sqrt{\frac{\varepsilon_m + \varepsilon_d}{\varepsilon_m \varepsilon_d}}\, ck_x \qquad (9)$$

3. Dispersion Relation of SPP

To derive the dispersion relation of SPPs, it is needed to start from Drude model of dielectric constant [13].

Based on Drude model, charges in a metal are treated as harmonic oscillation,

$$ma = F_{Elocal} + F_{Damping} + F_{spinning} \qquad (10)$$

Where, m is the mass of electron and a is the acceleration. The right hand side of Eq. 10 writes the force F on the electron under electric field E as contribution of the local force under E, F_{Elocal}, the damping force $F_{Damping}$, which is characterized by the damping rate $\gamma(=1/\tau)$, with τ is the relaxation time of the free electron gas, and spinning force $F_{spinning}$ characterized by the constant C. This last part represents the contribution of interband transitions.

$$m\frac{d^2r}{dt^2} + m\gamma\frac{dr}{dt} + Cr = -eE_L \exp(-jwt) \qquad (11)$$

C=0 for electrons not bound to a molecule. E_L is the amplitude of the local electric field. For the effective dielectric constant of metal,

$$\varepsilon_{eff} = \varepsilon_B - \frac{w_p^2}{w^2} + i\frac{w_p^2}{w^3\tau} \qquad (12)$$

ϵ_B for bound electron, and the rest of the right hand in Eq. 12 is for free electrons. w_p is the plasma frequency of the free electron gas.

Only conduction electrons contribute to ϵ_{eff} which means that $\epsilon_B \approx 1$

$$\varepsilon_{eff} = 1 - \frac{w_p^2}{w^2} + i\frac{w_p^2}{w^3\tau}$$

Therefore, the real part of dielectric constant is

$$\varepsilon_r = 1 - \frac{w_p^2}{w^2} \qquad (13)$$

Based on Eq. 13, it is shown that for frequencies below the plasmon frequency, $w < w_p$, the values of ϵ is negative, equal to 0 at $w = w_p$ and goes positive over the plasmon frequency $w > w_p$. Combining Eqs. (8) and (13) gives the relation of the surface plasmon wave vector k_{sp} ,

$$k_x = k_{sp} = \frac{w}{c}\sqrt{\frac{(w^2 - w_p^2)\varepsilon_d}{w^2(1+\varepsilon_d) - w_p^2}} \qquad (14)$$

Equation 14 can be plotted as in *Figure 2*. By comparing this equation with the dispersion equation of photon given by $w = ck_x$. It is found that the dispersion line of surface plasmon and that of light will never intersect at any value of k_x as shown in figure 2

In order to excite the SPPs, these two plots need to cut each other at a specific value of k_x and this was done by different methods. One of these methods is to use surface grating that will result in a change in the wavenumber and leads to the excitation of SPP.

Next section will show how the gratings enhance the excitation of SPPs compared to a smooth surface metal-dielectric

4. Simulation of SPPs

A metal-insulator-metal model is investigated in this section. The optical coupling to propagate SPPs was simulated using CST microwave studio by performing the finite integration technique (FIT). The model consists of a layer of gold with a thickness of 10 nm placed on a layer of aluminum (Al_2O_3) with a refractive index of 1.73^2 on top of silver layer of 5 nm to form a metal-dielectric-metal model. A layer of gold substrate is used. The schematic of the simulated model is shown in *Figure 3*. The frequency range was set between 400 THz to 416 THz, with a normal background. The dimensions of the gold layer are 130 nm in x direction, 10 nm in y direction and 200 nm in z direction. The boundary conditions were set to unit cell in x and y direction to simulate an infinite long in both directions. For z direction, an open add space boundary condition was applied for Zmax, while E=0 was applied for Zmin.

The field monitor at f=416 THz was introduced by defining e-field monitor. A frequency domain solver was used to perform the simulation and the result was as shown in *Figure 4*. It is shown that the signal concentrated on the top of the gold layer and no penetration occurs, which means no surface plasmon was occurred.

In *Figure 5*, a surface roughness was introduced at the surface of the model to obtain grating surface. After applying the field and performing the frequency simulation, the result is shown in *Figure 6*. This figure shows the confinement of power at the metal-dielectric interface and a generation of SPP.

A comparison of *Figure 4* and *Figure 6* shows how the surface grating helps on the excitation of SPP compared to the smooth surface model.

5. Conclusion

Plasmon is a hot topic since it provides signal confinement in a very small size component allowing a high-density integration in all optical integrated circuits. Different applications can be recognized based on surface plasmons ranging from biosensors to groove waveguides. In this paper, a mathematical model of surface plasmons is presented by solving Maxwell's equations at the dielectric-metal interface. Drude's model also was used to derive the refractive index of the metal. The dispersion of the SPPs and that of the light was shown not to intersect unless an external mechanism is used. Surface grating, is one of that mechanism that is modelled numerically in this work to show how the SPPs can be excited compared to that of a smooth surface interface.

ACCEPTED MANUSCRIPT

6. References

[1] R. Mansoor, S. Koziel, H. Sasse, and A. Duffy, "Crosstalk Suppression Bandwidth Optimisation of a Vertically Coupled Ring Resonator Add/Drop Filter", *IET Optoelectronics* 9, 30-36 (2015).

[2] Poon, A. W., Xianshu Luo, Fang Xu, and Hui Chen. 2009. "Cascaded Microresonator-Based Matrix Switch for Silicon on-Chip Optical Interconnection." *Proceedings of the IEEE* 97 (7): 1216-1238.

[3] W. L. Barnes, A. Dereux, and T. W. Ebbesen,. "Surface Plasmon Subwavelength Optics." *Nature* 424, 824-830 (2003).

[4] A. R. Melnyk, and M. J. Harrison, "Theory of Optical Excitation of Plasmons in Metals", *Physical Review B* 2, 835 (1970).

[5] H. A. Atwater, "The Promise of Plasmonics", *Scientific American* 296, 56-62 (2007).

[6] S. Linic, P. Christopher, and D. B. Ingram, "Plasmonic-Metal Nanostructures for Efficient Conversion of Solar to Chemical Energy." *Nature Materials* 10, 911-921 (2011).

[7] J. A. Dionne, L. A. Sweatlock, H. A. Atwater, and A. Polman, "Plasmon Slot Waveguides: Towards Chip-Scale Propagation with Subwavelength-Scale Localization", *Physical Review B* 73, 035407 (2006).

[8] P. Cheyssac, V. A. Sterligov, S. I. Lysenko, and R. Kofman. "Surface Plasmon-Polaritons", *Physica Status Solidi(a)* 175, 253-258 (1999).

[9] A. V. Zayats, and I. I. Smolyaninov. 2003. "Near-Field Photonics: Surface Plasmon Polaritons and Localized Surface Plasmons." *Journal of Optics A: Pure and Applied Optics* 5 (4): S16.

[10] CST. "3D Electromagnetic Simulation Software", last modified 2013, www.cst.com.

[11] J. Zhang, L. Zhang and W. Xu, "Surface plasmon polaritons: physics and applications", J. Phys. D: Appl. Phys. 45 (2012) 113001.

[12] J. M. Pitarke, V. M. Silkin, E. V. Chulkov, and P. M. Echenique, "Theory of Surface Plasmons and Surface-Plasmon Polaritons", *Reports on Progress in Physics* 70, 1 (2006).

[13] K. H. Lee, I. Ahmed, R. S. M. Goh, E. H. Khoo, E. P. Li, and T. G. G. Hung, "Implementation of the FDTD Method Based on Lorentz-Drude Dispersive Model on GPU for Plasmonics Applications", *Progress in Electromagnetics Research* 116, 441-456 (2011).

Figures

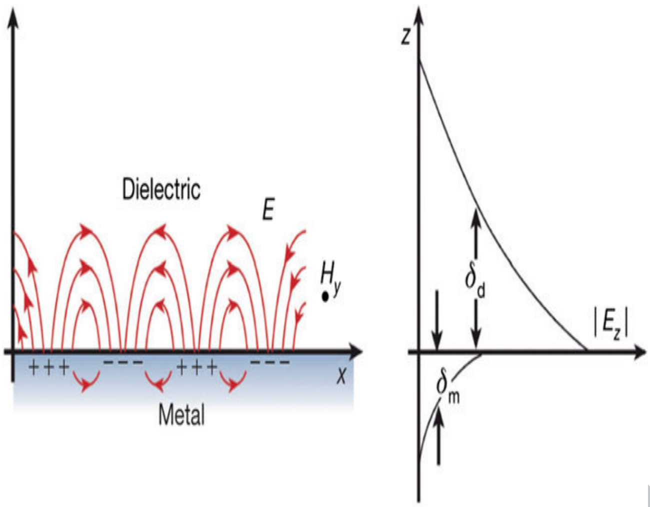

Figure 1: Left: geometry of the system studied. It consisting of metal in contact with dielectric layer. Field components are also shown. Right: electric field amplitude variation of SPP wave [13].

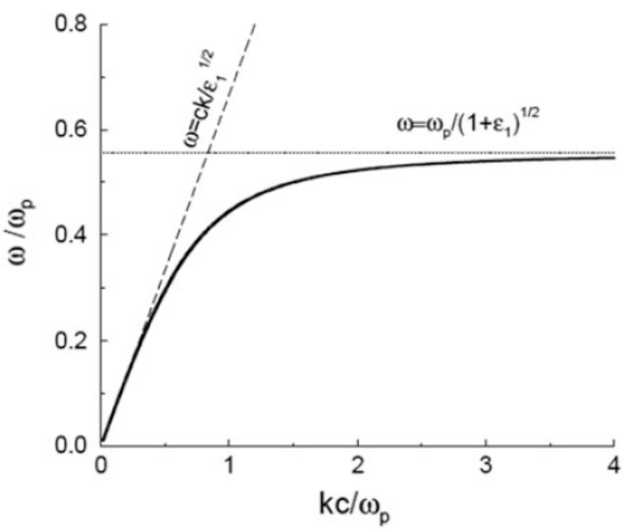

Figure 2 Dispersion line of SPPs and light

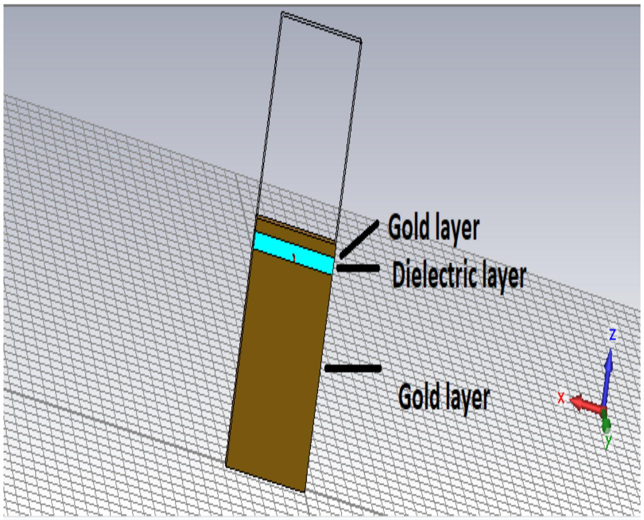

Figure 3 metal-dielectric-metal model.

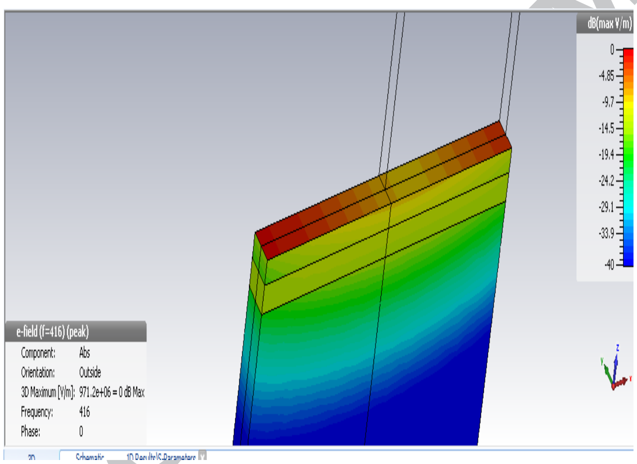

Figure 4: A smooth surface metal/dielectric model.

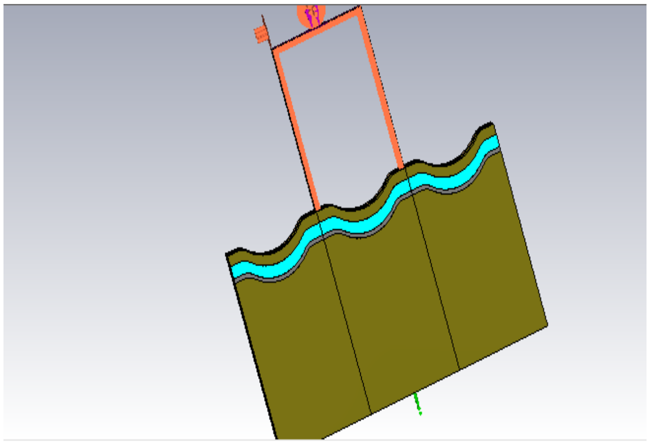

Figure 5: grating assisted surface

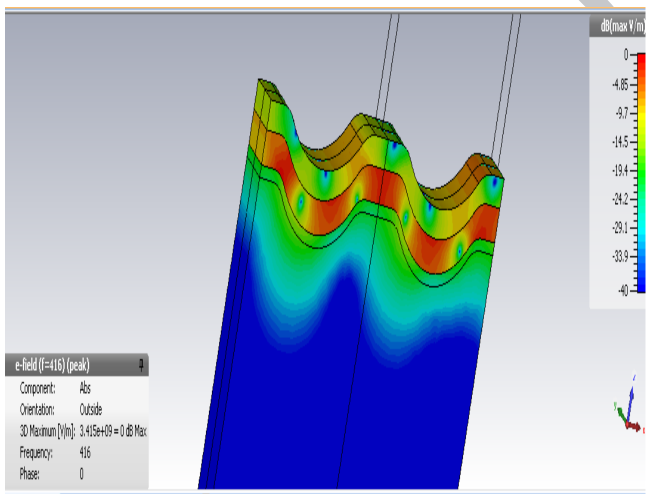

Figure 6: SPPs excitation at the metal-dielectric-metal interface. Mathematics and equations